

Rigid-Body Rotation of Cholesteric Droplets  
Coexisting with Their Isotropic Phase  
Driven by Thermomechanical Coupling

等方相と共存するコレステリック液晶滴の  
熱-力学交差相関による剛体回転

December 2022

Katsu NISHIYAMA

西山 活

Rigid-Body Rotation of Cholesteric Droplets  
Coexisting with Their Isotropic Phase  
Driven by Thermomechanical Coupling

等方相と共存するコレステリック液晶滴の  
熱-力学交差相関による剛体回転

December 2022

Waseda University

Graduate School of Advanced Science and Engineering

Department of Pure and Applied Physics, Research on Soft Matter Physics

Katsu NISHIYAMA

西山 活

# Contents

<b>1</b>	<b>Introduction</b>	<b>1</b>
1.1	Background of this study . . . . .	1
1.2	Purpose of this study . . . . .	4
1.3	Structure of this dissertation . . . . .	5
<b>2</b>	<b>Liquid Crystals</b>	<b>8</b>
2.1	Definition of liquid crystals . . . . .	8
2.1.1	Gases, liquids, and crystals . . . . .	8
2.1.2	Mesomorphic phase . . . . .	10
2.2	Classification of liquid crystals . . . . .	13
2.2.1	Nematic phase . . . . .	13
2.2.2	Cholesteric phase . . . . .	15
2.2.3	Smectic phase . . . . .	19
2.3	Orientational order of nematic phase . . . . .	21
2.3.1	Director . . . . .	21
2.3.2	Order parameter . . . . .	21
2.4	Phase transition . . . . .	24
2.4.1	Phenomenological theory of nematic–isotropic transition . . . . .	24

2.4.2	Nematic–isotropic coexisting phase . . . . .	27
2.5	Elastic theory of nematic phase . . . . .	29
2.5.1	Orientational elasticity . . . . .	29
2.5.2	Coherence length . . . . .	35
2.5.3	Extrapolation length . . . . .	36
<b>3</b>	<b>The Lehmann Effect</b>	<b>39</b>
3.1	Discovery and reproduction of the Lehmann effect . . . . .	39
3.2	Phenomenological description . . . . .	45
3.3	The inverse Lehmann effect . . . . .	50
3.4	Director rotation and rigid-body rotation . . . . .	51
<b>4</b>	<b>Direct Observation of Rigid-Body Rotation Driven by the Lehmann Effect</b>	<b>57</b>
4.1	Purpose . . . . .	57
4.2	Preparation of cholesteric compounds . . . . .	58
4.3	Temperature-control method . . . . .	60
4.4	Polarizing microscopy . . . . .	62
4.5	Results of direct observation of rigid-body rotation by particle tracking method	63
4.6	Rigid-body rotation of an aggregate composed of cholesteric droplets and particles . . . . .	68
4.7	Dependence of angular velocity on droplet radius . . . . .	74
<b>5</b>	<b>Measurement of Coupling Constant <math>\nu</math> between Heat Flux and Torque</b>	<b>78</b>
5.1	Purpose . . . . .	78
5.2	Methods . . . . .	79

5.3	Deriving $\nu$ from balance between Lehmann torque and electric-field-induced torque . . . . .	81
5.4	Results and comparison to previous studies . . . . .	87
<b>6</b>	<b>Theoretical Discussion of Rigid-Body Rotation</b>	<b>92</b>
6.1	Purpose . . . . .	92
6.2	Why rigid-body rotation is driven . . . . .	93
6.3	Shape of Ch droplets observed by confocal reflective microscopy . . . . .	95
6.4	Calculation of torque balance for rigid-body rotation . . . . .	96
<b>7</b>	<b>Friction at Liquid Crystal–Isotropic Coexisting Interface</b>	<b>109</b>
7.1	Purpose . . . . .	109
7.2	Flow measurement in isotropic phase near rotating cholesteric droplets . . . .	110
7.2.1	Methods . . . . .	110
7.2.2	Results . . . . .	110
7.3	Numerical calculation of flow field around droplets . . . . .	113
<b>8</b>	<b>Conclusions</b>	<b>116</b>
	<b>Acknowledgments</b>	<b>120</b>
	<b>References</b>	<b>121</b>

# Chapter 1

## Introduction

### 1.1 Background of this study

Most people associate the term “liquid crystals” (LCs) [1, 2] with LC displays, which are the most widely applied technology using LCs in our daily life [3, 4]. However, as explained in Chapter 2, the term “LC” describes not only LC displays but also a mesomorphic state between the isotropic (Iso) and crystal phases. The fluidity, the anisotropy, and the flexible responsiveness to the external fields of LCs lead to a myriad of intriguing phenomena. For example, this dissertation discusses the “Lehmann effect” [5,6], whereby chiral LC molecules are rotated by a thermomechanical cross coupling when a heat flux is applied.

Rotating devices driven by linear flows exist on various scales, from molecular motors to turbines. Turbines convert the energy of a fluid flow, such as wind, steam, or running water, into rotational motion by means of chirally arranged wings designed to extract mechanical power. Windmills, which are turbines driven by wind, have been used for milling, water pumping, and irrigation and have been in use for many centuries. When turbine-type steam engines, which are driven by high-temperature and -pressure steam, were put into use, they

superseded the older reciprocating steam engine, such as those invented by Watt. Steam turbines made a major impact on industry and are now used in all major types of power generation systems, including thermal and nuclear. In recent years the economy, society, and industrial structures have started to demand clean energy in a quest to achieve “carbon neutrality,” which means zero net emissions of greenhouse gases. One such clean energy source is wind, and power generation using wind turbines is now attracting attention as a clean energy source.

Consider now molecular motors: some rotate under a chemical potential gradient produced by protons or other ions. Examples include the flagellar motors [7–10] of bacteria and some of the ATPase [11–14], which are enzymes that hydrolyze adenosine triphosphate, the energy source for all living organisms. These molecular motors are characterized by a very high rotational efficiency of almost unity [7, 9, 14]. Elucidation of the mechanism driving flagellar motors should not only contribute to the realization of ultra-efficient motors and the development of nanomachines but also help control pathogenicity by the motility in pathogenic bacteria [10]. Some ATPase dysfunctions are reportedly associated with diseases such as osteoporosis, cancer, and deafness, making ATPase an important enzyme from the physiological and medical points of view [15]. These examples show that the mechanism by which flow is converted into rotational motion is important not only academically but also for applications at various scales dating from ancient times to the present.

The Lehmann effect, in which the rotation of a chiral LC is driven by a heat flux, is a type of rotating device similar to turbines where the flow is converted into the rotation of a chiral system. However, turbines differ from the Lehmann effect. The kinetic energy of the fluid produces a torque on the blades, thereby generating the rotational motion of the turbine, whereas it is nontrivial how heat flow generates a torque in chiral LCs. Such phenomena, in which a thermodynamically nonconjugate response occurs in an applied external

field, are called “cross-correlation.” Thermoelectric cross-correlation between temperature gradient and voltage, such as the Seebeck effect and the Peltier effect, and piezoelectric cross-correlation between pressure and voltage are well known examples [16–20]. Peltier devices, which exploit the thermoelectric effect, are widely used for cooling electronics and medical equipment because they are compact, quiet, and easy to maintain since they have no moving parts. Piezoelectric devices are used as actuators and sensors. Thus, devices utilizing cross-correlation see wide use in our daily life.

Thus, converting flow to rotation and cross-correlation is interesting and important both academically and in applications. The Lehmann effect is clearly important because it converts heat flow into rotation of chiral LCs by thermomechanical cross correlation. In recent years energy-frugality has become a vital issue for achieving a carbon-neutral society, so the recuperation of unused thermal energy from homes, factories, nuclear power plants, automobiles, etc. has attracted attention as one way to contribute to this goal. The Lehmann effect can be driven by small temperature gradients of several  $\text{mK } \mu\text{m}^{-1}$ , and is thus expected to be applied to micromotors for exploiting unused thermal energy.

This study also focuses on the coexisting LC–isotropic phase. The coexisting phase itself is easily found in nature. For example, if ice is placed in a glass and left at room temperature, it becomes ice water with ice floating in the water at  $0\text{ }^\circ\text{C}$ . This is the coexistence of the crystalline phase and the liquid phase (isotropic phase). When a room is heated on a cold winter day, water droplets sometimes condense on the window glass, which is cooled by the outside air. This is the coexistence of Iso phases of water (liquid) and water vapor (gas). Since the transition between the LC phase and the Iso phase is also a weak first-order phase transition, coexistence states such as ice–water or water–water vapor are possible. In this study, spherical chiral LC droplets were formed in their Iso phase by keeping them at the phase transition temperature, and the rotation of the droplets was detected upon applying



a temperature gradient. The LC–Iso coexisting phases are characterized by their physical properties and interfaces. The physical properties of the LC phases, such as orientation order, dielectric anisotropy, and orientational elasticity (all of which will be described in detail in Chapter 2) depend on temperature and discontinuously go to zero at the transition temperature of the Iso phase [21]. It is difficult to accurately measure the physical properties of the LC phase in the coexisting phases at the phase transition temperature, which is an unresolved problem. In terms of the interface, the LC–Iso coexisting interface differs from the solid–liquid and liquid–gas interfaces because the LC and Iso phases are both fluid and have almost the same density whereas they have different orientational order and symmetry. The coexisting interface and the liquid–liquid interface, which is formed with isotropic liquids, are clearly distinguished because the LC–Iso phase transition is first order. Although some studies study the static properties [22, 23], the dynamic properties of the coexisting interface have yet to be studied. The present study thus contributes to our knowledge of the coexisting interface.

## **1.2 Purpose of this study**

The previous section describes how the Lehmann effect can be applied in society. Although the Lehmann effect generates torque in chiral LC molecules, causing them to rotate, the specific rotational motion of the molecules remains subject to debate (see details in Chapter 3). The controversy over the rotation recalls the controversy over the geocentric versus heliocentric models. Under the geocentric model, the sun, Moon, stars, and planets orbit Earth, which is at the center of the Universe. In contrast, in the heliocentric model, Earth and the planets orbit the sun, which is at the center of the Universe. These models could not be differentiated by simply observing the sky, which led to the dispute.

The controversy over the rotational motion in the Lehmann effect is somewhat similar to

this. However, the question is not whether the LC molecules rotate but whether they rotate about their own axis or about the rotational axis. The rotational motion in which the molecules rotate only in their orientation without moving their center of mass is called “director rotation.” The revolution motion in which the molecules revolve about the central axis of rotation while maintaining their relative orientation is called “rigid-body rotation.” Polarizing microscopy, the most commonly used method for observing LCs, shows changes in the texture of liquid crystals due to the Lehmann rotation. Just as we could not distinguish between heliocentric and geocentric motion by looking at the sky, we cannot distinguish between director rotation and rigid-body rotation by looking at polarizing microscopy images.

The purpose of this study is to clarify whether the textural rotation of chiral LC droplets driven by the Lehmann effect is director rotation or rigid-body rotation. Although this is a fundamental question, no clear evidence has appeared for over a hundred years since Lehmann discovered this phenomenon in 1900. The question of whether textural rotation corresponds to director rotation or to rigid-body rotation is intriguing from the physical point of view because it is a fundamental question of how the microscopic torque exerted on the molecules drives the macroscopic rotation of the LC droplets. In addition, distinguishing between director rotation and rigid-body rotation and controlling these rotations will constitute a significant contribution to their application as soft micromotors.

### **1.3 Structure of this dissertation**

This doctoral dissertation consists of eight chapters. Chapter 2 summarizes the current knowledge of LCs, which is necessary to understand this dissertation. Those already familiar with LCs may skip this chapter.

Chapter 3 explicates the experimental history and the phenomenological description of the

Lehmann effect, which is the main topic of this dissertation. In addition, the most important concepts in this dissertation (i.e., director rotation and rigid-body rotation) are explicated with the help of previous studies.

My own studies are described in Chapters 4–7. Chapter 4 reports the results of measurements of the flow associated with the Lehmann rotation of the LC droplets, which were done by using the particle-tracking method. These experiments detected the flow associated with droplet rotation, with the results being independent of the orientational interior structure of the droplets. Furthermore, I formed dumbbell-shaped aggregates from two droplets and a particle aggregate and forced the rotation of the composite while retaining its interior structure. These results show that flow rotates the droplets and the composites, which shows that rigid-body rotation can be driven by the Lehmann effect.

Chapter 5 discusses the coupling constant between heat flux and the torque generated, which provides a measure of the efficiency of the Lehmann effect. A temperature gradient and an electric field were applied simultaneously to Ch droplets, and the coupling constant was obtained from the static balance between the Lehmann-induced torque and the electric-field-induced torque. The advantage of such static measurements is that the contribution of dynamic viscous friction at the interfaces is eliminated. Although this measurement method has been used in previous studies, I use it here to estimate the coupling constant by accurately accounting for the spatial dependence of the electric field.

Chapter 6 discusses the mechanism by which the microscopic Lehmann torque acting on the LC molecules drives the macroscopic rigid-body rotation of LC droplets in terms of the anchoring at the interface and orientational elasticity. Furthermore, I calculate the Lehmann torque on the droplets and the viscous torque required to balance the Lehmann torque; I furthermore provide a consistent explanation of the rigid-body rotation of an individual droplet and of a composite.

Chapter 7 reports the use of the particle tracking method to measure the flow field in the Iso phase in the vicinity of a rotating droplet. No flow was detected in the vicinity of the rotating droplets, suggesting that friction is extraordinarily low at the interface between the coexisting Ch and Iso phases.

Finally, Chapter 8 summarizes this study.

# Chapter 2

## Liquid Crystals

### 2.1 Definition of liquid crystals

#### 2.1.1 Gases, liquids, and crystals

States or phases of matter are generally gases, liquids, or solids. For example, water is a liquid at room temperature under atmospheric pressure. When heated, it boils at 100 °C to become a gas and, when cooled, it solidifies at 0 °C to become a solid (here, metastable states such as superheating and supercooling are not considered). Not only for water but also in general, if the bonds between atoms and molecules remain as the temperature changes, matter becomes a gas at high temperature and a liquid and then a solid as the temperature decreases.

Let us consider how gases, liquids, and solids are distinguished. Gases and liquids are usually distinguished their difference in density. However, since the density is a continuous quantity, it does not clearly define the boundary between gases and liquids. When a phase transition occurs between a gas and a liquid, the density changes discontinuously, so the density clearly distinguishes the phases. Conversely, at temperatures and pressures above the

critical point, the density changes continuously, obfuscating the distinction. One may think that liquids and solids are distinguished by their hardness. However, the glassy state is a metastable state in which a liquid is supercooled without becoming a solid and has liquid-like properties [24]. For this reason, the phase cannot be determined based solely on hardness.

Concerning the distinction of the states of matter, it is proper that liquids (gases) and solids are distinguished by symmetry. Gases and liquids are the same in terms of symmetry. In gases and liquids, the position of the center of mass of the constituent molecules is spatially random and varies in time so that the time-averaged density is uniform and constant both temporally and spatially. The constituent molecules are not necessarily spherical, but the orientation of each molecule is also disordered as the molecules rotate randomly around the center of mass. Because all directions are equivalent and isotropic, gases and liquids are collectively called Iso phases. Iso phases have the highest symmetry, being symmetric about any translation, rotation, inversion, mirroring, or any combination thereof.

In the solid state, which is also called the crystal phase, the position of the center of mass of the constituent atoms and molecules is ordered, making the symmetry lower than that of the Iso phase. The positions of the constituent atoms and molecules are given by the primitive translation vectors  $\mathbf{a}_1$ ,  $\mathbf{a}_2$ , and  $\mathbf{a}_3$ . The crystal phase is symmetric with respect to translation by  $n_1\mathbf{a}_1 + n_2\mathbf{a}_2 + n_3\mathbf{a}_3$  with integer  $n_1$ ,  $n_2$ , and  $n_3$ . The symmetric rotational axis and angle are limited due to the lattice structure of the crystal.

Here, I digress briefly to present the notation of symmetry. The Iso phase symmetry is denoted by  $K_h$  (or  $K$  when the constituent molecules are chiral) in the Schoenflies notation [25, 26]. This is a symbol for point groups and cannot describe translational operations. When the periodic structure is related to symmetry, as in crystals, the Hermann–Mauguin notation (sometimes called the “international notation”) is used to describe space group in which the translational operations are added to a point group. When describing the symmetry

of LC phases, the Schoenflies notation can be used because there is no positional order.<sup>1</sup> The symbols that appear frequently in the study of LCs are  $C$  and  $D$ , which mean cyclic and dihedral, respectively.  $C_n$  symmetry has only an  $n$ -fold rotation axis. When there is a mirror plane perpendicular to the  $n$ -fold rotation axis in addition to  $C_n$ , it is denoted by  $C_{nh}$  with h, which means “horizontal,” as a subscript. When  $n$  mirror planes contain the rotation axis, a subscript v, which means “vertical,” adorns the symbol (e.g.,  $C_{nv}$ ).  $D_n$  symmetry has not only an  $n$ -fold rotation axis but also  $n$  twofold rotation axes perpendicular to the  $n$ -fold rotation axis. Similarly to  $C$  symmetry,  $D_{nh}$  is  $D_n$  with a mirror plane perpendicular to the  $n$ -fold rotation axis. When  $D_n$  also has  $n$  mirror planes containing the  $n$ -fold rotation axis, a subscript d, which means “diagonal,” is added (e.g.,  $D_{nd}$ ). In  $D_{nd}$  symmetry, a mirror plane bisects the angle between adjacent twofold rotation axes.

### 2.1.2 Mesomorphic phase

Considering symmetry, the distinction between phase states should be clarified. Iso phases, including gases and liquids, are isotropic in terms of the directions, with the constituent atoms and molecules having no positional order. In contrast, the position of the constituent atoms and molecules in crystal phases exhibits long-range order in the form of a periodic and anisotropic structure.

In general, the long-range order in position and direction changes simultaneously when a phase transition occurs due to a change in temperature—as in water, for example. However, the positional and orientational orders are thermodynamically allowed to change at different temperatures. In other words, it is not surprising that a “mesomorphic phase” (or a mesophase) exists between the crystal and Iso phases that has either only positional order or only orienta-

---

<sup>1</sup>Although the Hermann–Mauguin notation should be used for smectic phases because they have one-dimensional periodic structures, the Schoenflies notation works well in most cases. The Hermann–Mauguin notation is used for the columnar and cubic phases, which have periodic structures of two or more dimensions.

tional order (with positional order having less than three dimensions). In materials in which the transition temperature of orientational order is lower than that of positional order, the molecules rotate freely and orient themselves randomly in time and space while maintaining a three-dimensional long-range order with respect to position. Although such a state looks like a solid, its elastic constant is so small that it cannot retain its shape for long. In addition, it has plasticity [27], so this state is called a “plastic crystal.” The fullerene C<sub>60</sub> is a well-known material that forms a plastic crystal. Although plastic crystals are one of the mesomorphic phases, I do not use them in this study, so I do not discuss them in detail here. In contrast, materials whose transition temperature for orientational order exceeds that of position order form a state in which long-range three-dimensional order of the position of the constituent molecules is lost, but orientational order is retained. In this state, the lack of positional order allows the material to flow like a liquid, while the orientation order allows it to exhibit anisotropic electromagnetic and mechanical properties, like a solid [28,29]. This state, which can be considered a “liquid with orientation,” is called a “liquid crystal” (LC) because it has the characteristics of both liquids and crystals.<sup>2</sup> The LC phase does not appear in all materials because most materials transition directly between crystal and Iso phases. The LC phase is often observed when the molecules have anisotropic shapes such as rods or disks. The LCs that appear in this study are only formed by rod-shaped molecules with low molecular weight.

The above argument considers a single-component system in which a mesomorphic phase appears as the temperature changes. This type of LC phase is called a “thermotropic” phase, and its phase transition also depends on pressure. When some types of molecules are added to a solvent, the mixture exhibits the LC phase transition by change in the concentration. LC

---

<sup>2</sup>The term “liquid crystal” is the name of a mesomorphic phase explained here. Materials that form LC phases are sometimes called LCs even if they are not in the LC phase. In this dissertation, material compounds that can form LC phases are sometimes referred to as “LC samples” for convenience, regardless of their phase state. In everyday life, “LC” often refers to LC displays, although these are not discussed in this dissertation.



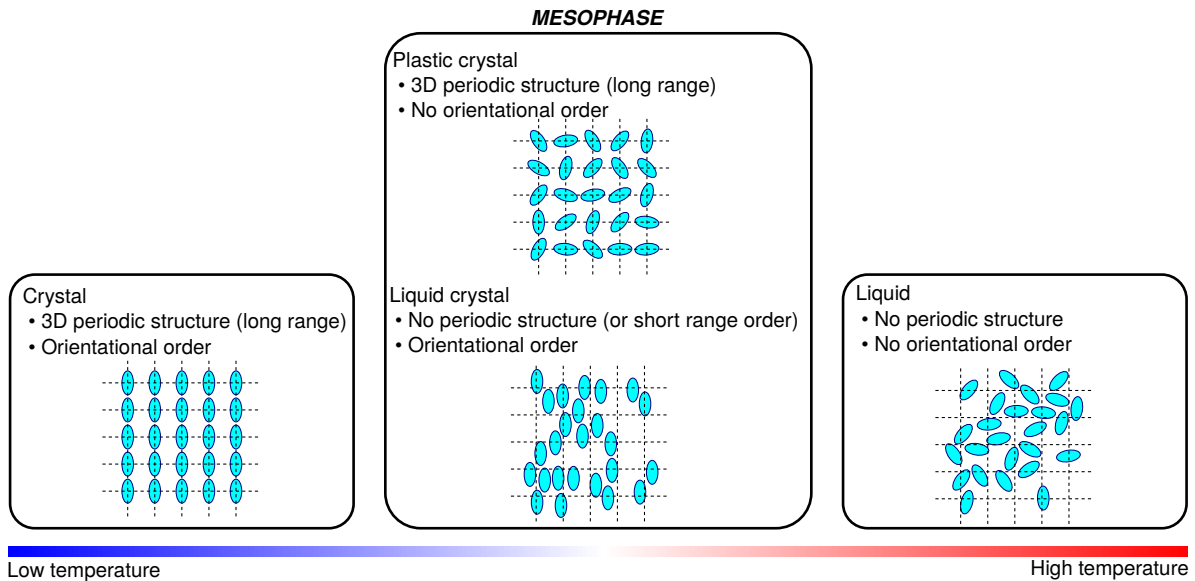


Figure 2.1: Schematic figure of crystal, isotropic, and mesomorphic phases.

phases that form not due to changes in temperature but instead due to changes in concentration are called “lyotropic” phases [29–32]. Lyotropic LC phases come in two types: One type consists of molecules with two incompatible parts with different chemical properties, forming an LC phase driven by microscopic phase separation [33, 34]. Examples include a system in which a surfactant with hydrophobic and hydrophilic groups at opposing ends of the molecule is dissolved in water. The other type of lyotropic LC phase forms from rigid highly concentrated rod-like polymers [35, 36], which is driven by the excluded-volume effect [37]. For example, an aqueous solution of hydroxypropyl cellulose, which is used as an additive in foods and pharmaceuticals, transitions to the LC phase at high concentrations [38, 39]. Only thermotropic LCs are used in this dissertation.

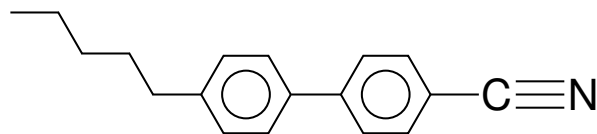


Figure 2.2: Chemical structure of 4-Cyano-4'-pentylbiphenyl.

## 2.2 Classification of liquid crystals

LC phases are finely classified into various phases based on symmetry. Of the LC phases induced by rod-shaped small molecules, this section first describe the nematic phase and then the cholesteric phase, which are closely related to this study. The smectic phase is not treated in this study but is introduced briefly because it is a well-known phase.

### 2.2.1 Nematic phase

The LC phase formed by rod-like small molecules does not transition to a one-dimensional liquid but, based on the symmetry of the shape of the constituent particles, it transitions to a three- or two-dimensional liquid. The three-dimensional liquid LC phase is called the nematic (N) phase,<sup>3</sup> which looks like a white fluid. Figure 2.2 shows an example of a molecule that forms a N phase: a 4-Cyano-4'-pentylbiphenyl, commonly known as 5CB, which has an alkyl chain and a cyano group at each end of its biphenyl group. LC molecules with this type of structure are called cyanobiphenyl LCs. Cyanobiphenyl LCs are chemically and photochemically stable, and their physical properties are well balanced, which is important for the practical use [42, 43].

The constituent molecules of the N phase have no long-range positional order but do have long-range orientational order. The molecules themselves, being polarized, form asymmetric rod-like structures in the long-axis direction. In the short-axis direction, the polarizability

---

<sup>3</sup>The name “nematic” is derived from a Greek word “νημα,” which means thread [40, 41]. This is because the unique defect line, the disclination, looks like a thread.

differs between the directions perpendicular and parallel to the two benzene rings. Therefore, if these molecules are aligned in the same direction, they have different dielectric constants in each of the three directions. This type of material is called a “optically biaxial.” In fact, the N phase of 4-Cyano-4'-pentylbiphenyl is macroscopically nonpolar and has different dielectric constants for the long- and short-axes; the dielectric constants do not differ in each of the three directions. Materials such as this N phase, in which the dielectric constants differ only in a certain direction and are the same in the plane perpendicular to the given direction, are called “optically uniaxial” materials. Apolar and optically uniaxial N phase has a cylindrical symmetry, which is denoted by  $D_{\infty h}$  in the Schoenflies notation. Most N-phase material commonly has  $D_{\infty h}$  symmetry. The fact that the N phase is composed of polar molecules yet is macroscopically apolar indicates that long-range order dominates in the direction of the long axis, whereas no such order exists in the direction of the cyano group and of the alkyl chain. In other words, there are the same numbers of the molecules with the opposite direction of the cyano group, and they cancel each other's polarity, making the N phase apolar overall. Since the N phase is optically uniaxial, the direction of the planes formed by the benzene rings do not have long-range order; they are oriented randomly around the long axis.

The usual N phase is apolar and uniaxial with  $D_{\infty h}$  symmetry, and this type of N LCs are used in this study. Other types of N phases exist, such as polar N phases, in which the direction of the permanent dipole moment of the molecule has macroscopic order, and biaxial N phases with long-range order not only in the direction of the molecular long axis but also in the direction perpendicular to the long axis. Since the N phase has the highest symmetry of all LC phases and is the most liquid-like LC phase, it usually appears at the highest temperature of the LC phases. However, some materials have N phases not only at the highest temperature in the LC-temperature range, but also at temperatures below the temperature range in which LC phases with lower symmetry (such as smectic phases) appear. The N phase that appears at

lower temperature is called the “reentrant” N phase. When monomers and dimers of certain types of LC molecules coexist with each other in the Iso phase, the numbers of the dimers become larger than that of the monomers at lower temperature. The increased number of dimers augments the repulsive interaction due to the excluded-volume effect, which increases the LC symmetry.

### 2.2.2 Cholesteric phase

The N phase has mirror symmetry. When the constituent molecules of the N phase do not have mirror symmetry because they contain chiral carbons, or if a chiral molecule is added to the N phase, a chiral LC phase appears. Breaking microscopic mirror symmetry critically affects the macroscopic static structure and dynamic properties.

Let us consider changes in the static structure due to broken mirror symmetry. Given a molecule and the  $D_\infty$  axis through the molecule, when the molecule has a  $D_{\infty h}$  symmetry in which the mirror symmetry plane is perpendicular to the  $D_\infty$  axis, then the long axis of the molecule must be perpendicular to this mirror plane. In contrast, when the molecules are chiral, which eliminates the mirror symmetry plane of the  $D_\infty$  axis, the long axis of the molecules around the  $D_\infty$  axis can be deformed to tilt from the direction parallel to the axis. The deformation shown in Figure 2.3, in which the molecules tilt around the line perpendicular to the  $D_\infty$  axis by an angle proportional to the distance from the  $D_\infty$  axis, has  $D_\infty$  symmetry.

Although a certain molecule and the  $D_\infty$  axis passing through that molecule have been considered above, there is no reason why only one of the molecules that constitute the LC should be special, and this argument holds for all molecules. Therefore, this argument can be applied to a second molecule at a certain distance from the first molecule, and the  $D_\infty$  axis passing through the second molecule. However, when this argument is applied as is, as shown in Figure 2.4a, an orientational inconsistency arises around the first and the second molecules,

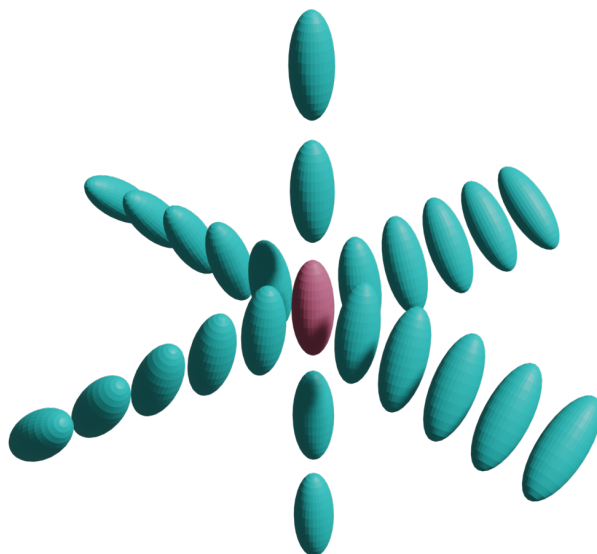


Figure 2.3: A deformation that can occur in chiral liquid crystals. The ellipsoids denote liquid crystal molecules. The  $D_\infty$  axis runs along the long axis of the red ellipsoid in the center.

excepting the distance in which the molecules tilt by  $90^\circ$ . Two types of orientational structures appear in such a chiral system: One is a structure in which the constituent molecules do not twist isotropically around the  $D_\infty$  axis to avoid the inconsistency, as shown in Figure 2.4b. This type of LC phase with a structure that twists only in uniaxial direction and not at all in the direction orthogonal to the twist is called the “cholesteric” (Ch) phase.<sup>4</sup> The Ch phase can occupy the whole three-dimensional space without defects. The other structure, the blue phase, is composed of double-twist cylinders with  $45^\circ$  tilt of molecules (Figure 2.5). The molecular orientation is continuous where the cylinders make contact. However, the double-twist cylinder cannot occupy the space without the defects. The inconsistency of the molecular orientation due to the twisting structure remains as a defect, which has higher energy than the continuous orientation. Since defects generation requires energy, this structure appears when

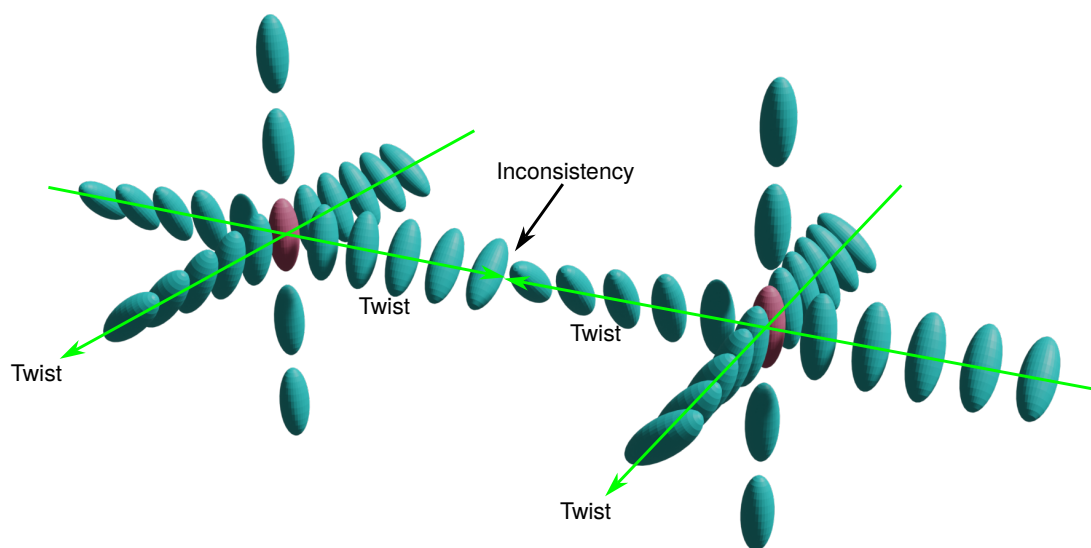
---

<sup>4</sup>This name was given because it was discovered in cholesterol derivatives.

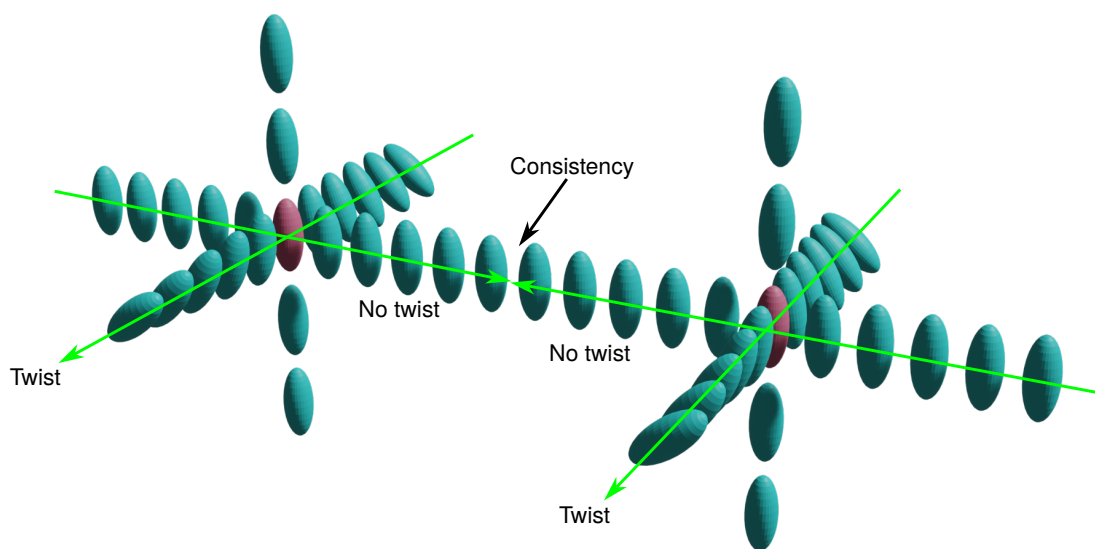
a strong interaction causes the molecules to twist in such a way that the energy gain from twisting exceeds the loss from making the defects. The LC phase with this structure is called the blue phase [44]. The blue phase is not discussed in detail because only the Ch phase is used in this study.

The Ch phase has a simple twist structure in which the molecular orientation consists of twisting in the uniaxial direction. Although the interaction terms that twist the molecules lead to loss, this structure fills the three-dimensional space without making defects. Although the mirror symmetry is lost, the thermodynamic properties of the Ch phase are the same as those of the N phase; the Ch phase is a three-dimensional liquid with no long-range positional order in the constituent molecules. For this reason, the Ch phase is also called the chiral nematic phase.

Observing through crossed polarizers a Ch compound sandwiched between two glass substrates under a polarizing microscope [45, 46] reveals textures, as shown in Figure 2.6. Figure 2.6a shows the texture that appears when the substrate surfaces are processed so that the molecules are perpendicular to the substrates surface (and to the paper surface). This is called the “fingerprint” texture because of its characteristic striped fingerprint-like pattern. When this texture appears, the helical axis of the molecular orientation is parallel to the glass substrate (and to the paper surface) and the orientation is rotated by  $\pi$  from a stripe to the next stripe. In contrast, Figure 2.6b shows the texture when the glass substrate interfaces and the molecules are parallel (to the paper surface). This texture is called the the “Grandjean” texture. The helical axis is perpendicular to the glass substrate (and to the paper surface), and defects called “oily streaks” are caused by the pseudo-layer structure made of the periodic helical structure [47].



(a)



(b)

Figure 2.4: (a) The double-twist structure about the long axis of red ellipsoids leads to the inconsistency. (b) In the single-twist structure, the molecules twist in uniaxial direction instead of the double-twist.

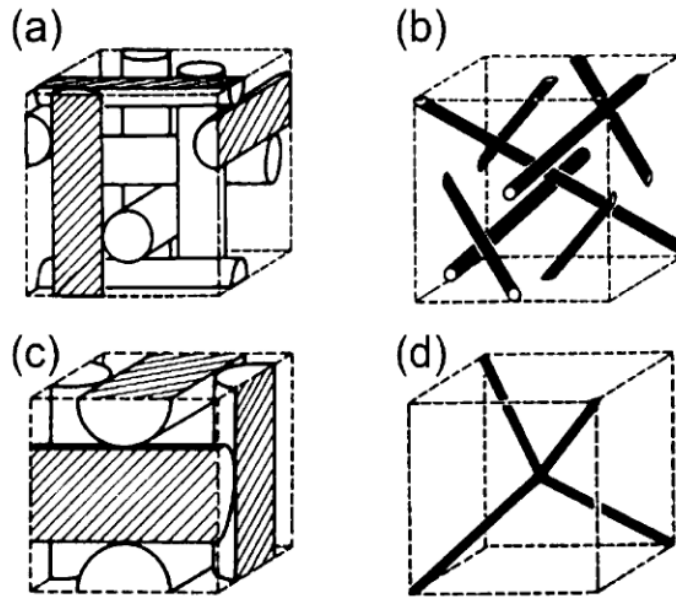
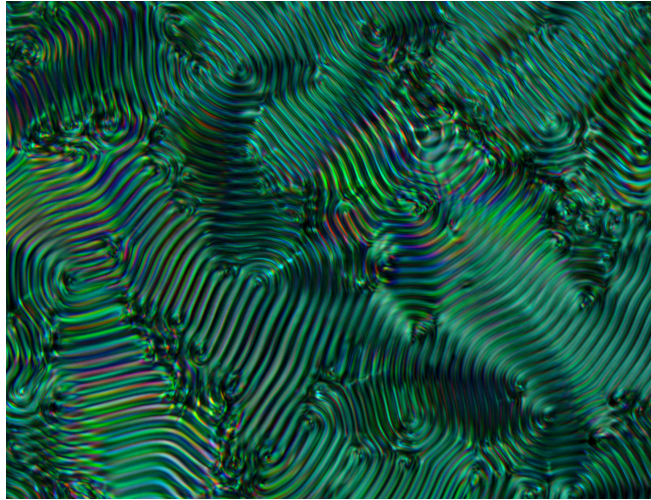


Figure 2.5: Structure of blue phase (a), (b) I and (c), (d) II. The cylinders in panels (a) and (c) indicate double-twist cylinders, and the lines in panels (b) and (d) indicate disclination lines. This figure is reproduced from Reference [44].

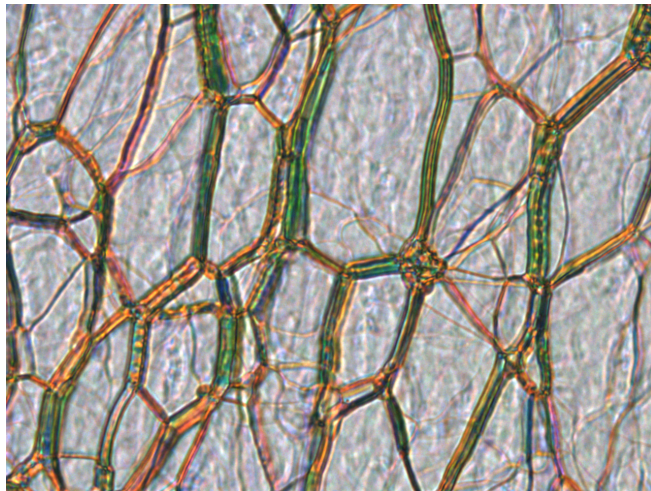
### 2.2.3 Smectic phase

Both the N and Ch phases are three-dimensional liquids with only long-range order with respect to orientation and no long-range order with respect to position. In contrast, the smectic phase has a one-dimensional positional order. In other words, the smectic phase has a layer structure. The smectic phase is systematically classified in terms of the order in the layer and the inclination of the molecules relative to the layer normal and are given alphabetical names such as smectic A, smectic B, and so on [48]. However, since the names were given in the order in which they were discovered, the nomenclature is neither systematic nor related to physical properties.





(a)



(b)

Figure 2.6: Polarizing microscopy images of (a) fingerprint texture and (b) Grandjean texture, as viewed through crossed polarizers.

## 2.3 Orientational order of nematic phase

### 2.3.1 Director

Let us consider materials composed of small rod-like molecules. In the Iso phase, since there is equal probability for the long axis of the molecules to be in any direction, the molecules are oriented in random directions and possess continuous rotational symmetry. When the phase transitions from Iso to N, the continuous rotational symmetry of the Iso phase is lost. The long axes of the molecules become oriented in one direction due to the intermolecular interaction. The direction of molecular orientation is denoted by a unit vector  $\mathbf{n}$ , which is called the “director.” The director is defined by the average direction of the molecules in a physically infinitesimal volume that is macroscopically small enough but sufficiently larger than the molecules and the intermolecular distance, as per the definition of the dielectric polarization and the magnetization. As shown in Figure 2.7, the average direction of the molecules in a physically infinitesimal volume  $\delta V(\mathbf{r})$  with the center of  $\mathbf{r}$  is denoted by  $\mathbf{n}(\mathbf{r})$ . Since a typical N phase possesses  $D_{\infty h}$  symmetry,  $\mathbf{n}(\mathbf{r})$  and  $-\mathbf{n}(\mathbf{r})$  denote the physically same state;  $\mathbf{n}(\mathbf{r}) = -\mathbf{n}(\mathbf{r})$ .

### 2.3.2 Order parameter

While the director  $\mathbf{n}(\mathbf{r})$  is defined as the average orientational direction of the LC molecules, not all the long axes of the molecules are aligned in the direction of  $\mathbf{n}(\mathbf{r})$ . The orientational state of the actual N phase is far from completely uniform, with all the molecules oriented in the direction of  $\mathbf{n}(\mathbf{r})$ . The degree of orientation of the constituent molecules of LCs relative to the director  $\mathbf{n}(\mathbf{r})$  affects the macroscopic anisotropy of the mechanical and electromagnetic properties, being an important parameter.

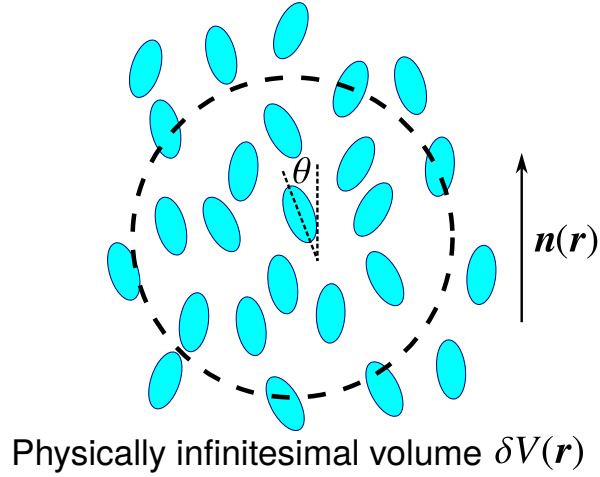


Figure 2.7: Definition of the director  $\mathbf{n}(\mathbf{r})$ . The ellipsoids and  $\theta$  denote the molecules and the angle of molecules from the director.

The degree of orientation of the molecules is described by a orientational distribution function  $f(\theta, \varphi)$ , where  $\theta$  and  $\varphi$  denote the zenithal and azimuthal angles, respectively, and the  $z$  axis is in the direction of  $\mathbf{n}(\mathbf{r})$ . Considering  $D_{\infty h}$  symmetry, which a typical N phase possesses, the distribution function  $f$  is independent of  $\varphi$ ;  $f = f(\theta)$ . The distribution function  $f$  is qualitatively characterized by physical states that are the same for both  $\theta = 0$  and  $\theta = \pi$ , with  $f$  symmetric about  $\theta = \pi/2$ , and, since  $\mathbf{n}(\mathbf{r})$  denotes the average orientational direction,  $f$  has local maximum and local minimum values at  $\theta = \pi$  and  $\theta = \pi/2$ , respectively.

The specific form of the distribution function can be determined from the Boltzmann distribution if the potential for  $\theta$  were known. In general, however, this potential is difficult to obtain, both theoretically and experimentally. Thus, LC properties such as the degree of orientation and the macroscopic anisotropy are analyzed by expanding the distribution function in orthogonal functions and using lower-order terms as necessary. Orthogonal functions should be chosen by considering the relationship between the degree of orientation and the macroscopic anisotropy. In this case, expanding in the basis of Legendre polynomials

$P_l(x)$  works well [49]:

$$P_l(x) = \frac{(-1)^l}{2^n n!} \frac{d^l}{dx^l} (1-x^2)^l, \quad (2.1)$$

where  $l$  is an integer. Expanding  $f(\theta)$  in terms of  $P_l(\cos \theta)$  gives

$$f(\theta) = \sum_{l=0}^{\infty} \frac{1}{2} (2l+1) S_l P_l(\cos \theta). \quad (2.2)$$

Considering the orthogonality of the Legendre polynomials, the expansion coefficients  $S_l$  are

$$S_l = \int_{-1}^1 P_l(\cos \theta) f(\theta) d(\cos \theta) = \langle P_l(\cos \theta) \rangle, \quad (2.3)$$

where  $\langle \cdot \rangle$  denotes the average at equilibrium. These expansion coefficients indicate the degree of orientation relative to the director, called the order parameter of order  $l$ . The specific forms of lower-order order parameters are

$$\begin{aligned} S_0 &= \langle P_0(\cos \theta) \rangle = 0, \\ S_1 &= \langle P_1(\cos \theta) \rangle = \langle \cos \theta \rangle, \\ S_2 &= \langle P_2(\cos \theta) \rangle = \frac{1}{2} \langle 3 \cos^2 \theta - 1 \rangle, \\ S_3 &= \langle P_3(\cos \theta) \rangle = \frac{1}{2} \langle 5 \cos^3 \theta - 3 \cos \theta \rangle, \\ S_4 &= \langle P_4(\cos \theta) \rangle = \frac{1}{8} \langle 35 \cos^4 \theta - 30 \cos^2 \theta + 3 \rangle. \end{aligned} \quad (2.4)$$

Excepting the zeroth order, the order parameters go to unity for uniform orientation, for which  $\langle \cos^2 \theta \rangle = 1$ , and zero for random orientation, for which  $\langle \cos^2 \theta \rangle = 1/3$ . In terms of a usual N phase in which  $\mathbf{n}(\mathbf{r}) = -\mathbf{n}(\mathbf{r})$  holds, all order parameters of odd order are zero. Therefore, the lowest order parameter of importance is  $S_2$ , which is the most often used. The important physical properties of the N phase, such as refractive indices, dielectric constants,

and magnetic susceptibilities, are proportional to  $\langle \cos^2 \theta \rangle$  and then to  $S_2$  directly [28, 29]. The specific value of  $S_2$  obtained experimentally for the N phase is in the range 0.2–0.4 near the N–Iso transition temperature and increases to 0.6–0.7 at temperatures significantly below the transition temperature [50, 51].

Some situations exist in which  $S_2$  is negative; for example,  $S_2$  is negative when the molecules oriented perpendicular to  $\mathbf{n}(\mathbf{r})$  are dominant. If all the molecules are oriented in the plane perpendicular to  $\mathbf{n}(\mathbf{r})$ ,  $\langle \cos^2 \theta \rangle = 0$  leads to  $S_2 = -1/2$ . The absolute value of  $S_2$  is 1/2 because there are two degrees of freedom for the orientational direction in the plane perpendicular to  $\mathbf{n}(\mathbf{r})$ .

Hereinafter, the notation  $S$  denotes the order parameter of second order ( $S_2$ ).

## 2.4 Phase transition

### 2.4.1 Phenomenological theory of nematic–isotropic transition

Since the LC phase is composed of molecules, a theory that considers intermolecular interaction is required to rigorously treat phase transitions; such a theory is called a “molecular theory” and can be traced back to two major origins: One is Onsager’s theory of repulsive interactions [37], and the other is Maier and Saupe’s theory of attractive interactions [52]. This dissertation does not mention molecular theory, although molecular theory can clarify the roles of intermolecular attractive and repulsive interactions in the phase transitions of LCs and in the physical properties of each phase.

In contrast, transitions in states of matter can be described from a macroscopic standpoint, without considering microscopic interactions between molecules. A parameter that quantitatively characterizes the transitions is introduced and the free energy of the system is

described as a function of that parameter. This method was established by Landau and is called “phenomenological theory” [26]. The parameter that tunes the symmetry and structure of the system due to the phase transition is defined to be zero in the high-symmetry phase and finite in the low-symmetry phase. The order parameter  $S \equiv S_2$  defined by Equation 2.4 can be a phenomenological parameter that describes the phase transition of LCs.  $S$  varies discontinuously at the phase-transition point in the first-order phase transition, as does the volume and entropy of the system. For the second-order phase transition, the order parameter  $S$ , the volume, and the entropy all vary continuously at the phase-transition point. LCs exhibit phase transitions, such as LC–Iso, crystal–LC, and LC–LC transitions, with various modifications of their symmetry. Concerning the N–Iso transition, the discontinuity of the parameters at the transition point is small, being a first-order transition close to the second order. Near the transition temperature,  $S$  becomes so small that the free energy of the system can be expanded in the power series of  $S$ . The phenomenological theory describing phase transitions is based on the assumption that the free energy can be expanded in powers of a phenomenological parameter.

In the vicinity of the N–Iso transition point, the free energy of the system  $F$  can be expanded in powers of the order parameter  $S$ :

$$F = F_0 + AS + \frac{1}{2}BS^2 + \frac{1}{3}CS^3 + \frac{1}{4}DS^4 + \dots, \quad (2.5)$$

where  $F_0$  is the free energy at the ground state, and  $A$ ,  $B$ ,  $C$ , and  $D$  are the expansion coefficients. Since the energy minimum is at  $S = 0$  in Iso phase,  $\partial F/\partial S|_{S=0} = 0$  and the first-order term vanishes:  $A = 0$ . The second-order term is necessary for the energy to have a local minimum at  $S = 0$ . The third-order term does not vanish because  $S$  and  $-S$  denote different physical states. In terms of the N phase, since the energy is minimal for  $S > 0$ ,

the coefficient  $C$  is negative. If the third-order term ends the expansion, the energy goes to negative infinity due to  $S \rightarrow \pm\infty$ ; the fourth-order term must have a positive coefficient,  $D > 0$ . Terms greater than fifth order can be neglected because  $S \ll 1$  near the transition point. Here, it is assumed that only the coefficient  $B$  depends linearly on temperature:

$$B(T) = a(T - T^*), \quad a > 0, \quad (2.6)$$

where  $T^*$  is the temperature at which the Iso phase becomes absolutely unstable.<sup>5</sup> The other coefficients  $C$  and  $D$  are assumed to be independent of temperature.

I now discuss the solutions of  $\partial F/\partial S = 0$ , which give stable or metastable states.

1. When  $T > T^* + C^2/4aD$ ,  $F$  has the minimum value at  $S = 0$ .
2. When  $T = T^* + C^2/4aD$ ,  $F$  has a local minimum at  $S = 0$  and a stationary value at  $S = -C/2D$ .
3. When  $T^* + C^2/4aD > T > T^*$ ,  $F$  has a local minimum at  $S = 0$ , a local maximum at  $S = (C + \sqrt{C^2 - 4BD})/2D$ , and another minimum value at  $S = (C - \sqrt{C^2 - 4BD})/2D$ .  
In particular, the two local minima become the same when  $T = T_c = T^* + 2C^2/9aD$ .
4. When  $T = T^*$ ,  $F$  has a stationary value at  $S = 0$  and a local minimum at  $S = (C + \sqrt{C^2 - 4BD})/2D$ .

As shown in Figure 2.8, The Iso phase with  $S = 0$  is most stable when  $T > T_c$ . When  $T = T_c$ , both the Iso phase with  $S = 0$  and the N phase with  $S > 0$  are maximally stable at the same time. When  $T < T_c$ , the N phase with  $S > 0$  is the most stable. In this way, the first-order phase transition between the N and Iso phases, in which the order parameter varies discontinuously from  $S = 0$  to  $S > 0$  at the transition temperature  $T = T_c$ , can be described.

---

<sup>5</sup> $T^*$  is the transition temperature for second-order transitions.

In the temperature range  $T^* + C^2/4aD > T > T_c$ , although the Iso phase with  $S = 0$  is the most stable, a metastable N-phase state exists with  $S > 0$  with a local energy minimum. In the range  $T_c > T > T^*$ , while the N phase with  $S = 0$  is the most stable, the Iso phase  $S > 0$  is metastable. When the Iso phase of a LC compound is cooled from sufficiently high temperature to below the transition temperature  $T = T_c$ , the Iso phase sometimes remains due to the energy barrier that blocks access to the N phase. This is called a supercooled state. In contrast, when the N phase is heated to a temperature greater than  $T_c$ , it may not transition to the Iso phase in some situations, which is called the “superheated state.”

### 2.4.2 Nematic–isotropic coexisting phase

Since the N–Iso phase transition is a first-order transition, the equilibrium state is a heterogeneous system with two phases coexisting at the phase transition point. In such a coexisting phase, all the intensive properties coincide in the two phases. Generally, in a system consisting of  $c$  types of materials, the intensive properties are the same in all phases when  $r$  phases coexist with each other, and the Gibbs–Duhem equation must be satisfied in all phases. Therefore, the number  $g$  of intensive properties that can change value independently while maintaining the coexistence state and thermodynamic degrees of freedom, is given by the phase rule

$$g = c + 2 - r. \quad (2.7)$$

In a single-component system with  $c = 1$ ,  $g = 2$  is obtained by the phase rule when  $r = 1$  (i.e., a state consisting of only one phase). This means that temperature and pressure can be varied independently while maintaining a single-phase state. In the coexistence of N and Iso phases, in which  $r = 2$ , the phase rule leads to  $g = 1$ , indicating that the temperature cannot be changed independently once the pressure is fixed. In a two-component system with  $c = 2$ ,



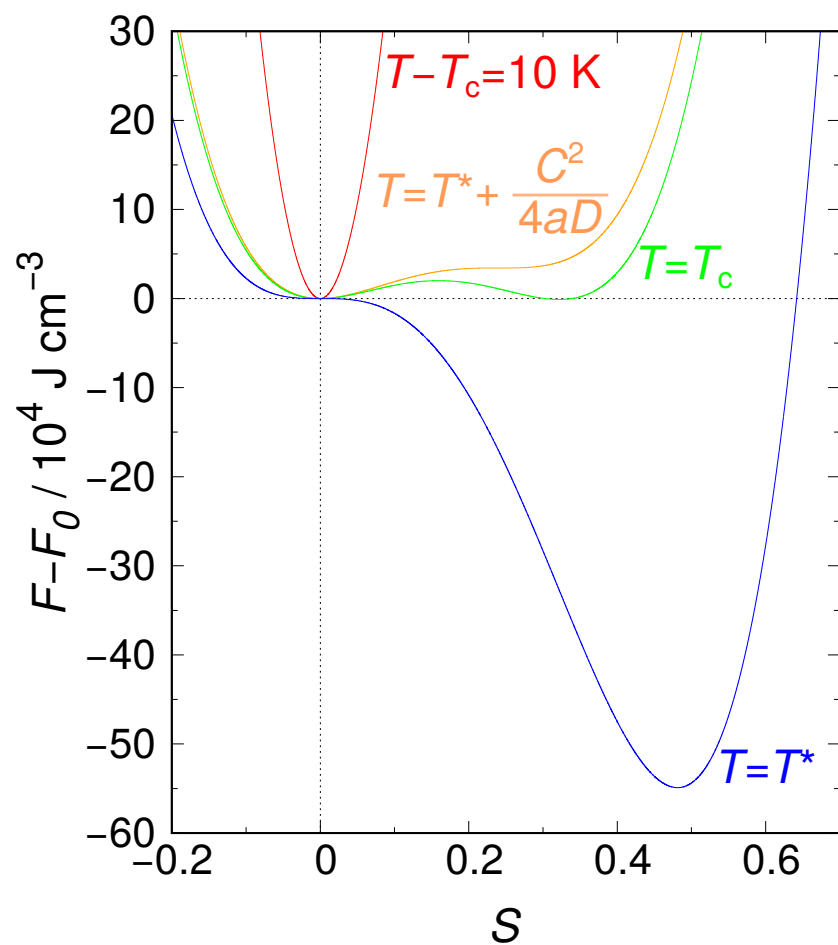


Figure 2.8: Relationship between the order parameter and free energy at each temperature. Specific values of the coefficients of  $a = 0.045 \text{ J}^\circ\text{C}^{-1} \text{ cm}^{-3}$ ,  $T^* = 45.3 \text{ }^\circ\text{C}$ ,  $C/3 = -0.197 \text{ J cm}^{-3}$ , and  $D/4 = 0.307 \text{ J cm}^{-3}$  were substituted into Equations 2.5 and 2.6. These values were obtained for N-(4-Methoxybenzylidene)-4-butylaniline in Reference [53].

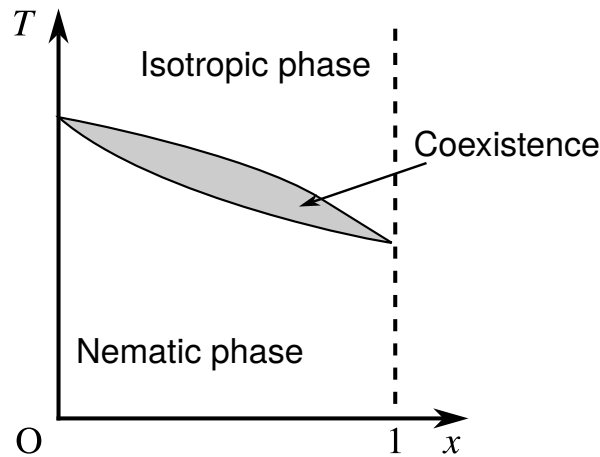


Figure 2.9: Phase diagram in a two-component system. The horizontal axis is the mixing ratio  $x$ , and the vertical axis is temperature. The coexisting phase of isotropic and nematic phases appears in a finite temperature range.

$g = 2$  is given by the phase rule even in the coexisting phase with  $r = 2$ , in which the pressure and temperature can be changed independently while maintaining the coexisting phase. In other words, as shown in Figure 2.9, the phase boundary is not a single line segment but is separated into two line segments so that, for a given pressure and concentration, two-phase coexistence is realized in a finite temperature range.

## 2.5 Elastic theory of nematic phase

### 2.5.1 Orientational elasticity

The N-phase state is determined by the order parameter  $S$  and the director  $\mathbf{n}$ .  $S$  is determined, as explicated in the previous section, to minimize the free energy. Since this basis is also valid for the determination of  $\mathbf{n}$ , the director field is determined to minimize the free energy. However, the free energy cannot be expanded in powers of  $\mathbf{n}$  in the same way as the expansion with  $S$  because  $\mathbf{n}$  is a unit vector and is not infinitesimal in the vicinity of the transition,

unlike  $S$ . In addition, since the Iso phase is the same in any direction,  $\mathbf{n}$  is also equivalent in any directions when it becomes the N phase; thus,  $\mathbf{n}$  cannot be uniquely determined. This is because the average direction of the molecules is considered spatially uniform; that is,  $\mathbf{n}$  does not depend on position. However,  $\mathbf{n}$  actually varies with position, which should be taken into account.

Since the N phase has a liquid-like fluidity, the restoring force, which restores shape deformation and is seen in crystals and elastic materials, is not exerted in the N phase. On the other hand, the N phase has an ordered orientation of the constituent molecules. The restoring force to restore the spatial distortion of the orientational direction is exerted in the N phase due to the orientational elasticity, which is not the case for typical isotropic liquids. The state in which  $\mathbf{n}$  is spatially uniform minimizes the free energy whereas, due to the distortion, the free energy of the nonuniform director field increases. The free energy of the N phase does not depend directly on  $\mathbf{n}$  but on the degree of spatial nonuniformity of  $\mathbf{n}$ .<sup>6</sup>

As shown in Figure 2.10, the director is assumed to be aligned with the  $z$  axis. At positions an infinitesimal distance  $\delta x_i$  from  $\mathbf{n}$ , infinitesimal variations  $\delta n_i$  in  $\mathbf{n}$  are given by the following six independent terms [54, 55]:

$$\begin{aligned}
 \text{Splay : } \quad s_1 &= \frac{\partial n_x}{\partial x}, & s_2 &= \frac{\partial n_y}{\partial y}, \\
 \text{Twist : } \quad t_1 &= -\frac{\partial n_y}{\partial x}, & t_2 &= \frac{\partial n_x}{\partial y}, \\
 \text{Bend : } \quad b_1 &= \frac{\partial n_x}{\partial z}, & b_2 &= \frac{\partial n_y}{\partial z}.
 \end{aligned} \tag{2.8}$$

---

<sup>6</sup>To rigorously treat the free energy of the N phase, the spatial variation of the order parameter  $S$  should also be considered. However, the spatial variation of  $S$  can be neglected here because  $S$  usually depends only on temperature and can be regarded as constant for small spatial variation of the director  $\mathbf{n}$ .

Setting the components of  $\mathbf{n}$  as

$$\begin{aligned}n_x &= a_1\delta x + a_2\delta y + a_3\delta z, \\n_y &= a_4\delta x + a_5\delta y + a_6\delta z, \\n_z &= 1,\end{aligned}\tag{2.9}$$

the infinitesimal variations of  $\mathbf{n}$  are

$$a_1 = s_1, \quad a_2 = t_2, \quad a_3 = b_1, \quad a_4 = -t_1, \quad a_5 = s_2, \quad a_6 = b_2.\tag{2.10}$$

The director  $\mathbf{n}$  does not change its  $z$  component for an infinitesimal tilt because  $\mathbf{n}$  is defined as a unit vector, which is why  $n_z = 1$ .

The quantities  $a_i$  are the spatial derivatives of  $\mathbf{n}$  and denote the degree of spatial nonuniformity of  $\mathbf{n}$ ; the free energy of the N phase should be expanded in powers of  $a_i$ . However, the free energy of the entire system cannot directly be expanded in terms of  $a_i$  because  $a_i$  depend on the position and are the local properties. The local free energy density  $f_d$  is thus introduced to be expanded with  $a_i$ . The free energy density  $f_d$  is defined as

$$f_d = \frac{\delta F}{\delta V},\tag{2.11}$$

where  $\delta V$  is an infinitesimal volume large enough to accurately determine the free energy and small enough to reflect the variation of  $a_i$ , and  $\delta F$  is the free energy in  $\delta V$ . Expanding  $f_d$  in powers of  $a_i$  up to the second order gives <sup>7</sup>

$$f_d = K_i a_i + \frac{1}{2} K_{ik} a_i a_k,\tag{2.12}$$

---

<sup>7</sup>The Einstein summation convention is applied.

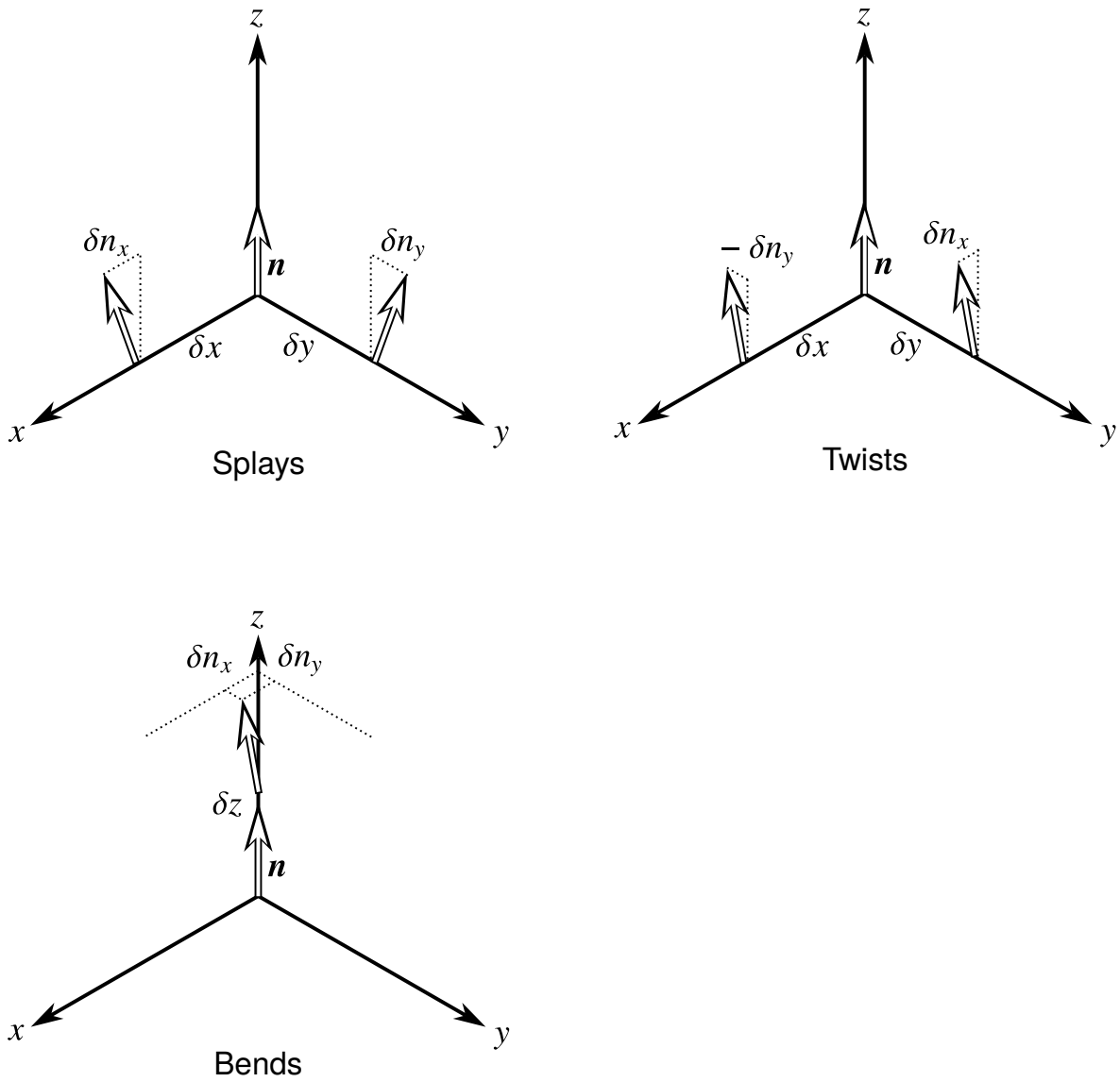


Figure 2.10: Schematic diagrams of the deformations of the director  $\mathbf{n}(\mathbf{r})$ .

where  $K_i$  and  $K_{ik}$  have 6 and 36 independent components, respectively.<sup>8</sup> However, the system symmetry reduces the numbers of the independent components [56]. The rotational symmetry around  $\mathbf{n}$  leads to

$$K_i = \begin{bmatrix} K_1 & K_2 & 0 & -K_2 & K_1 & 0 \end{bmatrix}, \quad (2.13)$$

which has two the independent components. Moreover,  $K_1 = 0$  when the system is apolar, and  $K_2 = 0$  when the system is achiral. All the first-order terms in  $a_i$  are zero for the usual N phase in which  $\mathbf{n} = -\mathbf{n}$ .

In the same way as  $K_i$ , the rotational symmetry around  $\mathbf{n}$  reduces the number of the independent components of  $K_{ik}$  to five;

$$K_{ik} = \begin{bmatrix} K_{11} & K_{12} & 0 & -K_{12} & K_{15} & 0 \\ K_{12} & K_{22} & 0 & K_{24} & K_{12} & 0 \\ 0 & 0 & K_{33} & 0 & 0 & 0 \\ -K_{12} & K_{24} & 0 & K_{22} & -K_{12} & 0 \\ K_{15} & K_{12} & 0 & -K_{12} & K_{11} & 0 \\ 0 & 0 & 0 & 0 & 0 & K_{33} \end{bmatrix}, \quad (2.14)$$

where  $K_{15} = K_{11} - K_{22} - K_{24}$ . Moreover,  $K_{12} = 0$  when the system is apolar or achiral.

These results leads to the following specific form of the free energy introduced by the spatial variation of  $\mathbf{n}$  for the apolar N phase:

$$f_d = K_2(a_2 - a_4) + \frac{1}{2}K_{11}(a_1 + a_5)^2 + \frac{1}{2}K_{22}(a_2 - a_4)^2 + \frac{1}{2}K_{33}(a_3^2 + a_6^2) - (K_{22} + K_{24})(a_1a_5 - a_2a_4). \quad (2.15)$$

---

<sup>8</sup>The numbers of independent components of  $K_i$  and  $K_{ik}$  are actually 9 and 81, respectively. The fact that  $\partial n_x / \partial z = \partial n_y / \partial z = \partial n_z / \partial z = 0$  reduces the numbers to 6 and 36, respectively.

The first term of the right-hand side including  $K_2$  is for the twist deformation, which appears only in the chiral N phase. The fifth term of the right-hand side (including  $K_{24}$ ) can be converted to a surface integration by using Gauss' divergence theorem when the free-energy density is integrated over the entire volume; it is neglected in the form of free-energy density. The resulting form of the free energy density is vectorially expressed as

$$f_d = \frac{1}{2}K_{11}(\nabla \cdot \mathbf{n})^2 + \frac{1}{2}K_{22} \left\{ \mathbf{n} \cdot (\nabla \times \mathbf{n}) + \frac{K_2}{K_{22}} \right\}^2 + \frac{1}{2}K_{33} \{ \mathbf{n} \times (\nabla \times \mathbf{n}) \}^2, \quad (2.16)$$

which is called the ‘‘Frank elastic free energy.’’  $K_{11}$ ,  $K_{22}$ , and  $K_{33}$  are the elastic constants corresponding to the splay, twist, and bend deformations, respectively. A uniform director field, in which the spatial differentials of  $\mathbf{n}(\mathbf{r})$  are zero, minimizes Equation 2.16 for a typical (i.e., apolar and achiral) N phase. In terms of the chiral N phase, since  $K_2 \neq 0$ , the uniform director field does not minimize the free energy. The free energy has the minimum value when

$$\begin{cases} \nabla \cdot \mathbf{n} = 0, \\ \mathbf{n} \cdot (\nabla \times \mathbf{n}) + \frac{K_2}{K_{22}} = 0. \\ \{ \mathbf{n} \times (\nabla \times \mathbf{n}) \}^2 = 0. \end{cases} \quad (2.17)$$

For example, for a uniform helical structure with a helical axis oriented along the  $z$  axis and a wave number  $K_2/K_{22}$ ,

$$\mathbf{n}(\mathbf{r}) = \left( \cos \left( \frac{K_2}{K_{22}} z \right), \sin \left( \frac{K_2}{K_{22}} z \right), 0 \right), \quad (2.18)$$

minimizes the free energy and is a stable structure. This director field corresponds to the Ch phase.

## 2.5.2 Coherence length

The constituent molecules of LCs possess electromagnetic anisotropy, changing their direction upon interaction with external fields such as electric and magnetic fields. The contribution to the free energy  $f_{el}$  of the interaction with an electric field is given by [29]

$$f_{el} = -\frac{1}{2}\mathbf{D} \cdot \mathbf{E} = -\frac{1}{2}\varepsilon_0\varepsilon_{ik}E_iE_k = -\frac{1}{2}\varepsilon_0\varepsilon_{\perp}E^2 - \frac{1}{2}\varepsilon_0\Delta\varepsilon(\mathbf{n} \cdot \mathbf{E})^2, \quad (2.19)$$

where  $\mathbf{E}$ ,  $\mathbf{D}$ , and  $\varepsilon_0$  denote the electric field, the electric displacement field, and the dielectric constant of vacuum, respectively. The quantity  $\varepsilon_{ik} = \varepsilon_{\perp}\delta_{ik} + \Delta\varepsilon n_i n_k$  is the dielectric tensor;  $\Delta\varepsilon = \varepsilon_{\parallel} - \varepsilon_{\perp}$  is the dielectric anisotropy, in which  $\varepsilon_{\parallel} = 1 + \chi_{\parallel}$  and  $\varepsilon_{\perp} = 1 + \chi_{\perp}$ , where  $\chi_{\parallel}$  and  $\chi_{\perp}$  are the parallel and the perpendicular components of the electric susceptibility, respectively. The second term of the rightmost side of Equation 2.19 indicates that the free energy has the minimum value when  $\mathbf{n}(\mathbf{r})$  is parallel to  $\mathbf{E}$  for the positive anisotropy,  $\Delta\varepsilon > 0$ , and when  $\mathbf{n}(\mathbf{r})$  is perpendicular to  $\mathbf{E}$  for the negative anisotropy,  $\Delta\varepsilon < 0$ .

A parameter called the ‘‘coherence length’’ is now introduced to define the thickness of the transitional layer, in which the director field is distorted due to the external fields such as electric and magnetic fields, in the vicinity of the boundary [57]. Let us consider an N phase occupying a half-infinite space  $z > 0$  with the director anchored to the  $x$  direction on the boundary at  $z = 0$ . When a uniform electric field  $\mathbf{E} = (0, E, 0)$  is applied, the angle  $\theta$  between the director and the  $x$  axis must satisfy the equilibrium condition

$$\frac{\partial^2\theta}{\partial z^2} + \frac{1}{\xi^2} \sin\theta \cos\theta = 0, \quad (2.20)$$



where the electric coherence length  $\xi$  is defined by

$$\xi = \sqrt{\frac{K_{22}}{\varepsilon_0 \Delta \varepsilon}} \frac{1}{E}. \quad (2.21)$$

Using the boundary conditions in which  $\varphi \rightarrow \pm\pi/2$  and  $\partial\theta/\partial z \rightarrow 0$  at  $z \rightarrow \infty$  gives

$$\tan\left(\frac{\theta}{2} + \frac{\pi}{4}\right) = \exp\left(\pm\frac{z}{\xi}\right); \quad (2.22)$$

the distortion of the director field due to the external field is small in the distance from  $z = 0$ , in which the director is anchored, to the coherence length  $\xi$ , whereas the director is strongly deformed to orient the direction of the external field in the region of  $z > \xi$ . The orientational elasticity is what prevents the distortion of the director near the boundary. Given that the definition (Equation 2.21) of the coherence length is the ratio of the orientational elastic constant to the magnitude of the molecular field acting on the director by the electric field, a larger external field will shorten the coherence length, so the director is deformed after a short distance. Conversely, the larger the orientational elasticity, the longer the correlation length and the further from the boundary the director is kept without deformation.

### 2.5.3 Extrapolation length

Extending the discussion above, let us consider the case in which a wall also exists at  $z = d$ . The N phase occupies the region  $0 \leq z \leq d$ . The director is assumed to be fixed in the  $x$  direction at the boundaries  $z = 0$  and  $z = d$ . The previous discussion considers the situation where the director at the boundary is not affected by the application of an external field. Such anchoring is called “strong.” In contrast, situations exist in which the application of an external field changes slightly the orientation at the boundaries, which is called “weak”

anchoring. Under weak anchoring, when the director rotates by a finite angle  $\theta$  from the anchored direction, the free energy per unit surface at the boundary increases by

$$f_{\text{anc}} = \frac{1}{2}A \sin^2 \theta, \quad (2.23)$$

where  $A$  is the anchoring strength per unit surface.

The torque balance in the bulk, given by Equation 2.20, remains valid under weak anchoring. In this case, the boundary conditions are obtained by the torque balance at the interfaces:

$$\begin{aligned} K_{22} \left( \frac{\partial \theta}{\partial z} \right)_{z=0} &= A\theta(0), \\ K_{22} \left( \frac{\partial \theta}{\partial z} \right)_{z=d} &= -A\theta(d). \end{aligned} \quad (2.24)$$

Assuming  $\theta(z)$  to be sufficiently small, I use  $\sin \theta \simeq \theta$  and  $\cos \theta \simeq 1$  in Equation 2.20, which gives

$$\theta(z) = \theta \left( \frac{d}{2} \right) \sin q(z + b). \quad (2.25)$$

Substituting the solution (Equation 2.25) into the boundary conditions (Equation 2.24) gives

$$\begin{aligned} q \frac{K_{22}}{A} &= \tan(qb), \\ -q \frac{K_{22}}{A} &= \tan q(d + b). \end{aligned} \quad (2.26)$$

$q = \pi/(d + 2b)$  is obtained from the consistency of Equation 2.26; when  $qb \ll 1$ ,  $b$  is given by

$$b = \frac{K_{22}}{A}. \quad (2.27)$$

The condition for the existence of the nonzero solution,  $\theta(z) \neq 0$ , is given by

$$\left(\frac{\pi}{d+2b}\right) = \frac{1}{\xi^2}, \quad (2.28)$$

which leads to the critical electric field

$$E_c = \frac{\pi}{d+2b} \sqrt{\frac{K_{22}}{\varepsilon_0 \Delta \varepsilon}}. \quad (2.29)$$

This critical value separates the stable states of the director.  $\theta(z) \equiv 0$  is the only solution under the electric field of  $E < E_c$ , whereas a solution exists with a finite deformation under the electric field of  $E > E_c$ , and  $\theta(z) = 0$  becomes unstable. Such a phenomenon is called the ‘‘Fréedericksz transition’’ [58–60].

Given that  $b = 0$  in Equation 2.25 under strong anchoring, the effect on the critical electric field of weak anchoring at the boundary is equivalent to an increase in the thickness  $d$  of the LC to  $d + 2b$ . In other words, a hypothetical strong-anchoring boundary is assumed to exist a distance  $b$  from the weak-anchoring boundary to the exterior of the LC. For this reason, the parameter  $b$  defined by Equation 2.27 is called the ‘‘extrapolation length.’’ The anchoring strength can be quantitatively evaluated by using the extrapolation length. The anchoring is assumed to be strong when  $d \gg b$ , and  $b$  is negligible compared with  $d$  for the required accuracy. When  $b$  is not negligible compared with  $d$ , the anchoring is assumed to be weak.

# Chapter 3

## The Lehmann Effect

### 3.1 Discovery and reproduction of the Lehmann effect

The mirror symmetry breaking in the N phase, which has long-range order not in the position but only in the orientation of the constituent molecules, causes the twist deformation of the director field produce chiral LC phases such as Ch and blue phases. Chirality strongly affects not only the static structure but also the dynamic properties of LC phases. One such dynamic phenomena in the Ch phase is the Lehmann effect.

In 1900, Lehmann observed LC droplets dispersed in a solvent put on a heating stage under a polarizing microscope and discovered that the droplet texture changes [5, 6]. Lehmann interpreted the phenomenon as rotation driven by a heat flux because the droplets were strongly heated from the bottom; he argued that the textural rotation is not a true rotation of mass, but a rotation due to an optical effect. <sup>1</sup> In other words, Lehmann believed that the rotation is pure director rotation. The details of Lehmann's experiment is unknown because specific information such as the experimental conditions and movies of the rotation was not

---

<sup>1</sup>I am indebted to Professor Helmut R. Brand for the interpretation of the original German article.



Figure 3.1: Lehmann’s drawings of deformed texture of a liquid crystal droplet under a temperature gradient. This figure is reproduced from Reference [5].

conserved [61]. Drawings of the texture of the droplets by Lehmann are reproduced from Reference [5] in Figure 3.1.

This phenomenon, in which the rotation of chiral LCs or the deformation of the director of chiral LCs is driven by flows, is called the Lehmann effect. Although some refer to the rotation of Ch droplets driven by a heat flux only as the Lehmann effect [61], in this dissertation, I use “Lehmann effect” to refer to all the phenomenon in which the unidirectional steady rotation or the deformation of chiral LCs is driven by any flows.

In 1982, Éber and Jánossy reproduced the Lehmann effect, estimating the coupling constant between the heat flux and the torque [62]. Dynamic rotation was not observed in this experiment; only observed was the static deformation in the director field of the bulk of Ch LC induced by cross coupling between a heat flux and torque. Based on the observed deformation, the coupling constant was quantitatively estimated from the balance between the orientational elasticity and the torque induced by the Lehmann effect. This was the first confirmation of cross coupling between a heat flux and torque since Lehmann’s experiment.

In 1987, Madhusudana and Pratibha observed a unidirectional rotation of Ch droplets driven by a DC current [63]. This was the first experiment reproducing the rotation of Ch droplets driven by a flux (although not a heat flux) since the original experiment. In the experiment of Madhusudana and Pratibha, the Ch compound was sandwiched between two glass substrates with transparent electrodes and was maintained in the coexisting phase

of the Ch and Iso phases. Upon applying a DC current, the texture of the Ch droplets underwent a unidirectional rotation. Figure 3.2 shows polarizing microscopy images of Ch droplets coexisting with their Iso phase, reproduced from Reference [63]. Figure 3.2a shows Ch droplets sandwiched in a 150- $\mu\text{m}$ -thick gap between glass substrates under a polarizing microscope with crossed polarizers. The dark region is the Iso phase, which is not optically anisotropic, and the bright fields are almost-spherical Ch droplets. Figures 3.2b–3.2h show image sequences of a Ch droplet sandwiched in an 8- $\mu\text{m}$ -thick gap between glass substrates under a polarizing microscope. The Iso phase does not look dark because the polarizers are rotated  $20^\circ$  from a right angle. The Ch droplets in the center of each image are no longer spherical but are thin cylinders because they are confined to an 8- $\mu\text{m}$ -thick region. Figure 3.2b was acquired without applying an electric field. Figures 3.2c, 3.2e, and 3.2g are snapshots taken every 30 s while a voltage of 2 V was applied across the glass substrates (i.e., perpendicular to the page). Notice that the texture of the droplet rotates clockwise. Figures 3.2d, 3.2f, and 3.2h are snapshots taken when the sign of the voltage was reversed, so the droplet has rotated counterclockwise. This result clarifies that the steady electric-current-induced unidirectional rotation of Ch droplets is reversed upon reversing the direction of the flow. In addition, the direction of rotation of the droplet also reversed upon reversing the chirality of the Ch LC, and the rotational velocity was proportional to the applied voltage. The reversal of the direction of rotation upon reversing the flow or chirality and the linearity of the rotational velocity with respect to the driving force are major features of the Lehmann effect.

In 2003, Tabe and Yokoyama discovered that a chiral Langmuir monolayer formed on glycerol rotates unidirectionally due to the transport of water vapor [64]. This is the first study to observe the Lehmann effect driven by a mass flow. Figure 3.3 is reproduced from Reference [64] and shows a Brewster-angle microscopy images of a monolayer of a chiral

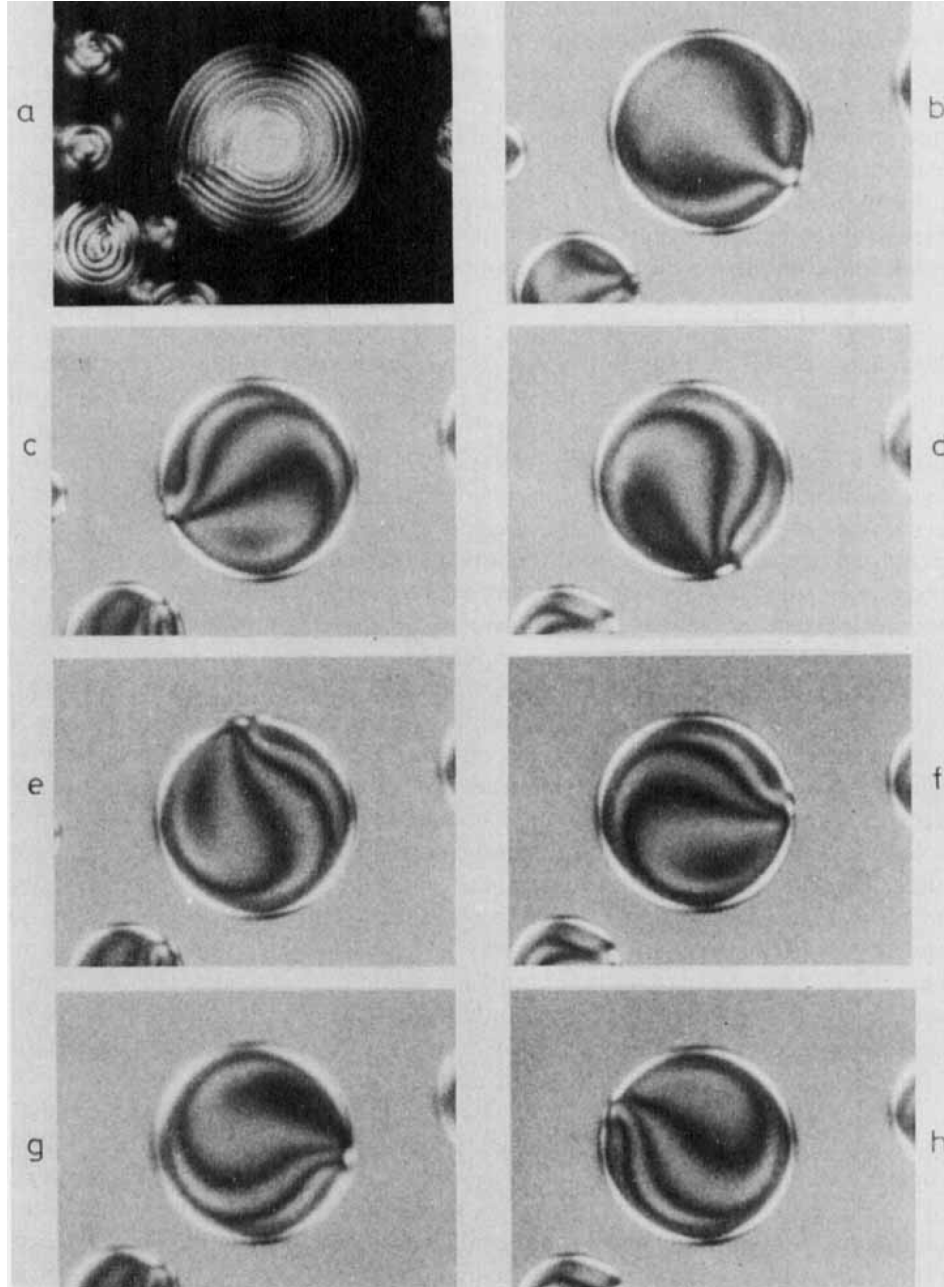


Figure 3.2: Images of cholesteric droplets coexisting with their isotropic phase under a polarizing microscope with (a) crossed polarizers and (b)–(h) polarizers crossed by  $20^\circ$  from a right angle. Panel (a) shows cholesteric droplets sandwiched in a  $150\text{-}\mu\text{m}$ -thick gap between glass substrates. Panels (b)–(h) show an image sequence of a cholesteric droplet sandwiched in an  $8\text{-}\mu\text{m}$ -thick gap between glass substrates. Panel (b) was acquired without an electric field. Panels (c), (e), and (g) show snapshots taken every 30 s with 2 V applied across the glass substrates (i.e., perpendicular to the page). Panels (d), (f), and (h) show snapshots when the sign of the voltage is reversed. This figure is reproduced from Reference [63].

LC on glycerol taken every 4 s. The Brewster-angle microscope is a reflective microscope optimized to observe monolayers [65–67]. As shown in Figure 3.3, a concentric-circle texture of the monolayer spreads outward over time from the center to the edge. This textural change indicates that water vapor flowing vertically through the monolayer drives the unidirectional steady rotation of the chiral molecules that compose the monolayer. In the study, as in the case of the electric-current-induced Lehmann effect, the direction of rotation reverses when either the flow direction or chirality is reversed (the direction of rotation does not change when both are reversed), and the rotational velocity is proportional to the flow velocity, reproducing the characteristics of the Lehmann effect.

The rotation of Ch droplets due to a heat flow, as observed by Lehmann himself, had not been reproduced for about 100 years after its discovery. In 2008, however, Oswald and coworkers succeeded in reproducing it in a system where the conditions can be controlled quantitatively [68]. Figure 3.4 is reproduced from Reference [68], showing a Ch droplet coexisting with its Iso phase. The droplet has a striped texture, which is considered to correspond to the fingerprint texture shown in Figure 2.6a; the helical axis of the director field inside the droplet is perpendicular to the striped droplet, and the director rotates by  $\pi$  from one stripe to the next. Such a droplet is called a “striped droplet.” The unidirectional rotation of the striped droplet was driven by applying a temperature gradient to the droplet by independently controlling the temperatures at the top and bottom (which correspond to the back and front of the page) of the glass cell containing the LC compound. The study led to a quantitative analysis of the heat-flow-driven rotation and revealed that the rotational velocity is proportional to the temperature gradient and inversely proportional to the square of the droplet diameter.

Since then, the Lehmann effect in Ch–Iso coexisting phases has been studied extensively [69–83].



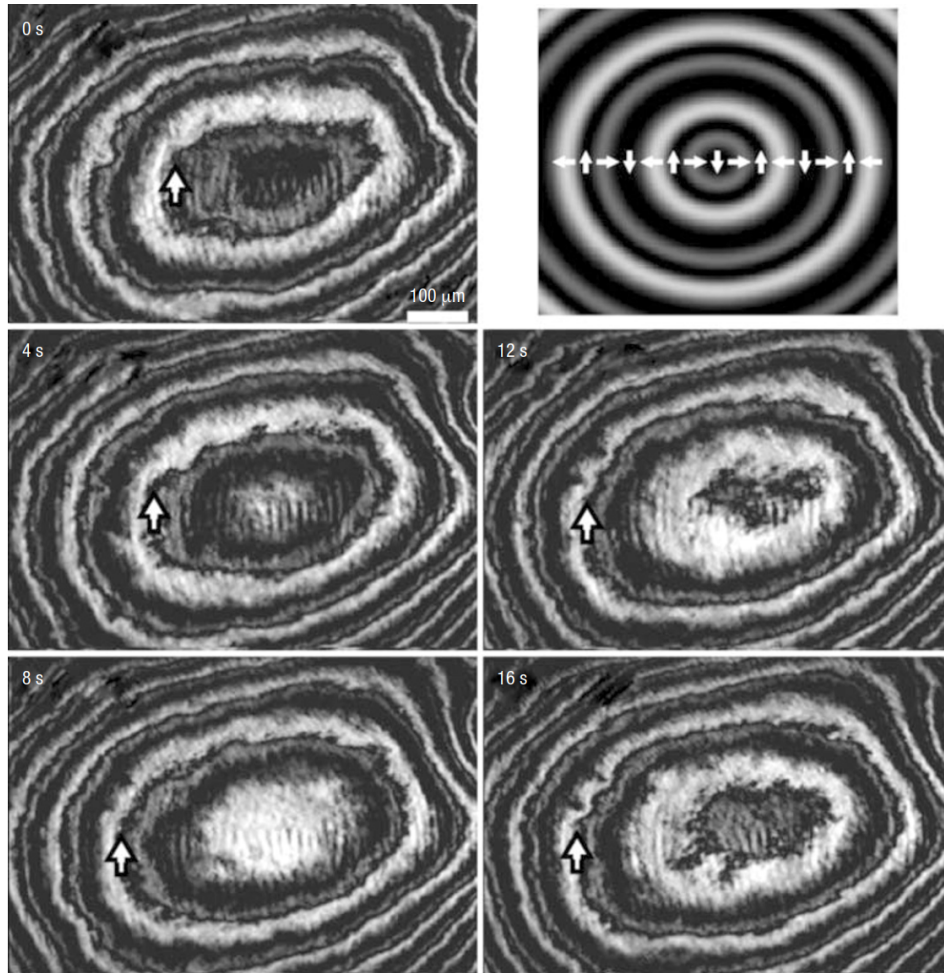


Figure 3.3: A sequence of Brewster-angle microscopy images of a chiral liquid-crystal monolayer on glycerol at 45% relative humidity and room temperature. The snapshots were acquired every 4 s, and the scale bar indicates 100  $\mu\text{m}$ . The rotation of the director is driven by water vapor flowing vertically through the monolayer. The top-right image is the corresponding simulation. This figure is reproduced from Reference [64].

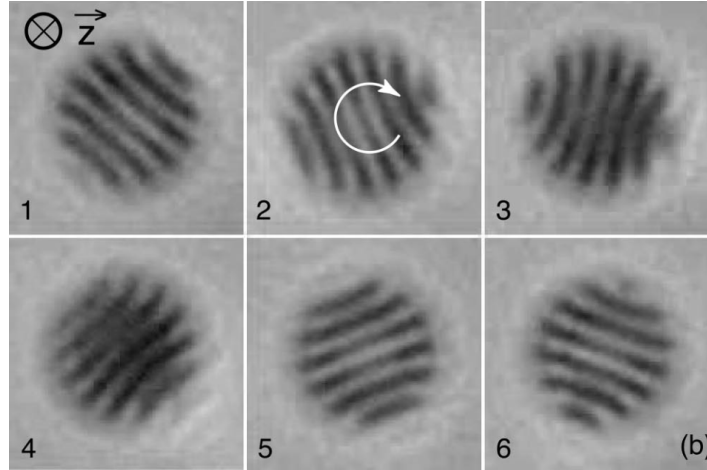


Figure 3.4: A sequence of optical microscope images of a cholesteric droplet coexisting with its isotropic phase under a temperature gradient. This figure is reproduced from Reference [68].

## 3.2 Phenomenological description

The phenomenological interpretation was first given by Leslie in 1968 [84]. Considering the symmetry and the conservation laws, Leslie showed phenomenologically the cross coupling between a heat flux and torque. Since Leslie theory is phenomenological, it does not mention the microscopic interaction between molecules and heat flow that causes the Lehmann effect; to this day, the microscopic mechanism remains to be clarified. However, some studies reproduce the Lehmann effect of Ch LCs by molecular dynamics simulations [85–89]. In this section, I introduce the phenomenological theory of Leslie.

The director of the ordinary N phase is uniformly oriented in the ground state. In practice, however, the interface between the LC and the container in which the LC is placed for observation affects the director and the free interfaces and surfaces. In other words, the existence of an interface deforms the director of the static LC phase. Under the given boundary conditions, it is necessary to find an equation describing the equilibrium distribution

of  $\mathbf{n}(\mathbf{r})$  [90–92]. The total free energy of the system,

$$F = \int f dV, \quad (3.1)$$

should be minimized under the condition  $\mathbf{n}^2 = 1$ . The variation of the free energy should be zero by the method of Lagrange multipliers;

$$\delta \int \left\{ f - \frac{1}{2} \lambda(\mathbf{r}) \mathbf{n}^2 \right\} dV = 0, \quad (3.2)$$

where  $\lambda(\mathbf{r})$  is an arbitrary function. Putting  $\delta \mathbf{n} = \mathbf{0}$  at the interfaces, the variation of the total free energy is given by

$$\delta F = - \int \mathbf{H} \delta \mathbf{n} dV. \quad (3.3)$$

$\mathbf{H}$  is called the “molecular field” and has the components of <sup>2</sup>

$$H_i = \partial_k \pi_{ki} - \frac{\partial f}{\partial n_i}, \quad \pi_{ki} = \frac{\partial f}{\partial (\partial_k n_i)}. \quad (3.4)$$

$\mathbf{H} = -\lambda \mathbf{n}$  is satisfied in the equilibrium state (i.e., the state in which  $\mathbf{H}$  and  $\mathbf{n}$  are parallel to each other), leading to

$$\mathbf{h} \equiv \mathbf{H} - \mathbf{n}(\mathbf{n} \cdot \mathbf{H}) = 0. \quad (3.5)$$

Here, the vector  $\mathbf{h}$ , which satisfies  $\mathbf{n} \cdot \mathbf{h} = 0$ , is introduced.

The dynamic state of the N phase is described by the spatial distribution of the director  $\mathbf{n}$ , the density  $\rho$ , the velocity  $\mathbf{v}$ , and the entropy density  $s$ . Corresponding to this, the equations of motion of the N phase consist of four equations that give the temporal differentials of these four physical quantities [28, 93–100]. Since the detailed derivation of the equations are

---

<sup>2</sup>The spatial derivatives  $\partial/\partial x_i$  are abbreviated to  $\partial_i$ .

explicated in the references, I mention only the results.

The general form of the equation of motion for the director is

$$\frac{dn_i}{dt} = \Omega_{kl}n_k + \lambda'(\delta_{il} - n_in_l)n_kA_{kl} + N_i, \quad (3.6)$$

where  $d/dt$  is the Lagrange derivative  $\partial/\partial t + (\mathbf{v} \cdot \nabla)$ ; the symmetrical and antisymmetric components of the velocity gradient tensor  $\partial_iv_j$  are denoted by  $A_{ij} \equiv (\partial_iv_j + \partial_jv_i)/2$  and  $\Omega_{ij} \equiv (\partial_iv_j - \partial_jv_i)/2$ , respectively.  $N$  is a vector defined as  $N \equiv \mathbf{h}/\gamma$ , where the coefficient  $\gamma$  has the dimensions of viscosity, and the coefficient  $\lambda'$  is dimensionless.

The equation for the density is given by the continuity equation;

$$\frac{\partial \rho}{\partial t} + \text{div}(\rho \mathbf{v}) = 0. \quad (3.7)$$

The equation for the velocity is given by the equation of motion. Body forces can be written as the divergence of the stress tensor  $\sigma_{ik}$ , so  $\rho dv_i/dt = \partial_k \sigma_{ik}$ , which gives

$$\rho \left( \frac{\partial v_i}{\partial t} + (\mathbf{v} \cdot \nabla)v_i \right) = -\partial_i p + \partial_k \sigma_{ik}^r + \partial_k \sigma'_{ik}. \quad (3.8)$$

Here,  $p$  is the pressure, and  $\sigma_{ik}^r$  and  $\sigma'_{ik}$  are defined as

$$\sigma_{ik}^r \equiv -\frac{\lambda'}{2}(n_i h_k + n_k h_i) - \frac{1}{2}(\pi_{kl}\partial_i n_l + \pi_{il}\partial_k n_l) - \frac{1}{2}\partial_l \{(\pi_{ik} + \pi_{ki})n_l - \pi_{kl}n_i - \pi_{il}n_k\}, \quad (3.9)$$

$$\sigma'_{ik} \equiv \sigma_{ik} - \sigma_{ik}^r + p\delta_{ik}. \quad (3.10)$$

The equation for the entropy density is given by the continuity equation taking the dissipation process into account,

$$\frac{\partial s}{\partial t} + \text{div} \left( s\mathbf{v} + \frac{\mathbf{J}_q}{T} \right) = \frac{2R}{T}. \quad (3.11)$$

Here,  $R$  is called the dissipation function and is of quadratic form. It is composed of  $v_{ik}$ ,  $\mathbf{h}$ , and  $\nabla T$ :

$$2R = \sigma'_{ik} A_{ik} + \mathbf{N} \cdot \mathbf{h} + \mathbf{J}_q \cdot \left( -\frac{\nabla T}{T} \right). \quad (3.12)$$

$\mathbf{J}_q$  denotes the heat flux density, which has the components

$$J_{q,i} = -\kappa_{ik} \partial_k T. \quad (3.13)$$

$\kappa_{ik}$  is the thermal conductivity tensor and is represented as

$$\kappa_{ik} = \kappa_{\parallel} n_i n_k + \kappa_{\perp} (\delta_{ik} - n_i n_k), \quad (3.14)$$

where  $\kappa_{\parallel}$  and  $\kappa_{\perp}$  are the thermal conductivities parallel and perpendicular to the director, respectively.

The above discussion is for the N phase, and mirror symmetry is not invoked in deriving these equations. Therefore, these equations can be applied to the Ch phase as well, although some modifications are necessary. In other words, several terms should be added to  $\sigma'_{ik}$ ,  $\mathbf{J}_q$ , and  $\mathbf{h}$  [84]:

$$\sigma'_{ik} = (\sigma'_{ik})_{\text{nem}} + \mu (n_i \varepsilon_{klm} + n_k \varepsilon_{ilm}) n_m \partial_l T, \quad (3.15a)$$

$$h_i = (h_i)_{\text{nem}} + \nu \varepsilon_{ikl} n_k (-\partial_l T), \quad (3.15b)$$

$$J_{q,l} = (J_{q,l})_{\text{nem}} + \nu_1 \varepsilon_{lki} n_k n_i + \mu_1 (\varepsilon_{lmi} n_k + \varepsilon_{lmk} n_i) n_m A_{ik}. \quad (3.15c)$$

The subscript ‘‘nem’’ identifies the terms for the N phase. These added terms are not polar vectors nor polar tensors but are axial vectors or axial tensors, which change their sign with respect to space inversion and reflection, which are absent from the N phase.

The coefficients appearing in the added terms are related to each other by the Onsager reciprocal relations [101, 102]. Considering  $\sigma'_{ik}$ ,  $J_{q,i}$ , and  $h_i$  as the thermodynamic fluxes, the corresponding thermodynamic forces are  $-A_{ik}/T$ ,  $\partial_i T/T^2$ , and  $-N_i/T$ , respectively. From Equations 3.6, 3.8, and 3.11,  $\sigma'_{ik}$  should be even, and  $q_i$  and  $h_i$  should be odd with respect to time reversal. Noting this, the comparison of the coefficients in Equation 3.15 yields

$$\nu_1 = \nu T, \quad \mu_1 = \mu T. \quad (3.16)$$

Finally, Equation 3.15 in vector form is

$$\sigma'_{ik} = (\sigma'_{ik})_{\text{nem}} + \mu [n_i (\mathbf{n} \times \nabla T)_k + n_k (\mathbf{n} \times \nabla T)_i], \quad (3.17a)$$

$$\mathbf{h} = \mathbf{h}_{\text{nem}} + \nu \mathbf{n} \times (-\nabla T), \quad (3.17b)$$

$$\mathbf{J}_q = (\mathbf{J}_q)_{\text{nem}} + \nu T \mathbf{n} \times \mathbf{N} + 2\mu T \mathbf{n} \times (\mathbf{n} \mathbf{A}). \quad (3.17c)$$

Equation 3.17b indicates that a heat flux applied to the Ch phase induces a Lehmann torque of

$$\boldsymbol{\tau} = \nu \mathbf{n} \times \mathbf{n} \times (-\nabla T) \quad (3.18)$$

on the director, where  $\nu$  is the cross-coupling constant between the heat flux and torque, which is a physical property determined by the details of the material and the chirality. In contrast, Equation 3.17c suggests the existence of an inverse Lehmann effect for which applying torque  $\boldsymbol{\tau}$  would induce the heat flux  $\mathbf{J}_q = \nu T \boldsymbol{\tau} / \gamma$  [103].

de Gennes later summarized this argument [29], assuming some conditions to argue about the rotation driven by the Lehmann effect:

1. A Ch droplet is sandwiched between two parallel flat glass substrates. The director is parallel to the substrates and can rotate freely while remaining parallel to the substrates.

This assumption of the boundary condition makes the helical axis perpendicular to the substrates and parallel to the heat flux.

2. The droplet is cylindrical and the contribution of the side interfaces is completely negligible.
3. There is no flow; the constituent molecules do not move; only the direction rotates.

Considering these assumptions, the director exhibits a steady unidirectional rotation with a rotational velocity of

$$\omega_0 = \frac{\nu|\nabla T|}{\gamma}. \quad (3.19)$$

In the above argument, a heat flux is considered as a flux to drive the Lehmann effect, and a temperature gradient as a conjugate field. From a phenomenological point of view, however, a flux is not necessarily a heat flux. For example, considering a electric current  $\mathbf{J}_e$  as a flux and  $-\nabla V$ , in which  $V$  is the electric potential, as a conjugate field, the argument remains valid. Taking a mass flux  $\mathbf{J}_m$  as a flux, as another example, a conjugate field would be  $-\nabla\mu$ , where  $\mu$  is the chemical potential. The conjugate field of a heat flux  $\mathbf{J}_q$  should be taken as  $-\nabla T/T$  so that the units of the coupling constants for all cases are the same. Note that the units of the coupling constant are not always taken in the same way, and that comparison of the values of the coupling constant may cause inconsistency unless considering the difference in its unit. Since only a heat flux is applied in this study, I take the field as  $-\nabla T$ .

### 3.3 The inverse Lehmann effect

In contrast to the Lehmann effect, in which torque is exerted on Ch LCs, the existence of a phenomenon that corresponds to the inverse process is implied in Equation 3.17c. The inverse Lehmann effect should generate a heat flux when the Ch LCs are rotated. The inverse

Lehmann effect is expected to be applied to a microscopic heat pump. In 2017 Sato et al. investigated the inverse Lehmann effect by rotating Ch droplets coexisting with their Iso phase and measuring the temperature along the rotational axis of the droplets [104]. The measurements revealed a temperature gradient proportional to the angular velocity of the droplets along the rotational axis of the droplets. In addition, the direction of the temperature gradient was inverted by reversing either chirality or the rotational direction of the droplets. However, the coupling constant for the inverse Lehmann effect estimated by this experiment was four orders of magnitude larger than that for the Lehmann effect. The coupling constants for the Lehmann and the inverse Lehmann effects should be the same due to the Onsager reciprocal relations, so further study and discussion is necessary.

### **3.4 Director rotation and rigid-body rotation**

As described in Chapter 1, one of the intriguing subjects in terms of the rotation of the Ch droplets driven by the Lehmann effect is the detailed rotational motion of the constituent molecules. Since the polarizing microscopy image reveals the temporal variation in the optical anisotropy due to the rotation of Ch droplets, it does not directly reveal the motion of the molecules. Molecules can undergo two independent types of rotational motion. One is “director rotation,” whereby molecules rotate only in the orientational direction without moving their center of mass, and the other is the “rigid-body rotation,” whereby molecules orbit around the center axis of the droplet rotation while maintaining their relative orientational structure. The change in the droplet texture is thought to be caused by one of these independent rotations or a combination of both. Director rotation involves no translational motion of the molecules, and thus no hydrodynamic flow is associated with the rotation. Rigid-body rotation, however, involves molecules orbiting with translational motion of the center of mass,



so flow should be generated. Lehmann himself believed that textural change was due to director rotation [5, 6]. Moreover, the possibility of the rigid-body rotation has never been discussed by theorists such as Leslie or de Gennes [29, 84].

In recent years; however, experimental results that suggest the possibility of rigid-body rotation have been reported. In 2014, Yoshioka et al. measured the flow inside a Ch droplet rotating due to the Lehmann effect and attempted to reveal the details of the rotational motion of the constituent molecules [72]. The experiment used the method of fluorescence recovery after photobleaching (FRAP), whereby a fluorescent dye is added to the Ch LC sample and a small region of the interior of the Ch droplet is photobleached by irradiating with a strongly focused laser beam while the entire sample is weakly excited by optical excitation. Without flow, the photobleached fluorescent dye diffuses according to the diffusion equation, and the fluorescence gradually returns to the bleached region. Conversely, if flow is present, the motion of the photobleached dye follows the convection–diffusion equation, and the center of the photobleached region moves with the flow as it diffuses. Figure 3.5 shows microscopic images of the FRAP measurement applied to a Ch droplet dispersed in the Iso phase (reproduced from Reference [72]). The green color of the entire image is due to the fluorescence of the dye. Figure 3.5a shows images of a striped droplet characterized by its striped texture, and the helical axis of the director is orthogonal to the heat flow. The left image is before photobleaching by laser irradiation, and the right image is after photobleaching. In the image after irradiation, the fluorescent dye in the laser-irradiated area has been photobleached, resulting in a dark-field spot. Tracking the position of the center of the photobleached area over time shows that it moves at the same velocity as the rotation of the droplet texture. Yoshioka et al. concluded that the rotation of the striped droplet corresponds to rigid-body rotation accompanied with a vortexlike flow.

In contrast, Figure 3.5b shows a droplet with a director field whose helical axis is parallel

to the heat flow. It is called a concentric-circle (CC) droplet because it has a concentric-circle texture. The left side is before photobleaching and the right side is after photobleaching. Tracking the position of the center of the photobleached region shows that no flow occurs, despite the rotation of the droplet. This suggests that the center of mass of the molecules comprising the droplet does not move, indicating director rotation. The reason the striped droplet undergoes rigid-body rotation whereas the CC droplet undergoes director rotation, was pointed out at this stage as orientational elasticity. When a heat flow is applied parallel to the helical axis of droplets with uniaxial helical structure, the helical structure is not distorted even by a spatially and temporally uniform director rotation around the heat flow. However, when a uniform director rotation occurs around the heat flow perpendicular to the helical axis, the helical structure is distorted, resulting in loss of elastic energy.

In 2016, Poy and Oswald used the FRAP method to reproduce the same experiment to measure the flow associated with Lehmann rotation of striped CC droplets [75]. In this experiment, measurements were made on almost the same LC samples and experimental system as in Reference [72]. The flow field in the Iso phase in the vicinity of the rotating striped droplet and inside the rotating CC droplet were measured. Despite the same experiments being done, contradictory results were obtained; no flow was detected for both types of droplets. The authors concluded that both types of droplets undergo director rotation and point out that rigid-body rotation due to the Lehmann effect is not driven in principle [61]. Thus, most previous studies argue that Ch droplets undergo director rotation driven by the Lehmann effect, and some previous studies argue strongly against such rigid-body rotation.

Furthermore, flow measurements of striped droplets not only are inconsistent but also several inconsistent results are obtained for the droplet size dependence of the rotational velocity. The Lehmann torque, given by Equation 3.18, is the torque per unit volume acting on the director. Since the moment of inertia of the director is negligible, the rotational

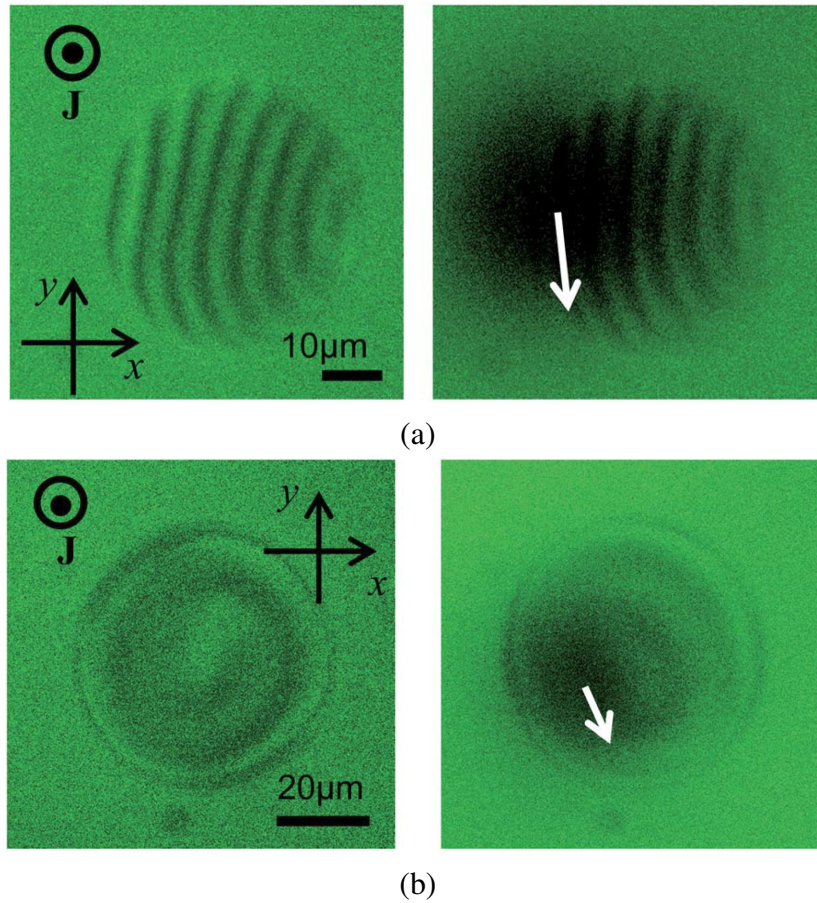


Figure 3.5: Flow-field measurement by the fluorescence recovery after photobleaching method for (a) a striped and (b) a concentric-circle droplet.  $\mathbf{J}$  and the white arrows indicate a heat flux and the direction of rotation, respectively. The scale bars indicate (a)  $10\ \mu\text{m}$  and (b)  $20\ \mu\text{m}$ . The magnitude of the temperature gradient was (a)  $6.3\ \text{mK}\ \mu\text{m}^{-1}$  and (b)  $6.0\ \text{mK}\ \mu\text{m}^{-1}$ . This figure is reproduced from Reference [72].

viscosity of the director is balanced by the Lehmann torque in the steady state. Considering that the rotational viscosity also acts per unit volume with respect to the director, the effect of the droplet volume should cancel out, and the rotational velocity should be independent of the droplet size, as shown in Equation 3.19. In other words, as long as the droplets undergo director rotation, the droplet size should be independent of rotation velocity. For rigid-body rotation, in contrast, the Lehmann torque is exerted on a unit volume, whereas the viscous friction acts on the droplet surfaces, not on the volume, so the rotational velocity should depend on the droplet size. Several groups have reported that the rotation velocity of striped droplets depends on droplet diameter, although both director rotation and rigid-body rotation have been reported [68,72,74]. No report has yet claimed that the rotational velocity of striped droplets is independent of droplet diameter. For CC droplets, all publications argue that director rotation is driven by the Lehmann effect. In addition, rigid-body rotation of CC droplets has never been reported. Despite the consistent reports concerning the rotational motion of CC droplets, some works report that rotational velocity does not depend on droplet diameter [72, 74], whereas other works report that velocity depends on droplet diameter [69, 71, 73]. Thus, the question of whether rigid-body rotation of Ch droplets can be driven is intriguing and important not only for physics but also for applications of the Lehmann effect. Unfortunately, it has been unresolved and controversial for a long time due to many conflicting reports.

Rigid-body rotation of a LC droplet in an isotropic fluid is not unusual when an external torque is applied to the droplet. A well-known example is the rigid-body rotation of N or Ch droplets dispersed in an aqueous solution when trapped by a polarized laser beam [105–107]. Figure 3.6 shows microscope images of N droplets dispersed in pure water (reproduced from Reference [106]). A dye is added to the droplets, and the droplets are trapped by a linearly polarized laser beam. The images show clearly that the smaller droplet unidirectionally orbits the larger droplet. Irradiation by the polarized laser beam applies a torque to the droplets; the

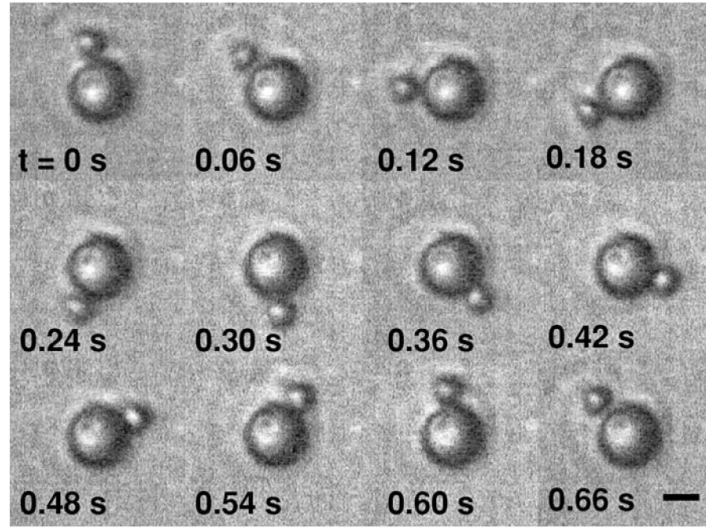


Figure 3.6: Sequence of microscopy images of nematic droplets dispersed in pure water. The droplet is trapped by polarized laser beam perpendicular to the paper. The snapshots were acquired every 0.06 s, and the scale bar indicates 1  $\mu\text{m}$ . This figure is reproduced from Reference [106].

revolution of the smaller droplet is driven by a vortexlike flow accompanied by the rotation of the larger droplet. The existence of the vortexlike flow indicates the translational motion of the position of the constituent molecules, proving the rigid-body rotation of the larger droplet. The reason the droplet is driven in rigid-body rotation is the large rotational viscosity of the N droplet, the orientational elasticity inside the droplet, and the anchoring of the droplet–fluid interface [106]. Since the anchoring strength at the LC–Iso interface is almost the same magnitude as that at the LC–water interface [22, 108], in analogy with rigid-body rotation of N droplets in water, the Lehmann effect should drive the rigid-body rotation of Ch droplets coexisting with their Iso phase even when the sources of torque differ completely.

# Chapter 4

## Direct Observation of Rigid-Body Rotation Driven by the Lehmann Effect

### 4.1 Purpose

The FRAP measurements of the flow field [72, 75] produced inconsistent results for striped droplets. For CC droplets, for which no flow was detected by FRAP in any of the reports and which was concluded to be director rotation, the reports on the dependence of the rotational velocity on droplet size are inconsistent [68, 72, 74]. FRAP is such a delicate method that it might be inappropriate for this type of experimental system.

In this chapter, I report the results of experiments in which I measured flow using a method other than FRAP. Specifically, tracer particles were added to LC samples, and the flow was visualized by tracking their movement. The purpose of the experiments was to directly observe the flow associated with the rotation of Ch droplets by the movements of the particles and to clarify whether the rotation of the droplet is director rotation or rigid-body rotation [81, 83]. Flow observation using particles has attracted attention as a efficacious

method for this system, and some attempts have already been made to add particles to LC samples for this purpose. However, because the interfacial energy between the LC and the glass substrates of the cell in which the LC is sandwiched is on the order of several tens of  $\text{mN m}^{-1}$ , the added particles adsorb onto the glass substrates. I experimented with changing the physical and chemical parameters such as particle size, material, and surface modification, and found particles that adhered to the Ch–Iso interface or were dispersed in the Iso phase.

## 4.2 Preparation of cholesteric compounds

Three types of LC samples were used in this experiment. For the first type, a N LC, 4-cyano-4'-pentylbiphenyl (produced by LCC Ltd) was mixed with a N LC mixture No. 270032 (produced by LCC Ltd, Table 4.1) at a weight ratio of 2 : 3 to serve as a host N LC, and (*S*)-4-[1-(methylheptyl)oxy]carbonyl-phenyl-4-(hexyloxy)benzoate (produced by DIC Corporation) was added as a chiral dopant at 1.0 wt%. In addition, particles (a gift from Professor Isa Nishiyama) with an average diameter of approximately 1  $\mu\text{m}$  were added as tracers to measure the flow. The phase sequences of this LC sample is Ch–69.8 °C–Ch + Iso–72.2 °C–Iso. The glass substrates were spin-coated with poly(methyl methacrylate) (PMMA, produced by Sigma-Aldrich) after removing impurities by ultrasonic cleaning and UV–ozone treatment, and were pasted with a 10- $\mu\text{m}$ -thick spacers between them to fabricate a cell. The LC samples were sandwiched in the 10  $\mu\text{m}$  gap between the glass substrates. The spin-coated PMMA was intended to reduce friction on the substrates and to be used as an alignment film. This sample is referred to as Sample A.

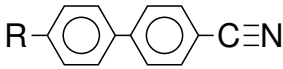
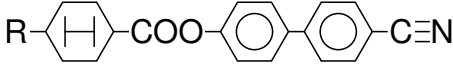

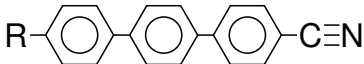
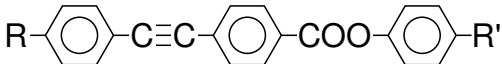
For the second LC sample, 4-cyano-4'-pentylbiphenyl (produced by LCC Ltd) and No. 270032 (produced by LCC Ltd) were mixed at a weight ratio of 3 : 2 to serve as a host N LC, and (*S*)-2-octyl 4-[4-(hexyloxy)benzoyloxy]benzoate (produced by Tokyo Chemical Industry

Co., Ltd) was added as a chiral dopant at 2.8 wt%; the same tracer particles as in Sample A were added. The phase sequences of this LC sample is Ch–49.8 °C–Ch + Iso–56.1 °C–Iso. The cell for sandwiching the sample was prepared by using the same procedure as that for sample A, but the thickness of the gap between the glass substrates for the LC was adjusted to be 20  $\mu\text{m}$ . This is referred to as Sample B.

For both Samples A and B, the helical axis of the uniaxial helical structure of Ch droplets formed in the Ch–Iso coexisting phase is mostly oriented parallel to the substrate due to the effect of the spin-coated PMMA, resulting in stripped droplets. CC droplets are also formed at a certain rate, but it is inefficient to select for observation CC droplets that form by chance. I applied an electric field to the droplets to control the direction of the helical axis, forming only CC droplets. The third LC sample was prepared for this purpose. The host N LC NA-0199 (produced by DIC Corporation) with negative dielectric anisotropy was mixed with 17.1 wt% octadecane (produced by Tokyo Chemical Industry Co., Ltd.) and 1.7 wt% chiral dopant of (*S*)-2-octyl 4-[4-(hexyloxy)benzoyloxy]benzoate (produced by Tokyo Chemical Industry Co., Ltd.). Micro Pearl EX(H) (produced by Sekisui Chemical Co., Ltd.) with an average particle diameter of  $2.50 \pm 0.05 \mu\text{m}$  and the particles used for Samples A and B were added to visualize the flow field. The phase sequences of this LC sample is Ch–33.3 °C–Ch + Iso–73.2 °C–Iso. The temperature range of the Ch–Iso coexisting phase was broadened by adding octadecane as an impurity. Glass substrates coated with a transparent electrode film made of indium tin oxide (ITO) were used for the glass cell sandwiching the LC sample. The substrates with ITO film were cleaned and spin-coated with PMMA in the same manner as Samples A and B; the thickness of the cell was adjusted to 20  $\mu\text{m}$ . This sample is referred to as Sample C. An AC voltage was applied across the substrates with a peak-to-peak voltage of  $V_{\text{pp}} = 20 \text{ V}$  and a frequency of 300 kHz by using a WF 1974 multifunction generator (produced by NF Corporation). Since Sample C has a negative dielectric anisotropy, the director is stable and



Table 4.1: Composition of No. 270032

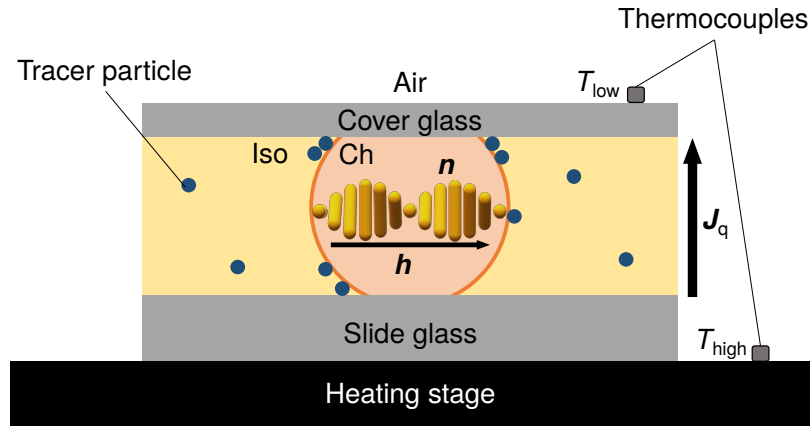
Component	Concentration / wt%
$R$ -  -C≡N	57
$R$ -  -C≡N	15
$R$ -O-  -C≡N	11
$R$ -  -C≡N	10
$R$ -  -R'	7

perpendicular to the applied electric field. Therefore, the helical axis of the Ch droplets is aligned parallel to the electric field and perpendicular to the substrate, forming a CC droplet.

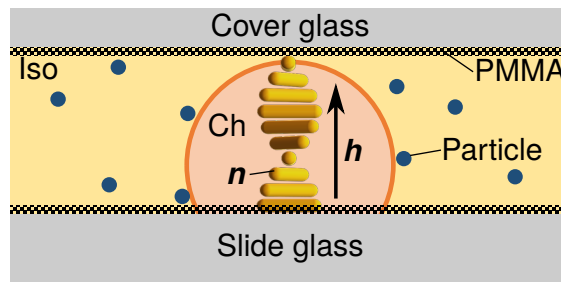
### 4.3 Temperature-control method

The temperature of Sample A was controlled by using a conventional heating stage (produced by Linkam Scientific Instruments), which heated only the lower side of the cell while the upper side of the cell was in contact with ambient air and naturally cooled. Therefore, heat flow was directed from the bottom to the top of the cell. The temperatures at the bottom and top of the cell were measured by using thermocouples (produced by Shimaden Co., Ltd.).

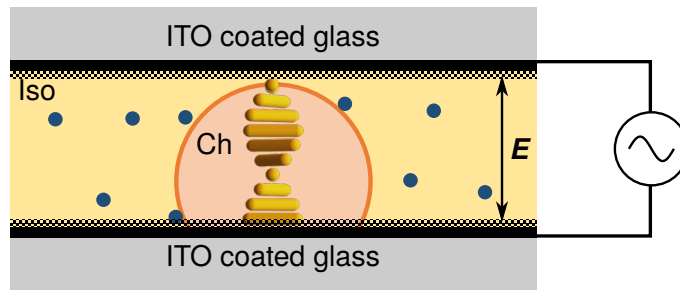
The temperature of Samples B and C was controlled by using a homemade device to apply



(a)



(b)



(c)

Figure 4.1: Schematic figures of Samples (a) A, (b) B, and (c) C. Ch, Iso,  $n$ ,  $h$ ,  $J_q$ , and  $E$  denote cholesteric phase, isotropic phase, the director, the helical axis of the director field, a heat flux, and an electric field, respectively. This figure is reproduced from References [81,83].

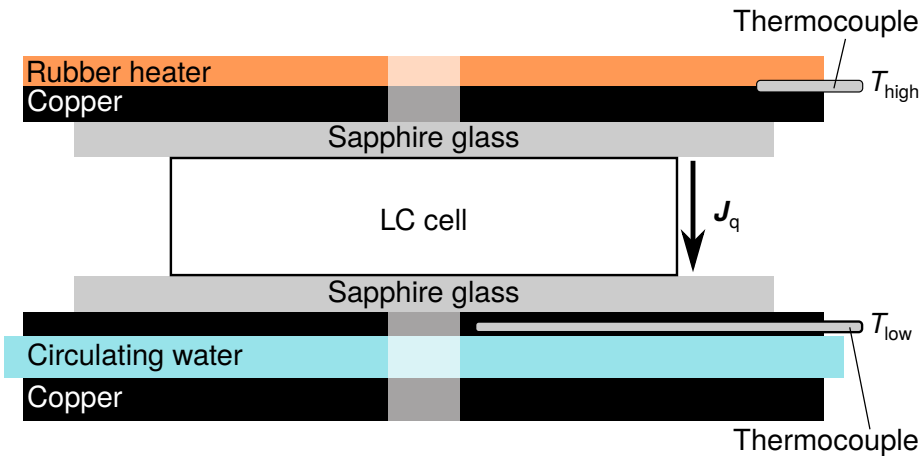


Figure 4.2: A schematic figure of my homemade device to apply a temperature gradient.  $J_q$  denotes a heat flux. This figure is reproduced from Reference [83].

a temperature gradient. This device heated the upper side of the cell via rubber heaters and cooled the lower side of the cell via circulating water, allowing the temperatures of the upper and lower parts of the cell to be controlled independently. The temperature at the top of the cell was measured with a thermocouple attached to a S11A heat flow sensor (produced by Eto Denki), and PID was controlled by using an SR23 digital controller (produced by Shimaden Co., Ltd.). The temperature at the bottom of the cell was measured with a K-type sheath thermocouple (produced by Sakaguchi E.H Voc Corp.) and a SR23 digital controller, and the temperature of the circulating water was controlled with a DC10 chiller combined with a K10 pump (produced by Haake).

## 4.4 Polarizing microscopy

The observation was made by using a BX51 polarizing microscope (produced by Olympus Corporation) equipped with a white-light source. Only the polarizer, which was positioned in the light path between the light source and the specimen, was applied, whereas the analyzer,

which was the second polarizer placed in the optical pathway after the specimen, was not used. The linearly polarized light was normally incident onto the sample and the transmitted light was detected without polarizers. This setup enabled me to observe both the texture of Ch droplets and the tracer particles, which are not optically anisotropic. Microscopy images were taken with a DFK23U445 charge-coupled device camera (produced by The Imaging Source) or a ProgRes charge-coupled device camera (produced by Jenoptik AG).

## **4.5 Results of direct observation of rigid-body rotation by particle tracking method**

First, striped droplets were formed using Sample A, and the flow was visualized by the particles. Figure 4.3 shows an image sequence of a striped droplet coexisting with its Iso phase. The snapshots were taken every 60 s; the scale bar indicates 10  $\mu\text{m}$ . The Iso phase is in the bright field because a polarizer was inserted only on the light-source side of the LC cell and the analyzer was removed. The droplet showed a striped texture and has a helical axis, as shown by the white arrows in the figure, perpendicular to the stripes. The blue dots are the tracer particles adhering to the droplet. Since impurities such as particles are excluded from the highly ordered LC phase, the particles were attached to the interface between the droplet and Iso phase. The adhesion of the particles did not disturb the director field inside the droplet, and the particles did not become a defect as far as observed under the polarizing microscope. The Ch droplets form upon contact with the substrate on the lower temperature side; when the droplets reach a certain size, they also contact the substrate on the higher-temperature side. The striped droplet shown in Figure 4.3 adhered to both the upper and the lower substrates.

The temperature of the top and the bottom sides of the cell were controlled to be  $T_{\text{low}} = 65.9^\circ\text{C}$  and  $T_{\text{high}} = 70.8^\circ\text{C}$ , respectively; the magnitude of the temperature gradient was

$|\nabla T| = 4.2 \text{ mK } \mu\text{m}^{-1}$ . This temperature gradient induced a heat flux from the back of the page toward the front to drive the droplet rotation, which appeared as a unidirectional textural rotation in the clockwise direction. The particles adhering to the droplet revolved about the rotational axis of the droplet in the same direction as the droplet. The revolution of the particles reveals the flow accompanied by droplet rotation, which demonstrates the rigid-body rotation of the droplet. Labelling as  $\theta$  and  $\theta'$  the rotational angles of the helical axis and one of the aggregates of the particle on the droplet from the initial angles, respectively, gives Figure 4.4 from the temporal variations in  $\theta$  and  $\theta'$ . Figure 4.4 shows that the temporal variation in  $\theta$  and  $\theta'$  are the same. The angular velocities of the texture and the particle aggregate were estimated from the slope of the graph, resulting in the same velocity of  $1.0 \times 10^{-2} \text{ rad s}^{-1}$ . The consistency between the angular velocities indicates that the pure rigid-body rotation is driven without rotation of the director. Angular velocities  $\omega_{\text{droplet}}$  and  $\omega_{\text{particle}}$ , which denote the angular velocity of the droplets and the particles adhering to them, respectively, were measured as shown in Figure 4.5 (open squares).  $\omega_{\text{droplet}}$  and  $\omega_{\text{particle}}$  are completely consistent for multiple droplets and particles.

One may claim that the particles are just transported by the anchoring force at the interface, and the textural rotation is the pure director rotation [61]. However, as shown clearly in Figure 4.3, the particle aggregates adhere at multiple position on the droplet, all of which revolve at the same angular velocity. Moreover, the particle aggregates adhere at random positions on the droplet; that is, the orientations of the director touching the particles differ. If the particles were transported by the interaction with the director, they would not adhere at random positions on the droplet but at a position with a given orientation of the director selectively. In addition, assuming the interaction, when the particles happen to adhere at random positions on the droplet interface, the rotational velocities of the particles at multiple positions should depend on the orientation of the director. However, the experiment shows that the particles adhering

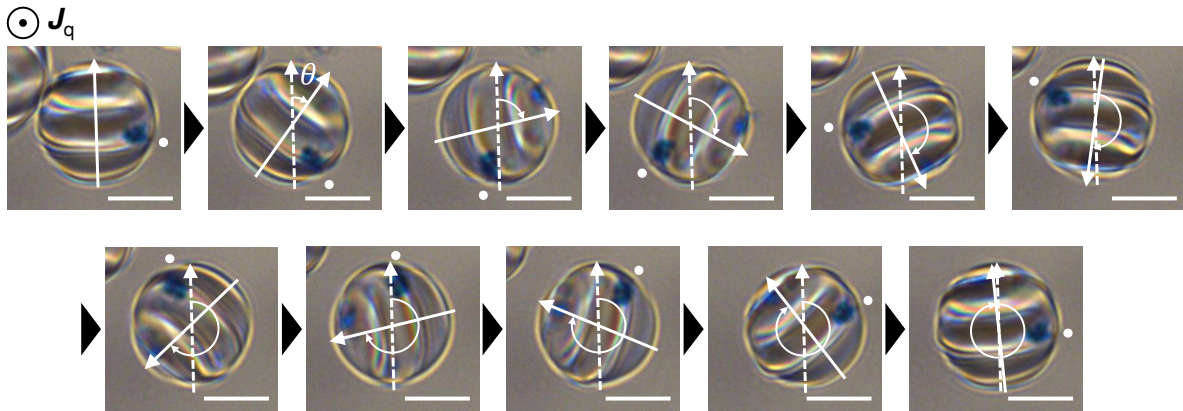


Figure 4.3: Image sequence of a striped droplet coexisting with its isotropic phase and particle aggregates adhering to the droplet. The images were acquired by using a polarizing microscope with linearly polarized incident light. The transmitted light was detected without polarizers. The snapshots were taken every 60 s, and the scale bars indicate  $10\ \mu\text{m}$ . The white solid arrow, the white dashed arrow, the white dot, and  $\mathbf{J}_q$  denote the helical axis, the initial state of the helical axis, the position of a particle aggregate, and the heat flux, respectively. A temperature gradient of  $4.2 \pm 0.2\ \text{mK}\ \mu\text{m}^{-1}$  was applied to the liquid crystal sample by a heating stage. This figure is reproduced from Reference [81].

at multiple positions with different orientations of the director revolve at exactly the same angular velocity as the textural rotation of the droplet, clearly demonstrating pure rigid-body rotation.

Next, I observed the flow accompanied by the Lehmann rotation of CC droplets with Sample B by using the same method. Figure 4.6 shows an image sequence of a CC droplet coexisting with its Iso phase under the polarizing microscope with only one polarizer. The droplet has a concentric-circle texture with its helical axis perpendicular to the page and parallel to the heat flux. The black dot in the CC droplet is a particle adhering to the droplet interface. The adhesion of the particle does not distort the director field, as was the case for the striped droplets. The details of the shape of the droplet, which touches only the colder substrate, are discussed in Section 6.3.

The temperatures of the top and the bottom of the cell were maintained at  $T_{\text{high}} = 56.0\ ^\circ\text{C}$

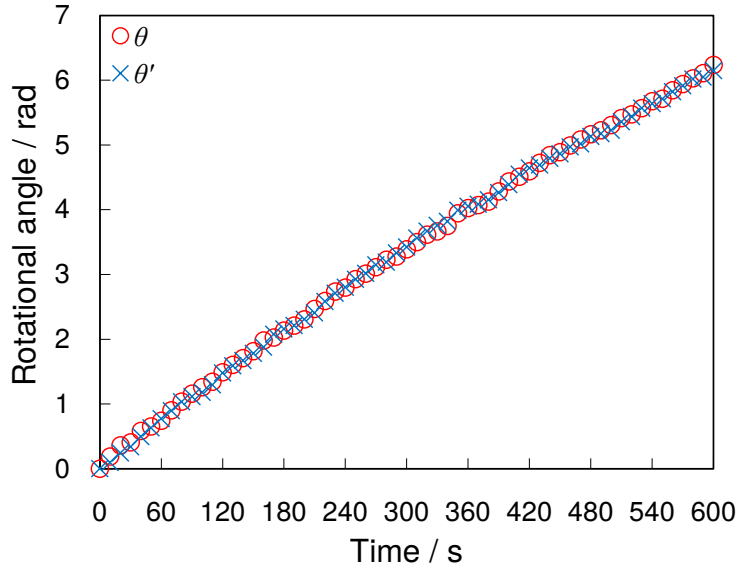


Figure 4.4:  $\theta$  and  $\theta'$  of the droplet and particle aggregate from Figure 4.3 plotted as functions of time.  $\theta$  and  $\theta'$  are the rotational angles of the helical axis and of a particle aggregate on the droplet and are measured from their initial angles. This figure is reproduced from Reference [81].

and  $T_{\text{low}} = 40.0 \text{ }^\circ\text{C}$ , respectively, by using the homemade temperature controller; the magnitude of the temperature gradient was  $|\nabla T| = 13.7 \text{ mK } \mu\text{m}^{-1}$ . The snapshots in Figure 4.6 were taken at 1 s intervals, showing that the concentric-circle texture spreads unidirectionally from the center to the edge of the droplet at a constant speed due to the heat flux oriented into the page. The textural change is attributed to rotation driven by the Lehmann effect. The particle on the CC droplet revolves at the same frequency as the textural rotation and about the central axis of the droplet in the counterclockwise direction and at constant velocity. The direction of the rotation of the particle is consistent with that of the striped droplets. The steady revolution of the particle indicates that a hydrodynamic flow accompanies the rotation of the CC droplet, which constitutes experimental evidence that CC droplets can rotate as rigid bodies. This result thus reveals the rigid-body rotation of Ch LCs with helical axes parallel to the direction of heat flux. I measured the temporal variation in the rotational angle of the

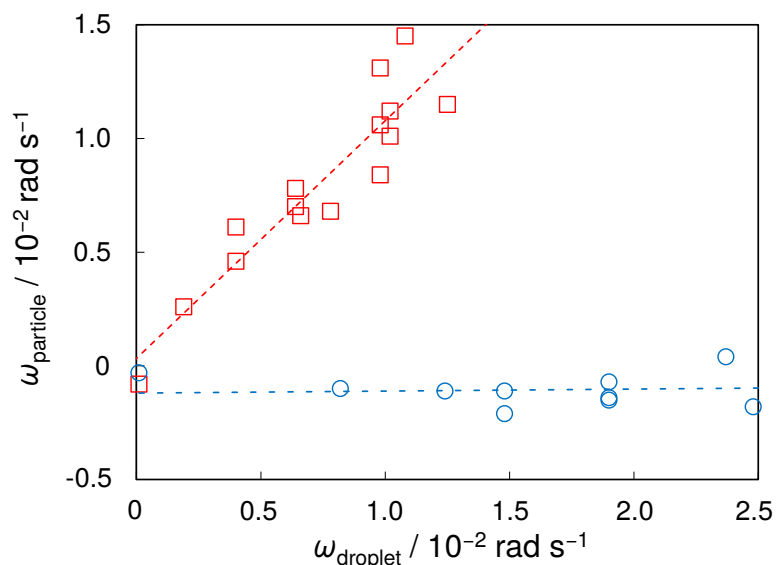


Figure 4.5: Angular velocity  $\omega_{\text{particle}}$  of particle aggregates as a function of the angular velocity  $\omega_{\text{droplet}}$  of the texture of striped droplets. Open squares corresponds to the angular velocities of the texture and the particles adhering to the droplets. The dashed line is a linear fit to the open squares. The open circles correspond to the angular velocities of the texture and the particles in the vicinity of the droplets (see Figure 7.1). The dashed-dotted line is a linear fit to the open circles. The details of the open squares are discussed in Chapter 7. This figure is reproduced from Reference [81].



particle adhering to the droplet from the initial angle (see Figure 4.7), the slope of which gives the angular velocity of the particle as  $\omega_{\text{particle}} = 7.0 \times 10^{-1} \text{ rad s}^{-1}$ . For the textural rotation, since the angular velocity cannot be directly calculated from the temporal variation in the concentric-circle texture. Instead, by rotating the polarizer, I estimated the angular velocity from the textural variation of the CC droplet at rest without applying a temperature gradient. Figure 4.8 shows the temporal change in the light intensity averaged over the small area at the center of the droplet at rest when the polarizer was rotated by  $360^\circ$ . The open circles are the measured values, and the dashed line gives the squared sine of the polarizer angle. The initial phase is taken to have light intensity  $I = 0$  when the polarizer angle  $P = 0$ . This measurement gives the following experimental relationship between the transmitted light intensity  $I$  and the angular velocity  $\omega_{\text{droplet}}$ :

$$I = \sin^2(\omega_{\text{droplet}}t + \delta), \quad (4.1)$$

where  $\delta$  denotes the initial angle. By fitting the result shown in Figure 4.9, in which the temporal variation in light intensity averaged over the small area at the center of the droplet rotating due to a heat flux (by Equation 4.1 with parameters  $\omega$  and  $\delta$ ), the angular velocity of the CC droplet is estimated to be  $\omega_{\text{droplet}} = 6.7 \times 10^{-1} \text{ rad s}^{-1}$ . The angular velocities of the particle and the droplet are the same,  $\omega_{\text{droplet}} = \omega_{\text{particle}}$ , indicating that the CC droplet and the striped droplet both undergo pure rigid-body rotation.

## 4.6 Rigid-body rotation of an aggregate composed of cholesteric droplets and particles

The previous section presents a novel method where the flow is visualized via particles that adhere to the Ch droplets, proving that the droplets undergo rigid-body rotation driven by

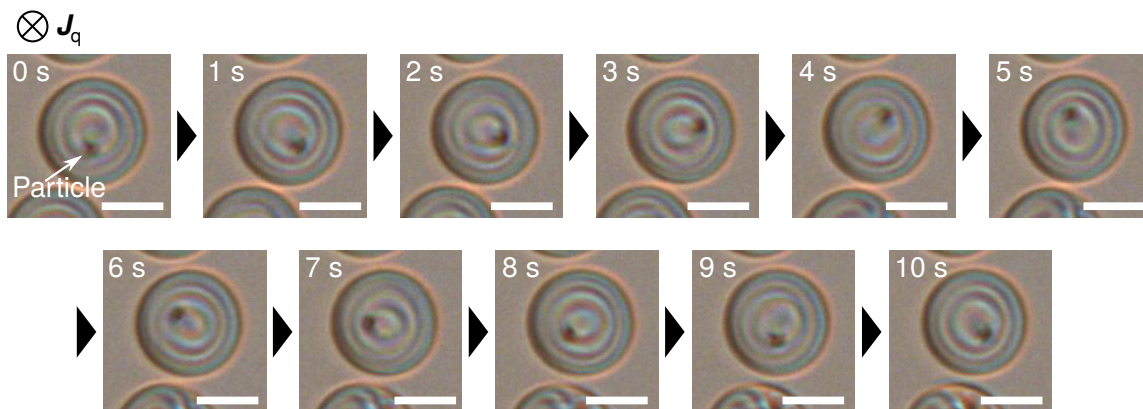


Figure 4.6: An image sequence of a concentric-circle droplet coexisting with its isotropic phase and of particle aggregates adhering to the droplet. The image was acquired by using a polarizing microscope with linearly polarized incident light. The transmitted light was detected without polarizers. The snapshots were taken at 1 s intervals. The scale bars and  $\mathbf{J}_q$  indicate 10  $\mu\text{m}$  and the heat flux, respectively. The temperature at the top and bottom of the cell were  $T_{\text{high}} = 56.0\text{ }^\circ\text{C}$  and  $T_{\text{low}} = 40.0\text{ }^\circ\text{C}$ , respectively, so the applied temperature gradient was  $13.7\text{ mK } \mu\text{m}^{-1}$ . The temperature was controlled by using the homemade device shown in Figure 4.2. A temperature gradient of  $4.2 \pm 0.2\text{ mK } \mu\text{m}^{-1}$  was applied to the liquid crystal sample by a heating stage. This figure is reproduced from Reference [83].

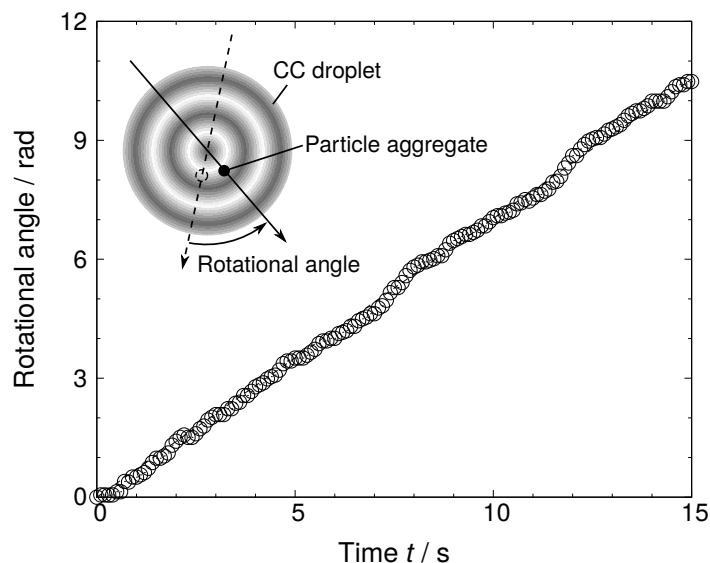


Figure 4.7: Temporal variation in the rotational angle of the particle aggregate on the droplet shown in Figure 4.6. This figure is reproduced from Reference [83].

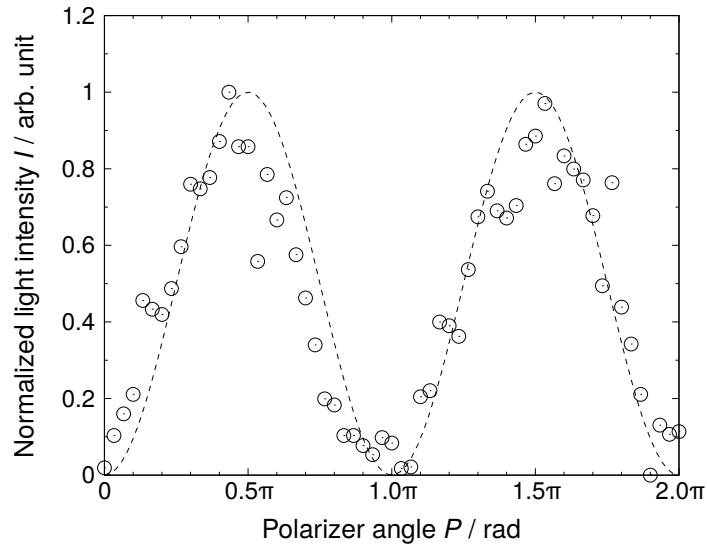


Figure 4.8: Temporal variation in the transmitted light intensity  $I$  of a concentric-circle droplet when the polarizer between the light source and the sample was rotated without the temperature gradient. The transmitted light was observed without polarizers. The droplet was at rest during the rotation of the polarizer. The dashed line indicates  $I = \sin^2(P)$ . This figure is reproduced from Reference [83].

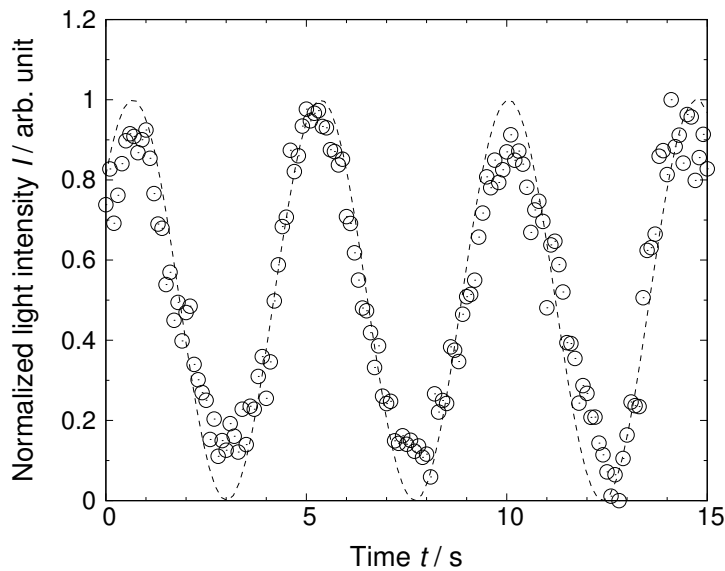


Figure 4.9: Temporal variation in the transmitted light intensity  $I$  at the center of the droplet shown in Figure 4.6. The dashed line is the best-fit curve obtained using Equation 4.1 with fitting parameters  $\omega$  and  $\delta$ . This figure is reproduced from Reference [83].

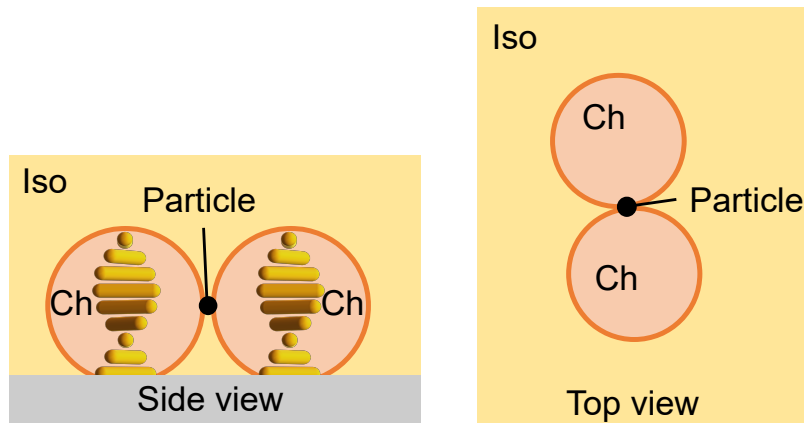


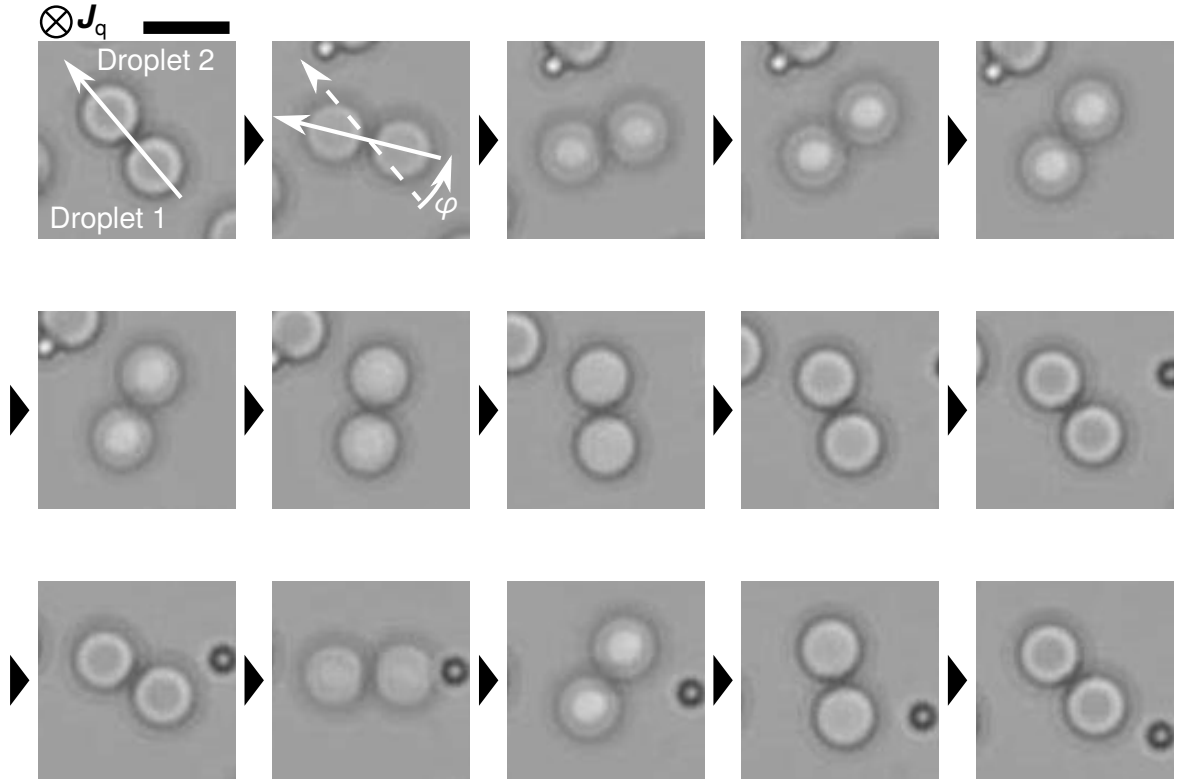
Figure 4.10: Schematic diagram of dumbbell-shaped aggregate composed of two concentric-circle droplets and a particle aggregate. Iso, Ch, and the yellow bars indicate the isotropic phase, cholesteric phase, and the director, respectively.

the Lehmann effect. This section presents another experimental proof of rigid-body rotation driven by the Lehmann effect. The experiment benefits from a novel geometry using particles and provides a new perspective that differs from the flow measurements. Specifically, I formed dumbbell-shaped composites with two CC droplets and a particles aggregate in between, as shown in Figure 4.10. The rigid-body rotation of the composite is driven by the Lehmann effect.

Sample C was used for this experiment, and the temperatures of the top and the bottom of the sample were controlled independently by the homemade device shown in Figure 4.2. Cooling from the temperature at which the sample assumes the Iso phase, Ch droplets were formed in Iso phase and moved due to thermal fluctuation. When two droplets touched each other by chance, the droplets coalesced and underwent interior reorientation to become a large droplet with a uniaxial helical structure. However, if a particle happens to adhere to the position where the droplets touch each other, the droplets are prevented from coalescing to form a dumbbell-shaped composite. The composites form randomly about once every hundred trials. Figures 4.11 and 4.12 show dumbbell-shaped composites formed in their

own Iso phase, as imaged by a polarizing microscope with snapshots taken every 10 and 5 s, respectively. In Figure 4.11, the temperatures of the top and the bottom of the cell were set at  $T_{\text{high}} = 76.0\text{ }^{\circ}\text{C}$  and  $T_{\text{low}} = 40.5\text{ }^{\circ}\text{C}$ , respectively, and the magnitude of the temperature gradient was  $|\nabla T| = 16.0\text{ mK } \mu\text{m}^{-1}$ . In Figure 4.12, the temperatures of the top and the bottom of the cell were set to  $T_{\text{high}} = 94.9\text{ }^{\circ}\text{C}$  and  $T_{\text{low}} = 46.8\text{ }^{\circ}\text{C}$ , respectively, forming a temperature gradient of  $|\nabla T| = 21.7\text{ mK } \mu\text{m}^{-1}$  across the LC. A heat flux directed from the front to the back side of the page caused the Lehmann effect, driving unidirectional counterclockwise rotation of both composites without losing their shape or orientational structure. The center of mass of each droplet composing the composite revolved about the center axis of the rotating composite, which cannot be explained based on pure director rotation. This result is a clear indication of rigid-body rotation of the composites.

To quantitatively analyze the rotation of the composite shown in Figure 4.11, I measured the temporal variations in the average light intensity at the center of each droplet composing the aggregate and in the rotational angle of the whole composite, which produces Figure 4.13. Open squares and open triangles show the measured light intensity  $I$  of Droplets 1 and 2, respectively, shown in Figure 4.11. Both plots correspond to the right vertical axis. Open circles show the measured rotational angle of the composite  $\varphi$  and correspond to the left vertical axis. To compare the light intensity and the rotational angle, I converted the rotational angle to light intensity by using Equation 4.1, obtaining the solid line shown in Figure 4.11. The temporal variations in the light intensities measured experimentally are consistent with those estimated from the rotational angle of the composite, which is indicative of pure rigid-body rotation without director rotation. In this novel geometry, the results thus demonstrate rigid-body rotation of Ch droplets driven by a heat flux not by measuring flow field but by revolving droplets with particles about the center axis of the rotation.



(Taken every 10 s)

Figure 4.11: Image sequence of a dumbbell-shaped aggregate composed of two concentric-circle droplets and a particle aggregate. The image was acquired by using a polarizing microscope with linearly polarized incident light, and the transmitted light was detected without polarizers. Two concentric-circle droplets, referred to as Droplet 1 and Droplet 2, were connected by a particle aggregate. The snapshots were taken every 10 s, and the scale bar indicates 20  $\mu\text{m}$ . The temperatures of the top and the bottom of the cell were set to  $T_{\text{high}} = 76.0^\circ\text{C}$  and  $T_{\text{low}} = 40.5^\circ\text{C}$ , respectively, by using the homemade device shown in Figure 4.2. The magnitude of the temperature gradient was  $|\nabla T| = 16.0 \text{ mK } \mu\text{m}^{-1}$ . The solid arrow, dashed arrow, and  $\mathbf{J}_q$  indicate the angle of the composite, the initial angle of the composite, and the heat flux, respectively.  $\varphi$  denotes the angle between the solid and the dashed arrows. This figure is reproduced from Reference [83].

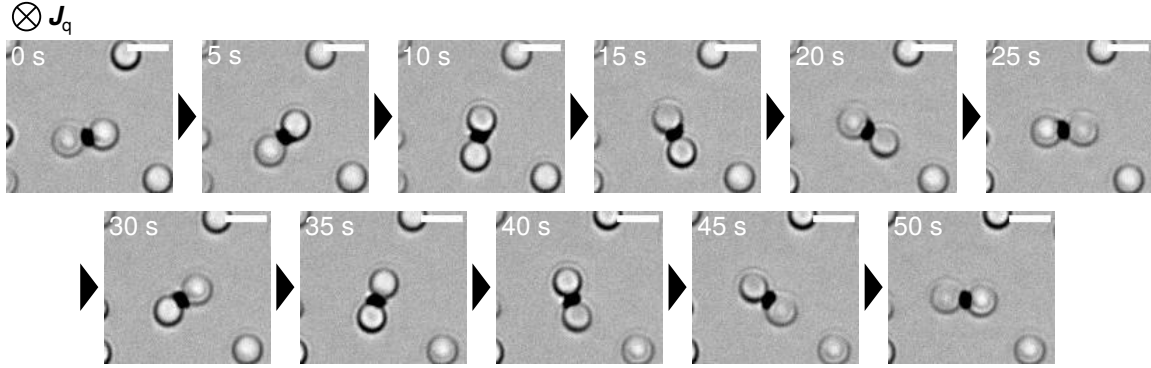


Figure 4.12: Image sequence of a dumbbell-shaped aggregate composed of two concentric-circle droplets and a particle aggregate. The image was acquired by using a polarizing microscope with linearly polarized incident light. The transmitted light was detected without polarizers. The snapshots were taken every 5 s, and the scale bar indicates 10  $\mu\text{m}$ . The temperatures of the top and the bottom of the cell were set to  $T_{\text{high}} = 94.9^\circ\text{C}$  and  $T_{\text{low}} = 46.8^\circ\text{C}$ , respectively, by using the homemade device shown in Figure 4.2. The magnitude of the temperature gradient was  $|\nabla T| = 21.7 \text{ mK } \mu\text{m}^{-1}$ . This figure is reproduced from Reference [83].

## 4.7 Dependence of angular velocity on droplet radius

When the Lehmann effect drives pure director rotation of Ch droplets, the angular velocity is constant with respect to droplet size, as given by Equation 3.19. This is because the Lehmann torque and the rotational viscosity both act on a unit volume and balance each other. Although the angular velocity is constant with respect to droplet size for director rotation, the velocity should depend on size in the experimental system used to demonstrate rigid-body rotation of droplets. In the Ch–Iso coexisting phase, the size of the Ch droplets can be tuned by adjusting the temperature. As the temperature increases, the droplets become smaller as the LC approaches the Iso phase. As the temperature decreases, the droplets become larger as the LC approaches the Ch phase. If the magnitude of the temperature gradient also changes as the temperature varies, the torque to drive the rotation changes. Since the angular velocity of rotation is affected by the temperature gradient, only the average temperature need be changed

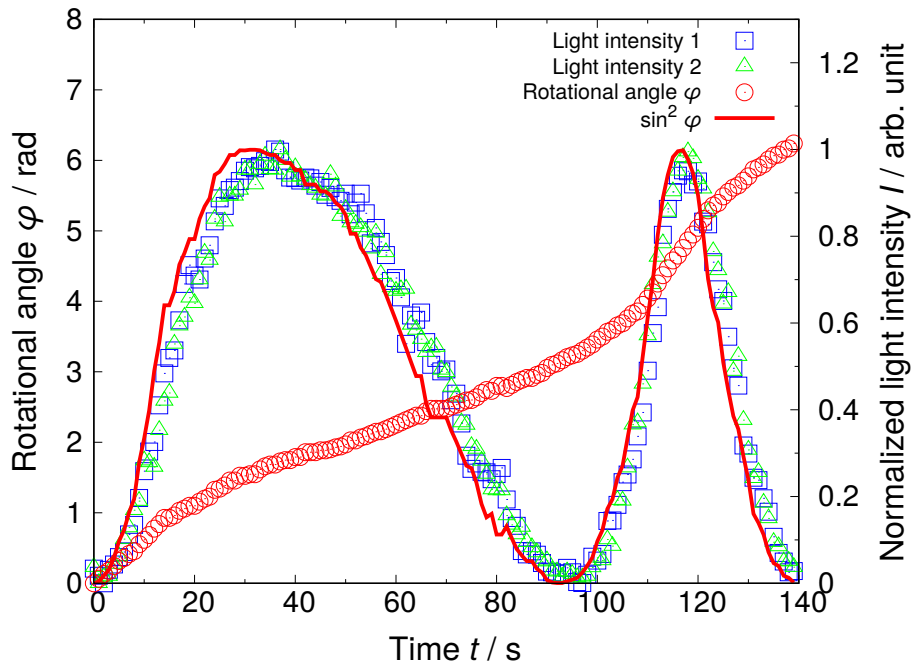


Figure 4.13: Temporal variation in rotational angle  $\varphi$  of the composite and in the light intensities transmitted at the center of each droplet shown in Figure 4.11. The open squares and the open triangles give the temporal variation of the transmitted light intensity for Droplets 1 and 2, respectively, and correspond to the right vertical axis. The open circles give the temporal change in  $\varphi$ , and correspond to the left vertical axis. This figure is reproduced from Reference [83].



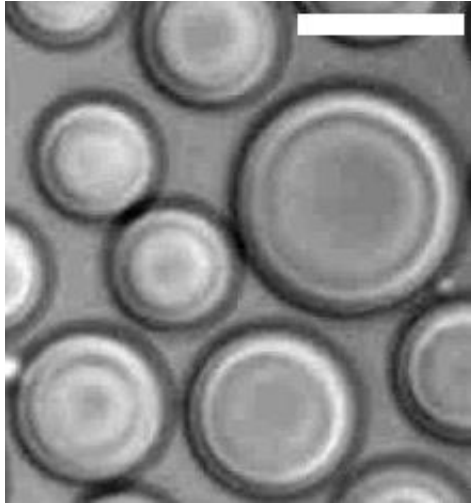


Figure 4.14: Polarizing microscopy image of concentric-circle droplets under a temperature gradient of  $|\nabla T| = 14.8 \text{ mK } \mu\text{m}^{-1}$ . A linearly polarized light was incident, and the transmitted light was detected without polarizers. The scale bar indicates  $20 \mu\text{m}$ .

to maintain the magnitude of the temperature gradient so that the dependence of the angular velocity on droplet size can be analyzed. As shown in Figure 4.14, Ch droplets formed in the cooling process from the Iso phase are not necessarily the same size, so that the angular velocity can be measured simultaneously for a certain range of droplet radii without changing the average temperature.

Figure 4.15 shows how angular velocity depends on droplet size when a temperature gradient of  $|\nabla T| = 14.8 \text{ mK } \mu\text{m}^{-1}$  is applied to Sample C. The graph shows log-log plots with the droplet radius plotted on the horizontal axis and the angular velocity on the vertical axis. Open circles show the experimental results; the larger the radius, the slower the angular velocity of rotation. This dependence is consistent with the flow measurements that show that the rigid-body rotation of the droplets is driven by the Lehmann effect. Since the plots are linearly aligned with slope of  $-1$ , the angular velocity  $\omega$  should be inversely proportional to the drop radius  $R$ . A detailed discussion of this dependence will be given in Chapter 6.

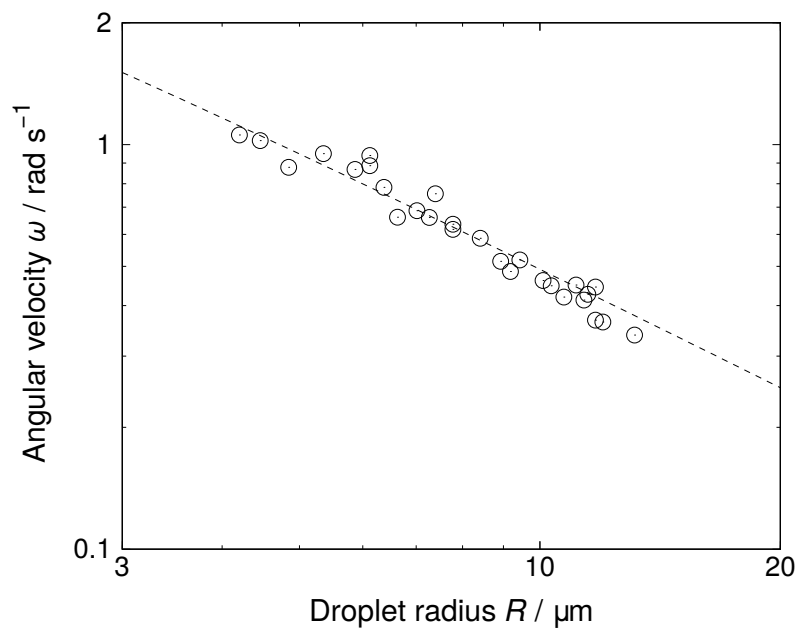


Figure 4.15: Log–log plot of the angular velocity of concentric-circle droplets  $\omega$  as a function of droplet radii  $R$ . Sample B was used for the measurements, and a temperature gradient of  $|\nabla T| = 14.8 \text{ mK } \mu\text{m}^{-1}$  was applied. Open circles show the experimental results, and the dashed line is the best-fit using Equation 6.16. The details of the fit are given in Chapter 6. This figure is reproduced from Reference [83].

# Chapter 5

## Measurement of Coupling Constant $\nu$ between Heat Flux and Torque

### 5.1 Purpose

The purpose of the experiments reported in this chapter is to measure the magnitude of the coupling constant  $\nu$  between the heat flux and torque and that appears in the Equation 3.18 to quantitatively investigate the rigid-body rotation of Ch droplets driven by the Lehmann effect. By simultaneously applying an electric field and a temperature gradient to Ch droplets coexisting with their Iso phase, the coupling constant  $\nu$  is determined from the condition of static equilibrium. The coupling constant  $\nu$  may also be determined by measuring the rotational velocity in a dynamic rigid-body rotation. In this case,  $\nu$  is determined from the balance between the torque induced by the Lehmann effect and the viscous torque on the interfaces. However, since measuring the viscous torque directly is difficult, the coupling constant is estimated by assuming viscous torque. On the other hand, when the coupling constant is determined from static equilibrium, no dynamic parameter such as viscous torque

is involved, which means that  $\nu$  can be obtained directly from the equilibrium between the torque induced by the Lehmann effect and that induced by the electric field.

## 5.2 Methods

The LC sample for this experiment was composed of E7 (produced by LCC Ltd.), a host N LC, and 1.0 wt% (*S*)-2-octyl 4-[4-(hexyloxy)benzoyloxy]benzoate (produced by Tokyo Chemical Industry Co., Ltd.) added as a chiral dopant. E7 is a mixed LC sample with the composition given in Table 5.1 and has a large positive dielectric anisotropy of  $\Delta\epsilon \simeq 10$ . Therefore, the director is oriented parallel to the applied electric field even for a weak electric field. Figure 5.1 shows the LC cell for this experiment. Two glass substrates were prepared and spin-coated with PMMA after removing surface impurities by ultrasonic cleaning and UV–ozone treatment. The substrates were pasted, sandwiching two 30- $\mu\text{m}$ -thick sheets of stainless steel film, with the LC sample sealed in the gap between the substrates. The two stainless steel films were about 300  $\mu\text{m}$  apart and also serve as electrodes to apply an electric field perpendicular to the temperature gradient. The stainless steel electrodes were connected to a WF 1974 multi-function generator (produced by NF Corporation); a 10 kHz AC voltage with a peak-to-peak amplitude  $V_{\text{pp}} = 0\text{--}17$  V was applied parallel to the substrate. The cell was installed in the homemade temperature controller shown in Figure 4.2. The upper and lower substrates were independently heated and cooled, respectively, to generate a heat flow perpendicular to the substrate. Observations were made by using a BX51 polarizing microscope (produced by Olympus Corporation) with crossed polarizers, and the images were acquired with a DMK23U445 charge-coupled device (produced by The Imaging Source).

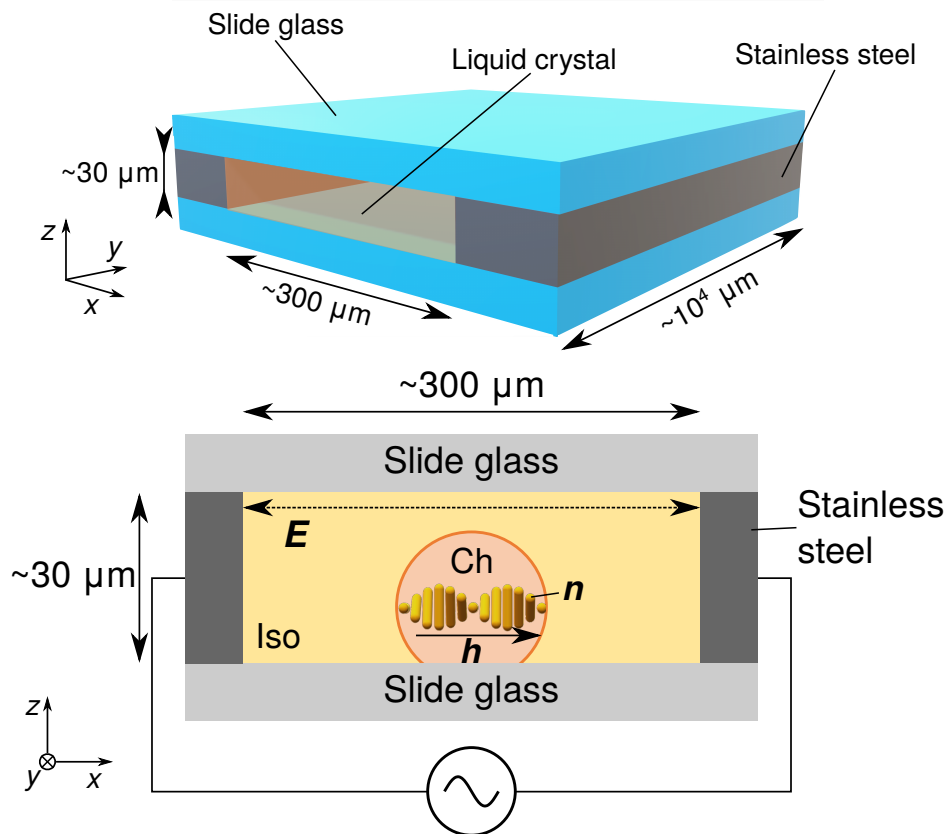
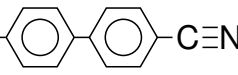
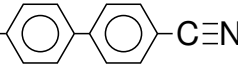
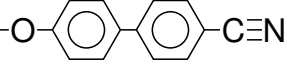
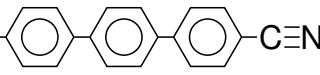


Figure 5.1: Schematic illustration of liquid crystal cell with stainless-steel electrodes to measure the coupling constant. A transverse AC electric field is applied across the sample. Iso, Ch,  $n$ ,  $h$ , and  $E$  denote isotropic phase, cholesteric phase, the director, the helical axis of the director field, and the electric field, respectively. This figure is reproduced from Reference [83].

Table 5.1: Composition of E7

Component	Concentration / wt%
$C_5H_{11}$ - 	51
$C_7H_{15}$ - 	25
$C_8H_{17}$ -O- 	16
$C_5H_{11}$ - 	8

### 5.3 Deriving $\nu$ from balance between Lehmann torque and electric-field-induced torque

This experiment determines the magnitude of the electric field and that of the temperature gradient, where Ch droplets are at rest. The dielectric anisotropy of E7 is already known. In this section, the coupling constant  $\nu$  between heat flux and torque is derived from these properties.

Leslie's phenomenological theory [29, 84] gives the expression of the torque  $\tau^{\text{Leh}}$  exerted on the director  $\mathbf{n}$  of Ch LCs per unit volume under a temperature gradient  $\nabla T$  (Equation 3.18);  $\tau^{\text{Leh}} = \nu \mathbf{n} \times \mathbf{n} \times (-\nabla T)$ . A simple way to measure the magnitude of  $\nu$  experimentally is to apply to Ch droplets an electric field  $\mathbf{E}$  perpendicular to a temperature gradient [69, 70]. Equation 2.19 yields the torque  $\tau^{\text{el}}$  exerted on the director per unit volume under an electric

field  $\mathbf{E}$  as

$$\boldsymbol{\tau}^{\text{el}} = \varepsilon_0 \Delta \varepsilon (\mathbf{n} \times \mathbf{E}) \mathbf{n} \cdot \mathbf{E}. \quad (5.1)$$

When the magnitude of the torque induced by the Lehmann effect and that by the electric field are insufficient to distort the director field, the Lehmann rotation of the droplets stops under the balance between  $\boldsymbol{\tau}^{\text{Leh}}$  and  $\boldsymbol{\tau}^{\text{el}}$ . This condition holds in this experiment. I set up the coordinate system shown in Figure 5.1 to calculate the torque. The origin is at the center of the LC sample, and the  $z$  axis is perpendicular to the substrates. The  $x$  and  $y$  axes are parallel and perpendicular to the longitudinal direction of the electrodes, respectively. The temperature gradient is

$$\nabla T = (0, 0, \nabla T_z). \quad (5.2)$$

The electric field can be approximated as

$$\mathbf{E} = (E_x, 0, 0). \quad (5.3)$$

The director field is set to

$$\mathbf{n} = (\sin \Theta \cos \Phi, \sin \Theta \sin \Phi, \cos \Theta), \quad (5.4)$$

with the zenithal angle  $\Theta$  and the azimuthal angle  $\Phi$ , the  $z$  component of each torque is

$$\tau_z^{\text{Leh}} = \nu \sin^2 \Theta (-\nabla T_z), \quad (5.5)$$

$$\tau_z^{\text{el}} = -\frac{1}{2} \varepsilon_0 \Delta \varepsilon \sin^2 \Theta \sin 2\Phi E_x^2. \quad (5.6)$$

The  $z$  component of the total torque acting on Ch droplets per unit volume is given by the

sum of these torques:

$$\tau_z^{\text{tot}} = \sin^2 \Theta(-\nabla T_z) \left( \nu - \frac{\varepsilon_0 \Delta \varepsilon}{2(-\nabla T_z)} \sin 2\Phi E_x^2 \right). \quad (5.7)$$

$\tau_z^{\text{tot}} = 0$  is satisfied when these torques are balanced to stop the rotation of the droplets. Under this condition, the coupling constant  $\nu$  is

$$\nu = \frac{\varepsilon_0 \Delta \varepsilon}{2(-\nabla T_z)} \sin 2\Phi E_x^2 \quad (5.8)$$

if the magnitude of the temperature gradient  $\nabla T_z$  and that of the electric field  $E_z$  are known.

In my experience, a spatially uniform temperature gradient  $\nabla T_z$  can be realized by controlling the top and the bottom of the cell directly and independently. In contrast, when a voltage  $V_0$  is applied across the electrodes, the electric field  $E_z$  is not spatially uniform, so the specific form of  $E_z$  must be derived. <sup>1</sup> To do this, I simplify the actual experimental setup shown in Figure 5.1 to the system shown in Figure 5.2. Since the electrodes are so thin and long in the  $z$  and  $y$  directions, respectively, they can be approximated as two parallel conductive wires of radius  $a \simeq 15 \mu\text{m}$  and of length  $l \simeq 10 \text{mm}$  installed  $d \simeq 300 \mu\text{m}$  apart from each other in a medium with dielectric constant  $\varepsilon$ . The condition  $a \ll d \ll l$  allows the image charges in the wires to be neglected; the wires can be considered to have the infinite length. Given these assumptions, when an electric potential difference  $V_0$  is applied across the conductive wires,

---

<sup>1</sup>In a previous study, Oswald measured the coupling constant  $\nu$  by using the same method as used herein [69]. This previous report, however, did not consider the spatial dependence of the electric field, so its analysis was imperfect and leaves a possibility of an inaccurate measurement of  $\nu$ . In my experiment, I consider the spatial dependence of the electric field and calculate the accurate value of  $\nu$  from the experimental results.



the electric field at a point on the  $xy$  plane can be expressed as

$$\mathbf{E}(x, y, z = 0) = -\frac{\rho}{2\pi\epsilon} \left( \frac{1}{\frac{d}{2} + x} + \frac{1}{\frac{d}{2} - x} \right) \mathbf{e}_x, \quad (5.9)$$

where  $\pm\rho$  and  $\mathbf{e}_x$  are the charge per unit length in the wires and the standard unit vector in the  $x$  direction, respectively. Since the electric potential difference is  $V_0$ , Equation 5.9 yields

$$\begin{aligned} V_0 &= -\frac{\rho}{2\pi\epsilon} \int_{-\frac{d}{2}+a}^{\frac{d}{2}-a} \left( \frac{1}{\frac{d}{2} + x} + \frac{1}{\frac{d}{2} - x} \right) dx \\ &= -\frac{2\rho}{2\pi\epsilon} [\ln(d - a) - \ln a] \\ &\simeq -\frac{2\rho}{2\pi\epsilon} \ln\left(\frac{d}{a}\right). \end{aligned} \quad (5.10)$$

Thus, the general expression of the electric field is

$$\mathbf{E}(x, y, z) = -\frac{V_0}{2 \ln\left(\frac{d}{a}\right)} \left( \frac{\frac{d}{2} + x}{\left(\frac{d}{2} + x\right)^2 + z^2} + \frac{\frac{d}{2} - x}{\left(\frac{d}{2} - x\right)^2 + z^2}, 0, \frac{z}{\left(\frac{d}{2} + x\right)^2 + z^2} - \frac{z}{\left(\frac{d}{2} - x\right)^2 + z^2} \right). \quad (5.11)$$

The electric field applied to the Ch droplets is

$$E_x(x, y = 0, z = 0) \simeq -\frac{V_0}{2 \ln\left(\frac{d}{a}\right)} \left( \frac{1}{\frac{d}{2} + x} + \frac{1}{\frac{d}{2} - x} \right), \quad (5.12)$$

$$E_y(x, y = 0, z = 0) \simeq 0, \quad (5.13)$$

$$E_z(x, y = 0, z = 0) \simeq 0, \quad (5.14)$$

because the droplets approximately form on the  $x$  axis. The magnitude of the electric field increases at a position closer to the electrodes and diverges to infinity on the electrodes. Substituting Equation 5.12 into Equation 5.7, the total torque on the droplets is

$$\tau_z^{\text{tot}} = \sin^2 \Theta (-\nabla T_z) \left\{ \nu - \frac{\varepsilon_0 \Delta \varepsilon}{2(-\nabla T_z)} \sin 2\Phi \left[ \frac{V_0}{2 \ln \left( \frac{d}{a} \right)} \left( \frac{1}{\frac{d}{2} + x} + \frac{1}{\frac{d}{2} - x} \right) \right]^2 \right\}. \quad (5.15)$$

Equation 5.15 indicates that the rotational behavior of the Ch droplets under a constant temperature gradient  $\nabla T_z$  depends on both the electric potential difference  $V_0$  between the electrodes and the  $x$  position of the droplet. When  $V_0$  is sufficiently small, the droplets keep rotating, except those at the electrodes ( $x = \pm d/2$ ). Increasing  $V_0$  gradually, the region in which the droplets stop rotating is extended to

$$\begin{cases} -\frac{d}{2} \leq x \leq -x^{\text{th}}, \\ x^{\text{th}} \leq x \leq \frac{d}{2}, \end{cases} \quad (5.16)$$

where  $x^{\text{th}}$  is the position at which  $\tau_z^{\text{tot}} = 0$ , that is to say,

$$\nu = \frac{\varepsilon_0 \Delta \varepsilon}{2(-\nabla T_z)} \left[ \frac{V_0}{2 \ln \left( \frac{d}{a} \right)} \left( \frac{1}{\frac{d}{2} + x^{\text{th}}} + \frac{1}{\frac{d}{2} - x^{\text{th}}} \right) \right]^2 \quad (5.17)$$

is satisfied. Therefore,  $x^{\text{th}}$  gives the boundary between the regions in which the droplets rotate and do not rotate. Experimentally, the coupling constant  $\nu$  can be determined by measuring  $x^{\text{th}}$  under various electric potential differences  $V_0$  while maintaining a constant temperature gradient  $|\nabla T|$  and then by substituting the values into Equation 5.17.

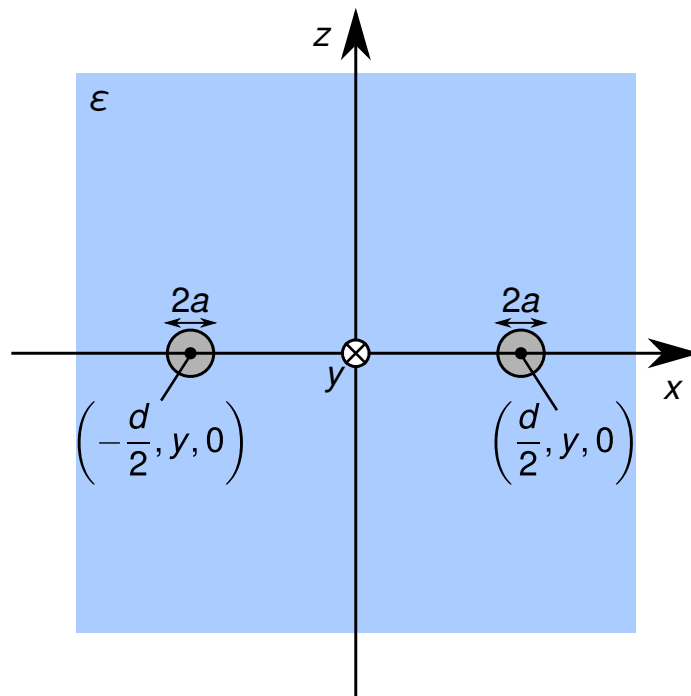


Figure 5.2: Schematic diagram of the coordinate system to calculate the electric field. Two conductive wires with radius  $a \approx 15 \mu\text{m}$  and length  $l \approx 10 \text{ mm}$  are set in a homogeneous media with dielectric constant  $\varepsilon$  and separated by a distance  $d \approx 300 \mu\text{m}$ . The  $x$  axis passes through the centers of the wires, and the  $y$  axis is parallel to the wires. This figure is reproduced from Reference [83].

## 5.4 Results and comparison to previous studies

Figure 5.3 shows Ch droplets dispersed in their own Iso phase under a polarizing microscope with crossed polarizers. Striped droplets characterized by the striped texture were formed, and the dark region surrounding the droplets corresponds to the Iso phase. The dark field due to the electrode is to the right of the observed region. The temperature gradient was applied in the direction perpendicular to the page (from the front to the back), and the AC electric field was applied in the crosswise direction of the page. The torque induced by the heat flux rotates the droplets in the counterclockwise direction. However, since the LC sample for this experiment has a positive dielectric anisotropy, the helical axis of the droplets are oriented perpendicular to the electric field in the vicinity of the electrodes. At the position of  $x = x^{\text{th}}$ , the droplets are at rest with an angle of  $45^\circ$  between their helical axes and the electric field because the torque induced by the electric field has the maximum value with  $\Phi = \pi/4$  in Equation 5.6. In my experiment, the magnitude of torque induced by the heat flux and that by the electric field was smaller than the orientational elasticity, so the director field was not distorted, as one can see from the texture. Since no orientational distortion occurred, the coupling constant  $\nu$  can be directly calculated by substituting the experimental conditions and measured values into Equation 5.17 from the previous section.

In the polarizing microscopy image of Figure 5.3, an AC voltage with an effective amplitude of  $V_0 = 7.5 \text{ V}$  was applied in the  $x$  direction, and a temperature gradient of  $4.3 \text{ mK } \mu\text{m}^{-1}$  was applied in the  $z$  direction. The graph in Figure 5.3 shows the magnitude of the applied electric field calculated from Equation 5.12. Here the boundary between the regions in which the droplets rotate and do not rotate was at  $x^{\text{th}} \simeq 45 \text{ } \mu\text{m}$ , where the magnitude of the electric field was  $E_x(x = x^{\text{th}}, y = 0, z = 0) \simeq 17 \text{ V mm}^{-1}$ . Substituting these values into Equation 5.17, the coupling constant is calculated to be  $\nu \simeq 3 \times 10^{-6} \text{ kg K}^{-1} \text{ s}^{-2}$ . The same measure-

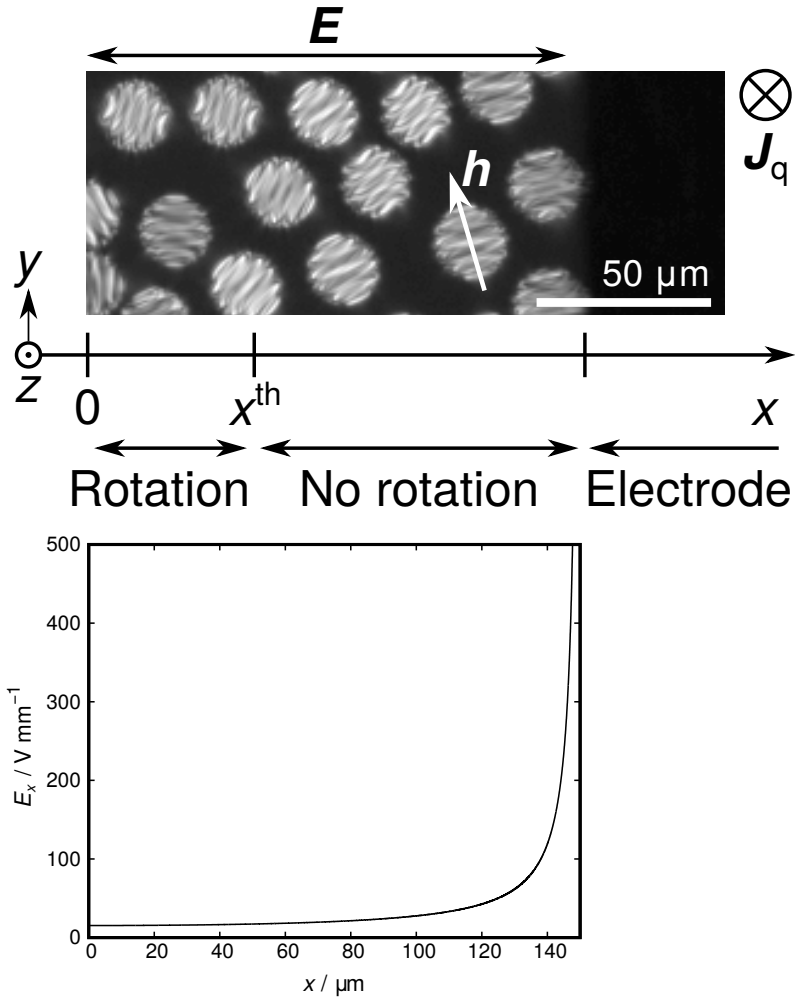


Figure 5.3: The upper image shows striped droplets coexisting with their isotropic phase under a polarizing microscope with crossed polarizers. A temperature gradient of  $4.3 \text{ K mm}^{-1}$  was applied in the  $z$  direction, and an AC voltage with a peak-to-peak amplitude of  $V_{pp} = 15 \text{ V}$  and a frequency of  $10 \text{ kHz}$  was applied in the  $x$  direction.  $h$ ,  $E$ ,  $J_q$ , and  $x^{\text{th}}$  denote the helical axis of the director field, the electric field, the heat flux, and the threshold position, respectively.  $x^{\text{th}}$  gives the boundary between the regions in which the droplets rotate and do not rotate. The lower graph shows the magnitude of the electric field  $E_x$  calculated using Equation 5.12. This figure is reproduced from Reference [83].

ment and analysis were conducted after changing the AC voltage from  $V_0 = 2.5$  V to  $V_0 = 8.5$  V in steps of 0.5 V, resulting in the same values of  $\nu$ .

Let us compare the value of the coupling constant with that obtained in the previous studies. First I compare it with the work of Éber and Jánossy (1982), where they measured the coupling constant by balancing the Lehmann torque and the orientational elasticity in a bulk Ch LC [62]. They used compensated Ch, of which the pitch of the helical structure (i.e., the strength of macroscopic chirality) depends on temperature; the helical structure vanishes at the compensation temperature and its chirality inverts continuously across the compensation temperature. In their study, the measurement of the coupling constant was conducted at the compensation temperature, and they estimated the upper limit of the constant to be  $|\nu| < 2 \times 10^{-6} \text{ kg K}^{-1} \text{ s}^{-2}$ . Since the helical structure vanishes at the compensation temperature, this value should only reflect the contribution of microscopic interactions between the heat flux and the molecules. In contrast, only diluted Ch LCs, which are obtained by adding a small amount of chiral dopant to a typical N LC, are used in my experiments. Note that the values of the coupling constant for different LC materials with different chirality strengths cannot be directly compared because the coupling constant is expected to depend on the details of the material, especially the chirality strength. However, the value obtained from my experiment is consistent with the upper limit obtained in this previous study. In my study, not only the microscopic interaction but also the interaction between the macroscopic helical structure of the director field and the heat flux is considered to contribute. Thus, it is not unnatural that the upper limit is near the value obtained from the microscopic interaction only.

I next compare the value of the coupling constant with that obtained via the same experimental method by Oswald in 2009 [69]. In this previous study, a diluted Ch compound was used, and the measurements were done with Ch droplets coexisting with their Iso phase by balancing the Lehmann and the electric torque. The value of the coupling constant was

reported to be  $\nu = 1.0 \times 10^{-6} \text{ kg K}^{-1} \text{ s}^{-2}$ . Since the spatial dependence of the magnitude of the electric field applied to the droplets was not taken into account in the study, the consistence of the values are likely to be just coincidence.

Finally, I compare the value with that calculated by the molecular dynamics simulations of Sarman and Laaksonen [88]. Chiral molecules were approximated to be prolate ellipsoids in this simulation. Assuming a repulsive potential including a chiral interaction, they applied a simulated temperature gradient to a cluster of ellipsoids forming uniaxial helical structure. Since the simulation in the actual scale corresponding to experiments requires significant computational resources, the chiral parameter was adjusted for the helical pitch to be about fifty times shorter than that for the actual experiments. In other words, they made the calculation region small. The value of the coupling constant was calculated to be about  $4 \times 10^{-4} \text{ kg s}^{-2}$  from the simulations. Here the units for the coupling constant should be noted, as mentioned in Section 3.2. In this previous study, since the heat flux was taken as  $-\nabla T/T$ , the value needs to be divided by temperature to be compared with the value obtained in my experiment. <sup>2</sup> Dividing the value by room temperature, 300 K,  $\nu \simeq 1 \times 10^{-6} \text{ kg K}^{-1} \text{ s}^{-2}$  is obtained. Although this value is consistent with that in my experiment, the simulated value is expected to be greater because the helical pitch was about fifty times shorter than that in my experiment. I conjecture that the calculated values are smaller than expected because the actual LC phases possess both macroscopic and microscopic chirality, which respectively correspond to the helical structure of the director and the chiral structure of each molecule, whereas the simulations approximated the molecules to be simple ellipsoids without microscopic chirality. In the range of weak chirality, the coupling constant is reportedly proportional to the chirality strength. However, the coupling constant need not be some 50 times greater in the region of

---

<sup>2</sup>In the paper of this previous study [88], the value of the coupling constant was compared with that reported in Reference [70] without correcting for the different definition of the constant.

strong chirality, where the helical pitch is about 50 times shorter, because it is considered to be outside the linear region. Although this discussion is based on somewhat uncertain grounds, I believe that these conjectures provide a qualitative explanation for the difference between the simulated and experimental results.

In comparison with these previous studies, it is not possible to conclude that they are consistent by a simple argument because the conditions such as the materials used, the chirality strength, and the contributions of microscopic and macroscopic chirality all differ for each experiment and simulation. However, it is also true that there are no fatal inconsistencies. At this stage I believe this is a simple picture that the torque induced by a heat flux is determined by the coupling constant  $\nu$ , which depends on the details of the material (chirality strength), and that  $\nu$  is completely independent of the shape, such as bulk and droplet, of the LC and the surrounding environment, such as coexisting phase and emulsion. Indeed, boundary conditions such as shape and the surrounding environment significantly affect the angular velocity, but as long as the same material is subjected to the same temperature conditions, the torque acting on the director per unit volume must be constant (i.e., the coupling constant must be constant). It is also natural to assume that the coupling constant is independent of the surrounding conditions. Unfortunately, the coupling constant has not been measured systematically under varying conditions. Further research should thus compare systematically the coupling constants under different conditions, both experimentally, computationally, and theoretically.



# Chapter 6

## Theoretical Discussion of Rigid-Body Rotation

### 6.1 Purpose

The flow observation by the particle tracking method and the rotation of the droplet–particle composite experimentally revealed that the rigid-body rotation of the Ch droplets can be driven by the Lehmann effect. However, the Lehmann torque exerted on the Ch droplets by a heat flux cannot directly drive the rigid-body rotation because the Lehmann torque acts on the director and is microscopic. In this chapter, I theoretically consider how the microscopic torque acting on the director drives the macroscopic rigid-body rotation of the CC droplets. This discussion also shows under what conditions the rigid-body rotation and the director rotation are driven, respectively. From these conditions, I also determine the condition at which the director rotation and rigid-body rotation switch, which contributes to the experimental control of rotational behavior of the droplets and to the application of the Lehmann effect to micromotors. Moreover, the torque acting on the CC droplet is calculated

specifically under conditions where rigid-body rotation occurs, and torque balance is used to explain the experimental results.

## 6.2 Why rigid-body rotation is driven

The rigid-body rotation of  $N$  droplets dispersed in aqueous solutions is reportedly driven by circularly or linearly polarized laser irradiation [105–107]. The following conditions must be satisfied for irradiation by a polarized laser beam to drive the rigid-body rotation of  $N$  droplets:

1. The rotational viscosity inside the LC droplets exceeds the viscosity of the surrounding liquids.
2. The orientational elasticity combined with the anchoring on the LC–Iso interfaces is larger than the external torque exerted on the LC droplets.

The first condition is not satisfied in my experiment done with samples in the Ch–Iso coexisting phase because the rotational viscosity of the Ch phase and the viscosity of Iso phase are the same order of magnitude. That the second condition is satisfied can be argued by evaluating the coherence length  $\xi$ , defined by Equation 2.21, and the extrapolation length  $b$ , defined by Equation 2.27.

I first calculate the extrapolation length  $b$  to consider how the anchoring affects the Ch–Iso interface. Applied the one-constant approximation, which assumes  $K_{11} = K_{22} = K_{33} \equiv K$ , to Equation 2.16, the extrapolation length is given by

$$b = \frac{K}{A}, \quad (6.1)$$

where  $A$  denotes the anchoring strength. The anchoring on the interface can be neglected

when the radius  $R$  of a droplet is shorter than  $b$ , and the director field inside the droplet is determined only by the orientational elasticity. In contrast, in terms of droplets whose radii are greater than  $b$ , the anchoring on the interface determines the director field inside the droplets [109]. The strength of the conical anchoring at the N–Iso coexisting interface is reported in Reference [22] to be  $A \simeq 2 \times 10^{-6} \text{ J m}^{-2}$ ; the orientational elastic constant of the N phase near the clearing point is reported in Reference [21] to be  $K \simeq 2 \times 10^{-12} \text{ N}$ . These values gives an extrapolation length of  $b \simeq 1 \text{ }\mu\text{m}$ . The radii of the droplets in my experiments were in the range  $R = 4\text{--}11 \text{ }\mu\text{m}$ , satisfying the condition  $R > b$ . Thus, strong anchoring may be assumed on the Ch–Iso interface so that it fixes the director field inside the droplets.

Next I calculate the coherence length  $\xi$  to discuss the competition between the Lehmann torque induced by a heat flux and the orientational elasticity inside the droplets. The torque is exerted on the director inside the droplets under a temperature gradient of  $-\nabla T$  due to the thermomechanical coupling, competing with the torque due to the orientational elasticity:

$$\boldsymbol{\tau} = \nu \mathbf{n} \times [\mathbf{n} \times (-\nabla T)] + K \nabla^2 \mathbf{n}. \quad (6.2)$$

Since the molecular field acting on the director is expressed by Equation 3.17b, the analogy with the electric coherence length shown in Equation 2.21 gives the Lehmann coherence length  $\xi_{\text{Leh}}$  as

$$\xi_{\text{Leh}} = \sqrt{\frac{K}{\nu |\nabla T|}} \quad (6.3)$$

under the one-constant approximation. The Lehmann coherence length  $\xi_{\text{Leh}}$  indicates the thickness of the region in which the director is fixed by the anchoring on the interface, even under the Lehmann torque. Substituting  $\nu \simeq 3 \times 10^{-6} \text{ kg K}^{-1} \text{ s}^{-2}$ , which was obtained experimentally in Chapter 5,  $K \simeq 2 \times 10^{-12} \text{ N}$ , which was reported in Reference [21], and  $|\nabla T| \simeq 1 \times 10^4 \text{ K m}^{-1}$ , which was applied in my experiment, into Equation 6.3,  $\xi_{\text{Leh}}$  is

calculated to be  $\xi_{\text{Leh}} \approx 10 \mu\text{m}$ . Since the maximum droplet radius in my experiment was  $11 \mu\text{m}$ ,  $R \leq \xi_{\text{Leh}}$  is satisfied. The anchoring at the interface, which is sufficiently stronger than the orientational elasticity, and the orientational elasticity, which is larger than the Lehmann torque, together lock the director field inside the droplet. The fixed director field prohibits rotation of only the direction of the molecules, and the rigid-body rotation is driven.

### **6.3 Shape of Ch droplets observed by confocal reflective microscopy**

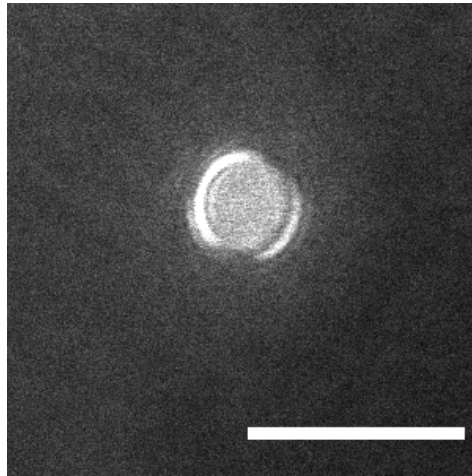
I explained why the rigid-body rotation can be ascribed to the anchoring at the interface and the orientational elasticity inside the droplet. Next I report the measurement of the detailed shape of the droplets in preparation for the calculation of torque balance inside the droplets rotating as rigid bodies.

4-cyano-4'-pentylbiphenyl (produced by LCC, Ltd.) and No. 270032 (produced by LCC, Ltd.) were mixed with a weight ratio of 3 : 2 as a host N compound, and 2.8 wt% (*S*)-2-octyl 4-[4-(hexyloxy) benzoyloxy] benzoate (produced by Tokyo Chemical Industry Co., Ltd.) was added as a chiral dopant. This compound corresponds to Sample B of Section 4.2 without particles. The cell substrates were cleaned ultrasonically and by UV–ozone treatment to remove impurities. They were then spin-coated with PMMA (produced by Sigma-Aldrich). The substrates sandwiched  $20 \mu\text{m}$  spacer beads and the sample. Confocal microscopy was done by using a C2 confocal microscope system with an Eclipse Ni upright microscope (produced by Nikon Corporation) with 488 nm laser light. The horizontal (parallel to the substrate) cross-sectional images of the droplets were taken at intervals of  $0.5 \mu\text{m}$ . The temperature during the observation was controlled by heating the underside of the cell using a conventional heating stage (produced by Linkam Scientific Instruments). Since the short

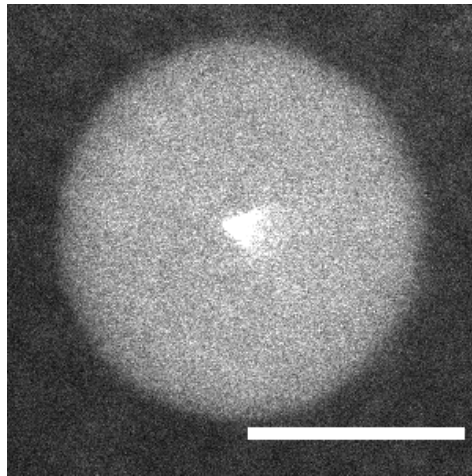
focal distance of the objective lens used in the confocal microscopy did not allow temperature control of the upper side of the cell, the upper side of the cell was in contact with the ambient air at room temperature. Therefore, in the Ch–Iso coexisting phase, Ch droplets formed attached to the upper substrate, which is colder. Figure 6.1 shows cross-sectional images of the Ch droplets under the confocal reflective microscope. Figure 6.1a shows the interface between the upper substrate of the cell and the droplet. The dark field corresponds to the Iso phase, and the round region with a strong reflection corresponds to the interface between the droplet and the substrate. The scale bar in the figure indicates 10  $\mu\text{m}$ ; the radius of the contacting region is 2.8  $\mu\text{m}$ . Figure 6.1b shows the horizontal cross section passing through the center of the droplet. The dark and bright fields correspond to the Iso phase and the droplet interior, respectively. The scale bar also indicates 10  $\mu\text{m}$ ; the radius of the droplet is 2.8  $\mu\text{m}$ . Assuming that the droplet is a true sphere contacting the substrate, the contacting angle  $\theta_E$  is estimated from the radii of the contacting region and the droplet as  $\theta_E \simeq 160^\circ$ , which was almost same for all samples used in my experiments.

## 6.4 Calculation of torque balance for rigid-body rotation

In this section I calculate the torque balance when the droplet rotates as a rigid body, giving an explanation of the experimental results. I start by estimating the Reynolds number  $Re$ . Taking the characteristic velocity as the rotational velocity of the droplet,  $V \simeq 10^{-5} \text{ m s}^{-1}$ , the characteristic length as the droplet radius  $L \simeq 10^{-5} \text{ m}$ , the viscosity as  $\eta \simeq 10^{-2} \text{ Pa s}$ , and the density  $\rho \simeq 10^3 \text{ kg m}^{-3}$ , the Reynolds number is estimated to be  $Re = VL\rho/\eta \simeq 10^{-5}$ . If the Reynolds number is sufficiently less than 1, the inertial term can be neglected, so only the balance of the viscous term need be considered. Let  $\Gamma_{Leh}$  be the  $z$  component of the torque acting on a droplet that contributes to rigid-body rotation due to the Lehmann effect,



(a)



(b)

Figure 6.1: Confocal reflective microscope images of a concentric-circle droplet coexisting with its isotropic phase. The images show horizontal cross sections of (a) the interface between the droplet and the colder substrate and (b) of the plane across the center of the droplet. The bright regions with strong reflection indicate the droplet, and the dark field indicates the Iso phase. The wavelength of the laser was 488 nm. The scale bars indicate 10  $\mu\text{m}$ . This figure is reproduced from Reference [83].

and integrated over the entire droplet. Then the  $z$  component of the viscous drag torque due to rigid-body rotation of the droplet is denoted by  $\Gamma_{\text{vis}}$ . The constant angular velocity of the droplet is determined by

$$\Gamma_{\text{Leh}} = \Gamma_{\text{vis}}. \quad (6.4)$$

First I deal with an individual CC droplet. As shown in Figure 6.2, the origin is taken at the center of the droplet, and the  $z$  axis is taken parallel to the temperature gradient (and perpendicular to the substrates). For the calculation, I assume that the director field in the droplet has a uniaxial helical structure with a wave number  $q$  along the  $z$  axis:

$$\mathbf{n} = (\cos qz, \sin qz, 0). \quad (6.5)$$

One may think that the assumption of a uniaxial director field in the droplet is inappropriate because of the discussion in which the anchoring on the Ch–Iso interface can be approximated to be strong. However, the magnitude of the torque calculated in this section changes only by several percent at most, even under a strong homeotropic anchoring condition. This error is acceptable because the error due to experimental accuracy is of the same order. Thus I assume uniaxial helical structure for the sake of simplicity. As an example of the specific director field inside a Ch droplet, Reference [110] reports a calculated director field. Since anchoring on the interface was assumed to be sufficiently strong in Reference [110], the director field for my experiment is given by removing the surface of a strongly anchored droplet with a thickness of the extrapolation length.

When a heat flux is applied, a Lehmann torque acts on the director. This torque cannot directly drive macroscopic rigid-body rotation because the torque acting on the director is microscopic. Considering the component of the torque on the director which contributes to the rigid-body rotation of the droplet, the torque on director at a certain position inside the

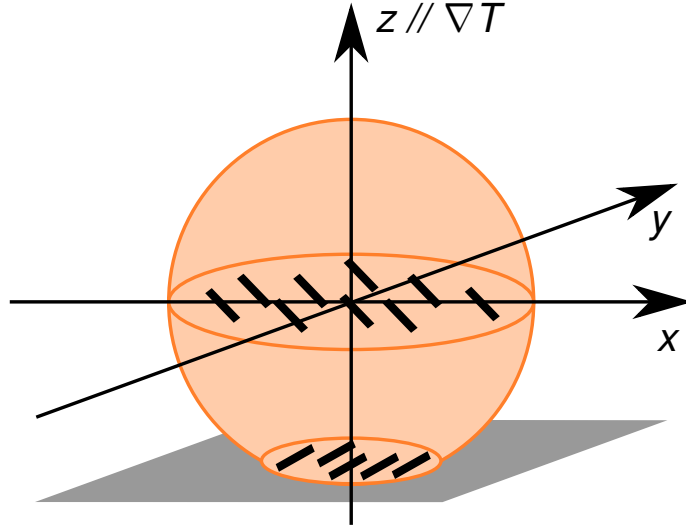


Figure 6.2: Schematic diagram of an individual concentric-circle droplet on the substrate and the coordinate system. The black bars indicate the director. The origin and the  $z$  axis are at the center of the droplet and parallel to the temperature gradient, respectively. This figure is reproduced from Reference [83].

droplet is canceled by that on the director around the position; thus, only the contribution on the interface of the droplet survives. Figure 6.3 shows a cross section of an individual CC droplet at the plane  $z = \text{const.}$ , where black sticks denote the director at an angle  $qz$  from the  $x$  axis. The surface element  $\Delta S$  of the droplet around the  $z$  axis and the vector  $\mathbf{r}'$  from the  $z$  axis to  $\Delta S$  are

$$\Delta S = \mathbf{e}_{r'} \sqrt{R^2 - z^2} \Delta\varphi dz, \quad (6.6)$$

$$\mathbf{r}' = \left( \sqrt{R^2 - z^2} \cos \varphi, \sqrt{R^2 - z^2} \sin \varphi, 0 \right). \quad (6.7)$$

Here  $\mathbf{e}_{r'}$ ,  $R$ , and  $\varphi$  are the standard unit vector in the direction of  $\mathbf{r}'$ , the radius of the droplet, and the azimuthal angle, respectively. The Lehmann torque on  $\Delta S$  that contributes to the



rigid-body rotation of the droplet is given by

$$\Delta\mathbf{\Gamma}_{\text{Leh}} = \mathbf{r}' \times \nu[\mathbf{n} \times (-\nabla T)](\mathbf{n} \cdot \Delta\mathbf{S}). \quad (6.8)$$

Integrating  $\Delta\mathbf{\Gamma}_{\text{Leh}}$  over the whole surface of the droplet yields the magnitude of the Lehmann torque,  $\Gamma_{\text{Leh}}$ , on the whole droplet, which contributes to the rigid-body rotation as

$$\begin{aligned} \Gamma_{\text{Leh}} &= \nu|\nabla T| \int_{R \cos \theta_E}^R dz \int_0^{2\pi} d\varphi (R^2 - z^2) \cos^2(\varphi - qz) \\ &= \nu|\nabla T| \pi f(\theta_E) R^3, \end{aligned} \quad (6.9)$$

where  $f(\theta_E)$  is defined by

$$f(\theta_E) = \frac{2}{3} - \cos \theta_E + \frac{1}{3} \cos^3 \theta_E. \quad (6.10)$$

Although the surface part of the Lehmann torque contributes to the rigid-body rotation, the integrated value is the same as that obtained by integrating the Lehmann torque per unit volume over the whole volume.

Next I calculate the viscous torque that balances the Lehmann torque. I deal with the viscous torque on the droplet interface by considering the result in which a rigid sphere with radius  $R$  rotating at angular velocity  $\omega$  in an infinite fluid with viscosity  $\eta$  is subjected to a viscous torque [111]

$$\Gamma_{\text{vis}} = 8\pi\eta\omega R^3. \quad (6.11)$$

The difference between this calculation and my experiments is that a part of the CC droplets is attached to the glass substrate in my experiments. Thus, the magnitude  $\Gamma_{\text{vis}}$  of the viscous torque accompanied by the rigid-body rotation of the CC droplets should be divided into the

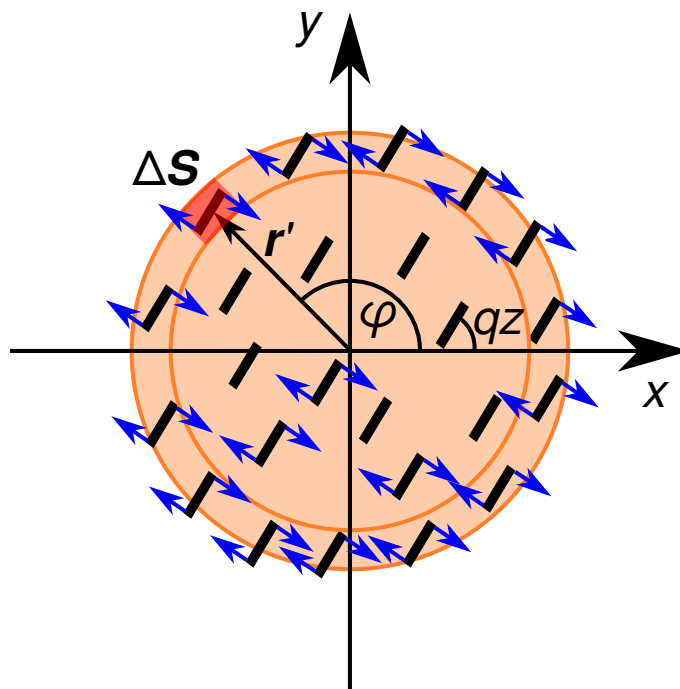


Figure 6.3: Schematic diagram of a cross section of an individual concentric-circle droplet at  $z = \text{const}$ . The bars and the arrows indicate the director and the force exerted on the director by the Lehmann effect, respectively.

viscous torque at the Ch–Iso interface,  $\Gamma_{\text{vis}}^{\text{Iso}}$ , and that at the Ch–substrate interface,  $\Gamma_{\text{vis}}^{\text{sub}}$ :

$$\Gamma_{\text{vis}} = \Gamma_{\text{vis}}^{\text{Iso}} + \Gamma_{\text{vis}}^{\text{sub}}. \quad (6.12)$$

Assuming that the expression of  $\Gamma_{\text{vis}}^{\text{Iso}}$  and its dependence on the physical properties do not differ significantly from Equation 6.11 even for the spherical-cap-shaped droplet,  $\Gamma_{\text{vis}}^{\text{Iso}}$  can be written as

$$\Gamma_{\text{vis}}^{\text{Iso}} = \alpha \pi \eta \omega R^3, \quad (6.13)$$

where  $\alpha$  is a dimensionless parameter indicating the magnitude of the friction on the Ch–Iso interface.

On the other hand, I treat the viscous torque on the Ch–substrate interface,  $\Gamma_{\text{vis}}^{\text{sub}}$ , by assuming the existence of an isotropic disordered layer between the droplet and the substrate. Since the thin layer of PMMA was deposited on the substrates for sake of lubrication, the molecular orientation can be considered to be disordered in this layer. As shown in Figure 6.4, denoting by  $\delta$  the thickness of the layer and by  $\gamma_\delta$  the hydrodynamic viscosity, I assume that the usual viscous force, which is proportional to the velocity gradient, acts on the layer. Based on the assumption  $\Delta \Gamma_{\text{vis}}^{\text{sub}}$ , the torque around the  $z$  axis exerted on a surface element of the Ch–substrate interface at the position  $\mathbf{r}'$  is given by

$$\Delta \Gamma_{\text{vis}}^{\text{sub}} = \mathbf{r}' \times \gamma_\delta \frac{r' \omega}{\delta} \mathbf{e}_\varphi r' dr' d\varphi. \quad (6.14)$$

The magnitude of the viscous torque exerted on the Ch–substrate interface is obtained by integrating  $\Delta \Gamma_{\text{vis}}^{\text{sub}}$ :

$$\Gamma_{\text{vis}}^{\text{sub}} = \int_0^{2\pi} d\varphi \int_0^{R \sin \theta_E} dr' r' \gamma_\delta \frac{r' \omega}{\delta} r' = \frac{\gamma_\delta \pi}{\delta} \omega R^4 \sin^4 \theta_E, \quad (6.15)$$

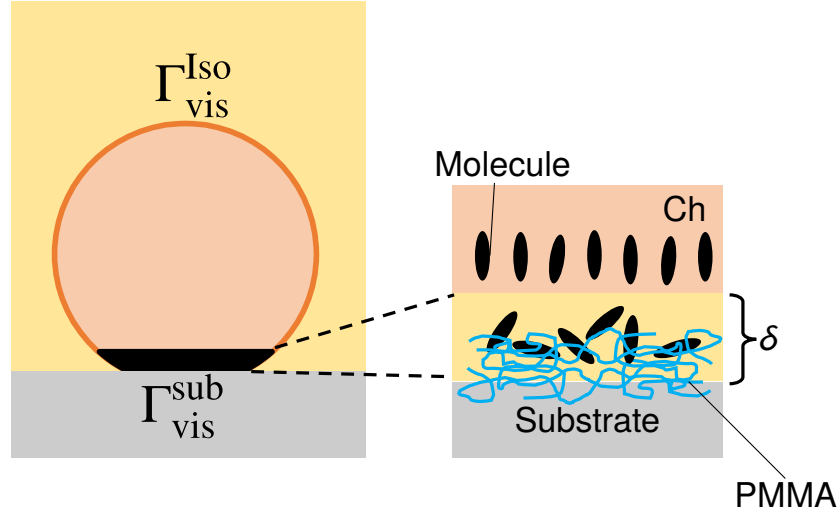


Figure 6.4: Schematic figures of a vertical cross section of an individual concentric-circle droplet (left) and of magnified cholesteric–substrate interface (right).

where  $\gamma_\delta/\delta$  is considered as the parameter indicating the viscous property on the Ch–substrate interface.

The torque balance from Equations 6.9, 6.13, and 6.15 gives the angular velocity of the droplet as

$$\omega = \frac{\nu |\nabla T_z| f(\theta_E)}{\alpha \eta + \frac{\sin^4 \theta_E \gamma_\delta}{2} \frac{R}{\delta}}, \quad (6.16)$$

where  $\nu$ ,  $\theta_E$ , and  $\eta$  are physical properties that depend on the materials,  $\nabla T$  and  $R$  are parameters controlled experimentally, and  $\alpha$  and  $\gamma_\delta/\delta$  are unknown parameters that indicate the viscous properties on the Ch–Iso and Ch–substrate interfaces, respectively.  $\nu \simeq 3 \times 10^{-6} \text{ kg K}^{-1} \text{ s}^{-2}$  and  $\theta_E \simeq 160^\circ$ , which were measured in my experiments, and  $\eta \simeq 5 \times 10^{-2} \text{ Pa s}$ , which was reported in Reference [112], can be substituted into Equation 6.16. Substituting the magnitude of the temperature gradient  $|\nabla T_z| \simeq 10^4 \text{ K m}^{-1}$  applied in the experiment in Section 4.7, Equation 6.16 should correspond to the droplet-radius dependence of the angular velocity measured in Section 4.7 (Figure 4.15). The dashed line in Figure 4.15 is the best-fit line from Equation 6.16 with fitting parameters  $\alpha$  and  $\gamma_\delta/\delta$ . Here,  $\alpha \simeq 0.06$  and  $\gamma_\delta/\delta \simeq 1.1 \times 10^6$

$\text{kg m}^{-2} \text{s}^{-2}$  gave the best fit. The parameter  $\alpha$  is significantly less than 8, which suggests that the viscous friction at the Ch–Iso interface is much, much smaller, implying that the usual nonslip boundary condition is not satisfied at the coexisting interface. The friction at the coexisting interface is discussed in Chapter 7. Therefore, the viscous torque on the Ch–substrate interface is dominant in my experimental system.

Next let us calculate the torque balance in terms of the dumbbell-like aggregate composed of droplets and particles. The Lehmann torque exerted on the composite is derived as follows: As shown in Figure 6.5, the origin is taken at the point where two droplets touch each other; the  $x$  axis passes through the centers of the two droplets, and the  $z$  axis is parallel to the temperature gradient (perpendicular to the substrates). The director field inside the droplets is assumed to be the uniaxial helical structure in the  $z$  direction, as expressed by Equation 6.5. Although the Lehmann torque is induced on the director of the whole composite, only the surface torque survives to contribute to the rigid-body rotation of the composite in the same way as the individual CC droplet. As shown in Figure 6.6, a cross section at  $z = \text{const.}$ , the torque around the rotational axis ( $z$  axis) acting on a surface element  $\Delta S$ , whose position with respect to the  $z$  axis is denoted by  $\mathbf{r}'$ , is given by the same equation as the individual droplet, Equation 6.8. Considering one of the constituent droplets of the composite,  $\mathbf{r}'$  can be divided into  $\mathbf{r}_G$ , a vector from the  $z$  axis to the central axis of the droplet, and  $\mathbf{r}''$ , a vector from the central axis of the droplet to  $\Delta S$ ;

$$\mathbf{r}' = \mathbf{r}_G + \mathbf{r}'' = (R + \sqrt{R^2 - z^2} \cos \varphi, \sqrt{R^2 - z^2} \sin \varphi, 0), \quad (6.17)$$

$$\mathbf{r}_G = (R, 0, 0), \quad (6.18)$$

$$\mathbf{r}'' = (\sqrt{R^2 - z^2} \cos \varphi, \sqrt{R^2 - z^2} \sin \varphi, 0). \quad (6.19)$$

Therefore, the magnitude of the Lehmann torque on one of the constituent droplets of the

composite which contributes to the rigid-body rotation is

$$\begin{aligned}
\Gamma_{\text{Leh}} &= \nu |\nabla T| \int_{R \cos \theta_E}^R dz \int_0^{2\pi} d\varphi R \sqrt{R^2 - z^2} \cos qz (\cos qz \cos \varphi + \sin qz \sin \varphi) \\
&\quad + \nu |\nabla T| \int_{R \cos \theta_E}^R dz \int_0^{2\pi} d\varphi (R^2 - z^2) \cos qz (\cos qz \cos \varphi + \sin qz \sin \varphi)^2 \\
&= \nu |\nabla T| \pi f(\theta_E) R^3.
\end{aligned} \tag{6.20}$$

The result equals the value obtained by integrating the Lehmann torque on the director per unit volume over the whole droplet in the same way as the single droplet. Since the aggregate is composed of two droplets, the total Lehmann torque is given by  $\Gamma_{\text{Leh}} = 2\nu |\nabla T| \pi f(\theta_E) R^3$ .

In terms of the viscous torque on the rotating composite, only  $\Gamma_{\text{vis}}^{\text{sub}}$  is taken into account from the beginning because the argument regarding the interfacial friction of the single droplet reveals the dominance of the viscous torque at the Ch–substrate interface. Assuming the existence of the disordered layer formed by the PMMA film between the droplet and the substrate in the same way as the single droplet, the viscous torque around the rotational axis ( $z$  axis) acting on a surface element on the Ch–substrate interface at the position  $\mathbf{r}'$  can be calculated by dividing  $\mathbf{r}'$  into  $\mathbf{r}_G$  and  $\mathbf{r}''$ . Here,  $\mathbf{r}_G$  and  $\mathbf{r}''$  are vectors from the  $z$  axis to the center of the contacting region and from the center of the contacting region to the surface element, respectively [78]:

$$\begin{aligned}
\Gamma_{\text{vis}}^{\text{sub}} &= 2 \int_0^r dr'' \int_0^{2\pi} d\varphi \frac{\gamma_\delta}{\delta} \omega \{ (R + r'' \cos \varphi)^2 + r''^2 \sin^2 \varphi \} \\
&= \frac{\gamma_\delta}{\delta} \pi \omega r^4 \left( 1 + 2 \frac{R}{r} \right).
\end{aligned} \tag{6.21}$$

Substituting the values corresponding to the experiment in Section 4.6,  $\theta_E \simeq 160^\circ$ ,  $|\nabla T| \simeq 2 \times 10^4 \text{ K m}^{-1}$ ,  $R \simeq 10 \times 10^{-6} \text{ m}$ ,  $\nu \simeq 3 \times 10^{-6} \text{ kg K}^{-1} \text{ s}^{-2}$ , and  $\omega \simeq 3 \times 10^{-2} \text{ rad s}^{-1}$ , into

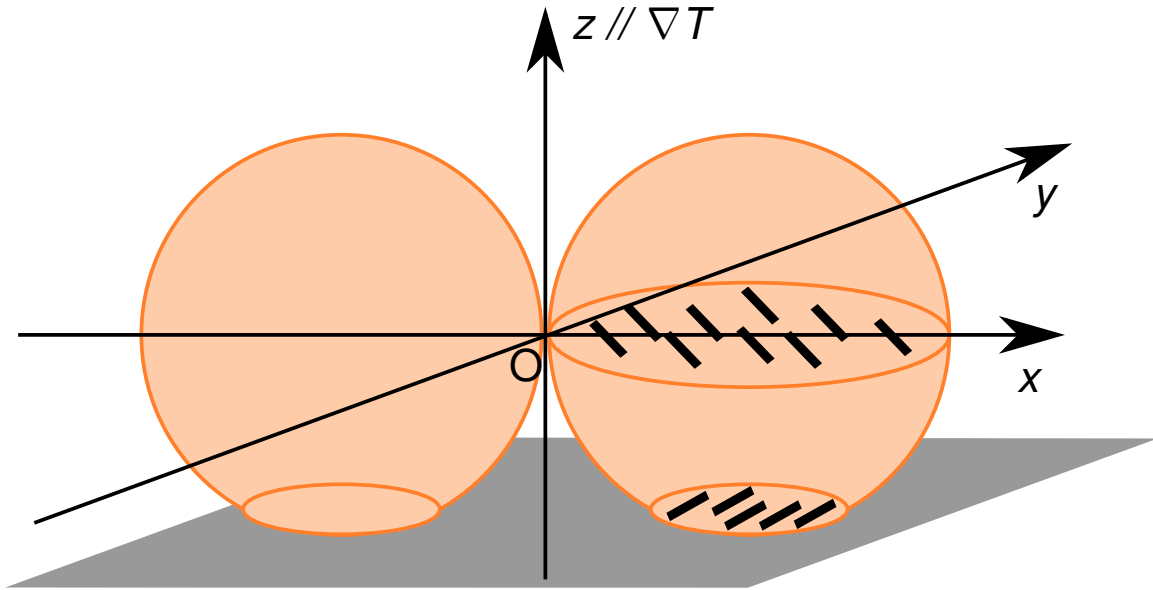


Figure 6.5: Schematic diagram of an aggregate of two concentric-circle droplets on the substrate and the coordinate system. The black bars indicate the director. The origin and the  $z$  axis were taken at the center of the composite and parallel to the temperature gradient, respectively.

the balance between Equations 6.20 and 6.21,  $\gamma_\delta/\delta \approx 2.3 \times 10^6 \text{ kg m}^{-2} \text{ s}^{-2}$  is obtained as the parameter indicating the viscous friction at the Ch–substrate interface. This value of  $\gamma_\delta/\delta$  is consistent with that for the individual droplet. Thus, this argument concerning the torque balance consistently explains the rigid-body rotation driven by the Lehmann effect. It should be noted that the parameters  $\alpha$  and  $\gamma_\delta/\delta$  can be determined accurately by fitting the experimental result in which the angular velocity is measured with various radii under a constant temperature gradient. However, the possibility of forming the composites is very low (a composite is formed about every hundred trials), and it was hard to obtain sufficient data with various sizes. For this reason, I set  $\alpha$  to zero from the beginning and substituted the experimental values into the torque balance to estimate  $\gamma_\delta/\delta$  directly.

Finally, I would like to discuss  $\gamma_\delta/\delta$ . In terms of the actual interface, it is reasonable to think that there no clear boundary exists between the Ch droplet and the disordered layer

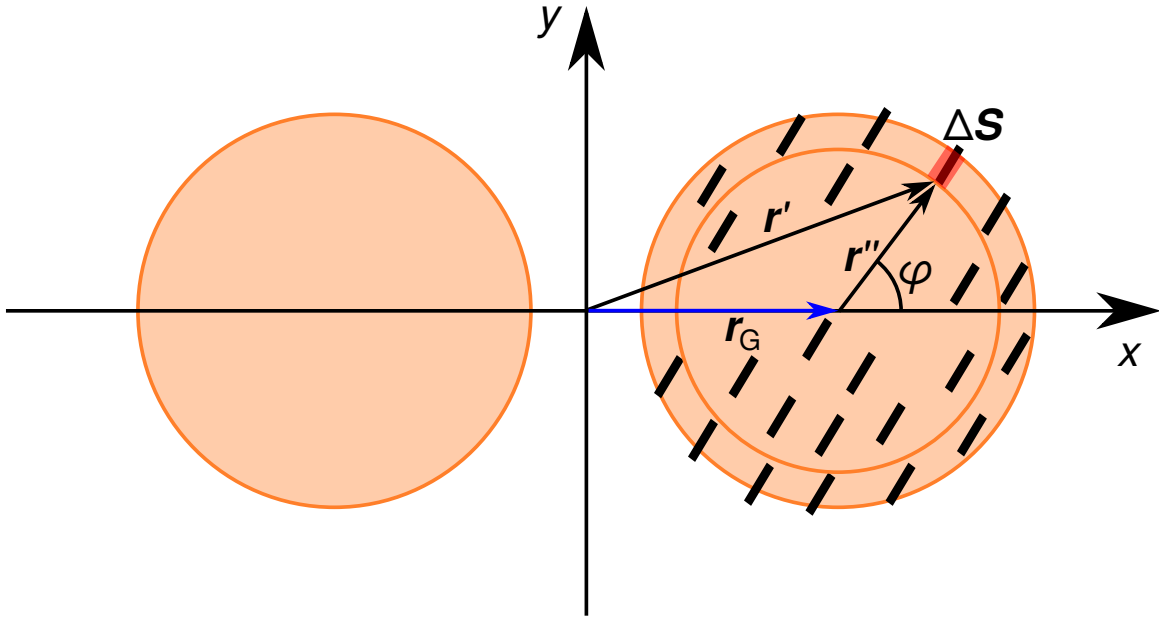


Figure 6.6: Schematic diagram of a cross section of an aggregate of two concentric-circle droplets at  $z = \text{const}$ . The bars indicate the director.

shown in Figure 6.4, and that there a transitional region exists where the orientational order gradually changes. However, I assume the hypothetical boundary for the sake of quantitative discussion and denote by  $\delta$  the thickness of the layer. Since the layer should be thicker than the spin-coated PMMA on the substrate, the minimum value for  $\delta$  is given by  $\delta > 1 \times 10^{-8}$  m. On the other hand, since the disordered layer is not observed with the confocal reflective microscope (Figure 6.1a), the layer should be thinner than the vertical resolution of the microscope, which is about  $0.5 \mu\text{m}$ . Thus, the thickness of the disordered layer should be in the range  $1 \times 10^{-8} \text{ m} < \delta < 5 \times 10^{-7} \text{ m}$ . This condition gives the range of the viscosity of the disordered layer as  $2 \times 10^{-2} \text{ Pa s} < \gamma_\delta < 1 \text{ Pa s}$ , which corresponds to the typical value for LC compounds. This argument of torque balance is also consistent with the known properties. It may seem inconsistent that the friction on the Ch–Iso interface is small enough to be negligible whereas the usual friction occurs between the Ch phase and the disordered



layer. I speculate that the inconsistency can be ascribed to the difference between the Iso phase and the disordered layer; the layer is an isotropic layer formed by disordered molecular orientation due to the PMMA and is not a pure coexisting phase. Further study is necessary regarding the friction of the interfaces.

# Chapter 7

## Friction at Liquid Crystal–Isotropic Coexisting Interface

### 7.1 Purpose

In previous experiments the hydrodynamic flow accompanied by the Lehmann rotation of the Ch droplets coexisting with their Iso phase was measured by tracking the particles adhering onto the Ch–Iso interface. In contrast, in this section I report measurement and calculation of the flow field in the Iso phase around the rotating Ch droplet visualized by the particles dispersed in surrounding Iso phase. The vortexlike flow in the Iso phase should be accompanied by the rotation of the droplet when the usual nonslip boundary condition is satisfied at the Ch–Iso interface. However, the extraordinarily small value of  $\alpha$  from Chapter 6 implies that the nonslip boundary condition is not satisfied at the coexisting interface. If the Ch–Iso interface is slippery, vortexlike flow should not occur in the Iso phase. The purpose of this chapter is to investigate the dynamic properties of the Ch–Iso coexisting interface by observing the flow in the Iso phase.

## 7.2 Flow measurement in isotropic phase near rotating cholesteric droplets

### 7.2.1 Methods

The same sample as Sample A in Chapter 4 was used for this experiment. A host nematic LC was prepared by mixing 4-cyano-4'-pentylbiphenyl (produced by LCC, Ltd.) and No. 270032 (produced by LCC, Ltd., Table 4.1) with a weight ratio of 2 : 3, and 1.0 wt% (*S*)-4-[1-(methylheptyl)oxy]carbonyl-phenyl-4-(hexyloxy)benzoate (produced by DIC Corporation) was added as a chiral dopant. Particles with an averaged diameter of 1  $\mu\text{m}$  were added to the compound as tracers to visualize the flow. The compound was sandwiched in a 10- $\mu\text{m}$ -thick gap between glass substrates with spin-coated PMMA. The temperature was controlled by a conventional heating stage (produced by Linkam Scientific Instruments), which is also the same as was done with Sample A in Chapter 4. Only the bottom of the cell was heated, and the top of the cell was cooled by exposure to the ambient air. A heat flux progressed from the bottom to the top of the cell. Observations were made by using a BX51 polarizing microscope (produced by Olympus Corporation) with a linear polarizer positioned between the light source and the specimen.

### 7.2.2 Results

Figure 7.1 shows an polarizing microscopy image sequence of a Ch droplet coexisting with its Iso phase and an aggregate of the particles dispersed in the Iso phase. The snapshots were taken every 20 s. The droplet is characterized by its striped texture, so the helical axis is perpendicular and parallel to the heat flux and the substrates, respectively, as shown by the white arrow in Figure 7.1. Upon applying the heat flux, the droplet rotates by the Lehmann

effect in the clockwise direction. The blue dot outside the droplet is the particle aggregate dispersed in the Iso phase, which exhibits vigorous thermal fluctuations at its position. From the beginning to the end of the image sequence in Figure 7.1, the particle aggregate in the vicinity of the rotating droplet did not move significantly, whereas the texture of the droplet rotated through about  $180^\circ$ . Open circle and cross plots in Figure 7.2 indicate the rotational angles of the texture of the droplet shown in Figure 7.1 and of the particle aggregate in the vicinity of the droplet, respectively. The graph shows that the particle aggregate near the droplet undergoes no significant unidirectional motion whereas the texture rotates at a constant velocity. Open-circle plots in Figure 4.5 of Chapter 4 show the relationship between the angular velocity  $\omega_{\text{droplet}}$  of the texture of the droplet and the angular velocity of the particle aggregate in vicinity of the droplet  $\omega_{\text{particle}}$ . In terms of the droplets with various velocities and the particle aggregates near the droplets, I obtained the consistent result in which the particles do not exhibit any significant motion. Since the particles moved due to the thermal fluctuated, it was not that the particles adhered onto the substrate to be stuck. Thus, if there was a flow accompanied by the rotation of the droplet, the particles should have exhibited unidirectional motion along the flow. This result indicates that there was not any detectable flow in surrounding Iso phase in spite of the rigid-body rotation of the droplet. When a usual rigid sphere rotates in a usual viscous fluid, a vortexlike flow is expected to be occur in the fluid; this result is counterintuitive and unexpected. The absence of the flow around the rotating droplet suggests that the usual non-slip boundary condition is not satisfied on the Ch-Iso coexisting interface. The dynamic abnormality of the interface implied by the small value of  $\alpha$  was also observed experimentally.

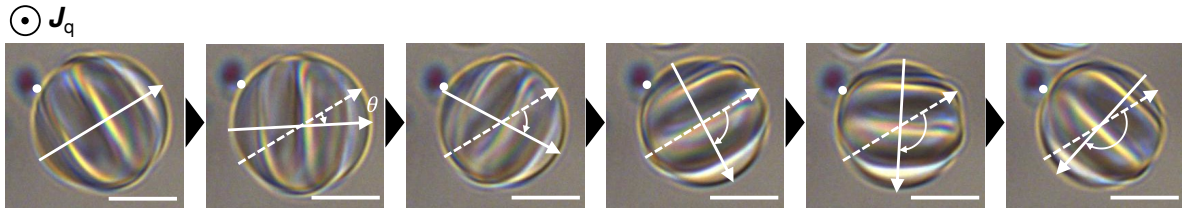


Figure 7.1: An image sequence of a striped droplet coexisting with its isotropic phase and particle aggregates dispersed in the vicinity of the droplet under a polarizing microscope with a linearly polarized incident light. The transmitted light was detected without polarizers. The snapshots were taken every 20 s, and the scale bars indicate 10  $\mu\text{m}$ . The white solid arrow, the white dashed arrow, the white dot, and  $\mathbf{J}_q$  denote the helical axis, the initial state of the helical axis, the position of a particle aggregate, and the heat flux, respectively. A temperature gradient of  $4.2 \pm 0.2 \text{ mK } \mu\text{m}^{-1}$  was applied to the liquid crystal sample by a heating stage (see Figure 4.1a). This figure is reproduced from Reference [81].

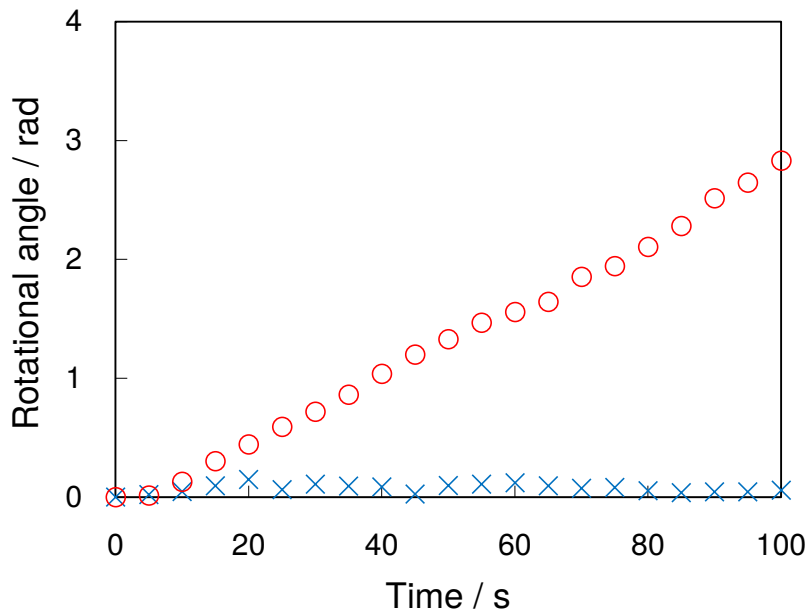


Figure 7.2: Temporal changes in the rotational angles of the helical axis of the droplet (open circles) and a particle aggregate dispersed in vicinity of the droplet (crosses) shown in Figure 7.1, respectively. This figure is reproduced from Reference [81].

### 7.3 Numerical calculation of flow field around droplets

I conducted a numerical calculation to quantitatively estimate the flow field which should occur when a usual rigid sphere rotates in a usual viscous fluid. When a rigid sphere with a radius  $R$  sandwiched by two parallel substrates is rotating at an angular velocity  $\Omega$ , the flow field in the fluid around the rotating sphere obeys the Navier–Stokes equation at the steady state;

$$(\mathbf{v} \cdot \nabla) \mathbf{v} = -\frac{\nabla p}{\rho} + \eta \nabla^2 \mathbf{v}. \quad (7.1)$$

Here incompressibility and uniform viscosity is assumed;  $\mathbf{v}$ ,  $p$ ,  $\rho$ , and  $\eta$  denote velocity, pressure, density, and viscosity, respectively. Taking a cylindrical coordinate system  $(r, \varphi, z)$  with the  $z$  axis passing through the center of the droplet and perpendicular to the substrates, both  $\mathbf{v} = (v_r, v_\varphi, v_z)$  and  $p$  do not depend on  $\varphi$  from the rotational symmetry around the  $z$  axis. Moreover, assuming the  $r$  and the  $z$  components of  $\mathbf{v}$  do not occur by the rotation of the sphere,  $\text{div } \mathbf{v} = 0$  yields  $\mathbf{v} = (0, v_\varphi(r, z), 0)$ . Thus the equation for  $v_\varphi$  is obtained from Equation 7.1 as

$$\frac{\partial^2 v_\varphi}{\partial r^2} + \frac{1}{r} \frac{\partial v_\varphi}{\partial r} + \frac{\partial^2 v_\varphi}{\partial z^2} - \frac{v_\varphi}{r^2} = 0. \quad (7.2)$$

Differentiating Equation 7.2 in the  $rz$  plane divided into partitions with a width of  $R/160$  in both the  $r$  and the  $z$  directions, the difference equation for  $v_\varphi$  is derived as

$$v_{i,j} = \left\{ \left( 1 + \frac{1}{r_i} \right) v_{i+1,j} + \left( 1 - \frac{1}{r_i} \right) v_{i-1,j} + v_{i,j+1} + v_{i,j-1} \right\} \left( 4 + \frac{1}{r_i^2} \right)^{-1}, \quad (7.3)$$

where the index  $\varphi$  is omitted for simplicity. In order to solve this equation I assumed that

1. the non-slip boundary condition is satisfied on the sphere and substrate.
2.  $\mathbf{v} = \mathbf{0}$  at  $r = 2R$  since there is another Ch droplet about  $2R$  away from a droplet in my

experiment.

I reiterated the calculation of Equation 7.3 with the initial state of  $v_{i,j} = 0$  for all  $i$  and  $j$  under these boundary conditions. When the remainder of  $v_{i,j}/R\Omega$ , the normalized velocity, at each point became less than  $10^{-11}$ , I judged the calculation result to be converged and ceased the calculation. The normalized angular velocity  $\omega/\Omega$  at each point obtained from the calculated  $v_{i,j}$  is shown in the color map Figure 7.3. The lower graph in Figure 7.3 shows the angular velocity at  $z = R$ , the height of the center of the droplet. A vortexlike flow with an angular velocity  $\omega = \Omega$  occurs in the fluid on the surface of the sphere; the flow attenuates as the position is away from the sphere, which is in line with intuition.

In the flow measurement using the particles explained in the previous section, the radial position of the particle aggregate near the rotating droplet (Figure 7.1) is expressed by  $r/R \simeq 1.2$ . Although Figure 7.3 shows that there should be a flow at  $r/R \simeq 1.2$ , the particle aggregate at this position did not exhibit significant motion. This implies that the flow is too weak to detect in contrast to the expectation.<sup>1</sup> The inconsistency between the calculation and the experimental result may be ascribed to the assumptions for the calculation. That is to say, there is a possibility that the non-slip boundary condition is not satisfied on the Ch–Iso coexisting interface. At this point, the detailed properties and the specific explanation of this extraordinary interface are not obtained; Further research is necessary.

---

<sup>1</sup>It is not certain if the particle aggregate was at  $z = R$  in my experiment because to determine the  $z$  position of the particle aggregate was difficult. However, I assumed the particle aggregate was at  $z = R$  as it fluctuated randomly in the  $z$  direction.

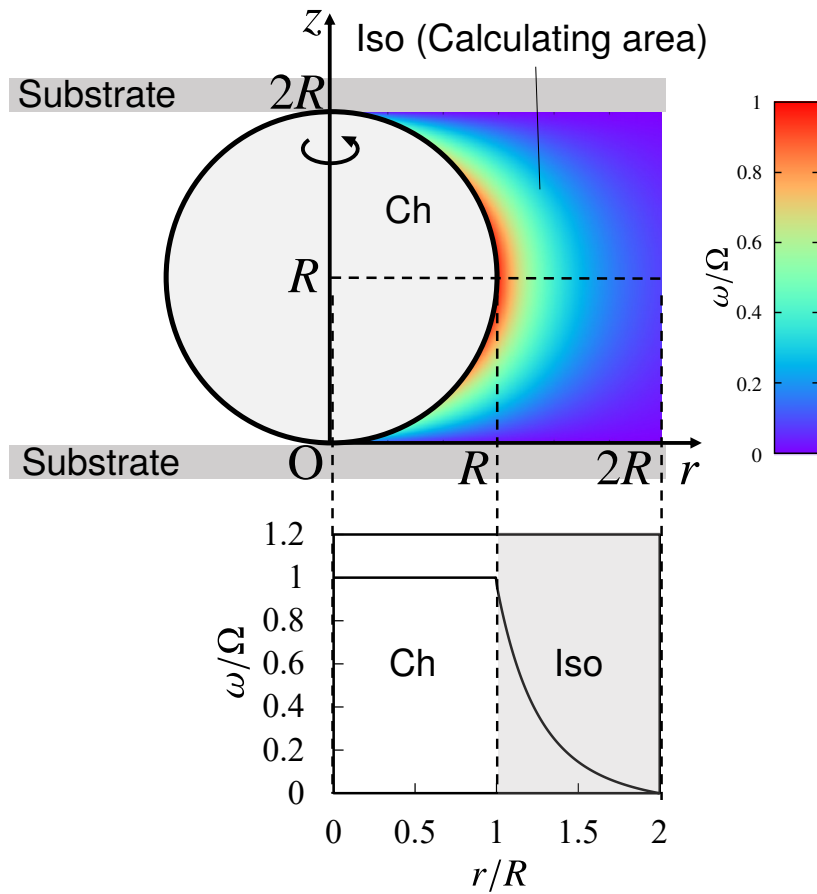


Figure 7.3: The upper schematic shows the vertical cross section of the geometry used to calculate the flow field around the rotating rigid sphere. The color map is the result of the calculation. The lower graph gives the magnitude of the flow at  $z = R$  obtained by the calculation.



# Chapter 8

## Conclusions

This dissertation reported my study to reveal the detailed molecular motion—the director rotation or the rigid-body rotation—driven by the thermomechanical coupling (the Lehmann effect) which takes place in chiral liquid crystals (cholesterics). I would like to summarize Chapters 4–7 in which my own study was explicated.

In Chapter 4, I explicated the flow measurement by using the particle tracking method. The tracer particle with an average diameter of  $\sim 1 \mu\text{m}$  were added to the liquid crystal samples; the flow accompanied by the Lehmann rotation of the droplets was visualized by tracing the particles. The particle tracking method for the liquid crystal cells had not been realized because the added particles were likely to adhere onto the glass substrates due to the high interfacial energy of more than  $\sim 10 \text{ mN m}^{-1}$  between the LCs and the glass substrates. I tried various types of particles by changing physical and chemical parameters such as the size, material, and surface modification of the particles. I finally realized the particles which adhere onto the liquid crystal–isotropic interface or disperse in the isotropic phase.

As a result of tracking the motion of the particles which adhered onto the cholesteric droplets rotating under a heat flux, I found that the particles rotated at the same velocity as

the texture of the droplet. Translational motion of the particles accompanied by the textural rotation indicates the existence of a hydrodynamic flow, which is the proof of the rigid-body rotation of the droplets. Moreover, the angular velocity of the texture and that of the particles were consistent with each other, indicating the pure rigid-body rotation without any orientational rotation. In my experiment, the interaction between the director and the particle can be neglected because of following reasons. (i) the director field was not distorted by the adhesion of the particles. (ii) the position of the particles on the droplet was independent of the director field of the droplet. The results which indicate the rigid-body rotation of the cholesteric droplets were consistent for both the striped droplets and concentric-circle droplets. Therefore, it was proved that the rigid-body rotation of the cholesteric droplets can be driven by the Lehmann effect regardless of the directions of the helical axis of the director and of the heat flux.

Furthermore, I formed a dumbbell-like shaped aggregate with two concentric-circle droplets and particles, observing the Lehmann rotation of the whole composite successfully. The composite exhibited unidirectional rotation with keeping its shape and orientational structure under a heat flux. Constituent droplets of the composite revolved about the rotational axis of the composite, which cannot be explained only by the director rotation and was obviously the rigid-body rotation. I revealed that the Lehmann effect can drive the rigid-body rotation of cholesteric droplets not only by the hydrodynamic flow measurement but also by the novel geometry in which the composite rotates.

In Chapter 5, I reported the result of the measurement of the coupling constant  $\nu$  between the heat flux and the torque induced by the Lehmann effect. The coupling constant was derived from the static equilibrium condition in which the total torque induced by an AC electric field and the Lehmann effect on cholesteric droplets coexisting with their own isotropic phase becomes zero. This method itself is not new. However, I calculated the spatial dependence of

the electric field to obtain accurate value of the coupling constant. The coupling constant was estimated as  $\nu \simeq 3 \times 10^{-6} \text{ kg K}^{-1} \text{ s}^{-2}$  from my experiment, which is not inconsistent with the values obtained with other materials and calculations.

In Chapter 6, I discussed the reason why not the director rotation but the rigid-body rotation was driven by the Lehmann effect in my experiment. The reason for the rigid-body rotation in my experiment can be ascribed to the anchoring on the liquid crystal–isotropic interface and the orientational elasticity inside the droplets. I estimated the extrapolation length, which indicates the strength of anchoring on the interface, as  $1 \text{ }\mu\text{m}$ . Since the radius of the cholesteric droplets was  $\simeq 10 \text{ }\mu\text{m}$  in my experiment, the extrapolation length is considered to be so small that the anchoring on the interface can be approximated to be strong. Thus, the director inside the droplet is fixed by the anchoring on the interface. On the other hand, the Lehmann coherence length was estimated to be  $10 \text{ }\mu\text{m}$ . The coherence length indicates the thickness of the layer in the vicinity of the strong anchoring interface, where the director field is not distorted due to the Lehmann torque. Since the anchoring on the cholesteric–isotropic interface can be approximated to be strong in my experiment, the director field is not distorted for  $10 \text{ }\mu\text{m}$  from the interface. Considering that the radius of the droplets were  $\simeq 10 \text{ }\mu\text{m}$ , the anchoring on the droplet interface, which is approximated to be strong, and the orientational elasticity inside the droplet, which is greater than the external torque, completely lock the director field. Thus, the director rotation, in which only the direction of the molecules are rotated, cannot be driven, but the rigid-body rotation is driven. I would like to note that I do not deny the director rotation as this argument is based on the comparison between the extrapolation length, the Lehmann coherence length, and the radius of the droplet. For example, when the radius of the droplet is larger than the coherence length, the distortion of the director field inside the droplet is allowed; the director rotation should be driven.

Moreover, I calculated the torque balance specifically. Since the Reynolds number of the Lehmann rotation of the droplets is small enough to neglect the inertia terms, I considered the balance between the Lehmann torque and the viscous torque. The component of the Lehmann torque which contributes to the rigid-body rotation of the droplets can be obtained as the surface integration over the droplet surface, which corresponds to the volume integration of the Lehmann torque per unit volume. The viscous torque should be divided into that on the cholesteric–isotropic interface and that on the cholesteric–substrate interface. The viscous properties on the cholesteric–isotropic and the cholesteric–substrate interfaces are denoted by the parameters of  $\alpha$  and  $\gamma_\delta/\delta$ , respectively. Fitting the experimental result with these parameters, I obtained  $\alpha = 0.06$  and  $\gamma_\delta/\delta \simeq 10^6 \text{ kg m}^{-2} \text{ s}^{-2}$  for both the individual droplets and the composites.

In Chapter 7, I investigated hydrodynamic flow in the isotropic phase in the vicinity of the rotating cholesteric droplets under a heat flux by using particle tracking method. When a usual rigid sphere is rotating in a usual viscous fluid, hydrodynamic flow should occur in surrounding fluid. However, it was found that there was not any detectable flow around the droplets rotating as rigid bodies. This result implies that usual non-slip boundary condition is not satisfied on the cholesteric–isotropic interface, which is consistent with the small value of  $\alpha$ . Dynamic property of coexisting interface is not fully understood at this point, and further investigation is necessary.

# Acknowledgments

I gratefully acknowledge Professor Yuka Tabe, my supervisor, for her intensive guidance. I am also grateful to Professor Mitsunori Takano, my co-supervisor and referee, and Professor Yoshihiro Yamazaki, my referee, for their valuable comments and discussions. I would like to thank Doctor Shinji Bono for his guidance in my early work. I would also like to thank Professor Hiroshi Yokoyama for fruitful discussions, Professor Ken Ishikawa for his generous support regarding controlling temperature and fabricating LC cells, and Professor Isa Nishiyama for his support and advice about materials.

My work and my college life were partially supported by Support for Pioneering Research Initiated by the Next Generation, Japan Science and Technology Agency and Research Fellowships for Young Scientists, Japan Society for the Promotion of Science. I appreciate the support.

# References

- [1] F. Reinitzer. Beiträge zur Kenntniss des Cholesterins. *Monatshefte für Chemie und verwandte Teile anderer Wissenschaften*, 9:421–441, 1888.
- [2] O. Lehmann. über fließende Krystalle. *Zeitschrift für Physikalische Chemie*, 4:462–472, 1889.
- [3] M. Schadt and W. Helfrich. Voltage-Dependent Optical Activity of a Twisted Nematic Liquid Crystal. *Applied Physics Letters*, 18:127–128, 1971.
- [4] H. Kawamoto. The history of liquid-crystal displays. *Proceedings of the IEEE*, 90:460–500, 2002.
- [5] O. Lehmann. Structur, System und magnetisches Verhalten flüssiger Krystalle und deren Mischbarkeit mit festen. *Annalen der Physik*, 307:649–705, 1900.
- [6] O. Lehmann. *Flüssige Kristalle Und Ihr Scheinbares Leben*. Leopold Voss, Leipzig, 1921.
- [7] M. Meister, G. Lowe, and H. C. Berg. The proton flux through the bacterial flagellar motor. *Cell*, 49:643–650, 1987.
- [8] S. A. Lloyd, F. G. Whitby, D. F. Blair, and C. P. Hill. Structure of the C-terminal domain of FliG, a component of the rotor in the bacterial flagellar motor. *Nature*, 400:4, 1999.

- [9] H. C. Berg. The Rotary Motor of Bacterial Flagella. *Annual Review of Biochemistry*, 72:19–54, 2003.
- [10] B. Chaban, H. V. Hughes, and M. Beeby. The flagellum in bacterial pathogens: For motility and a whole lot more. *Seminars in Cell & Developmental Biology*, 46:91–103, 2015.
- [11] P. D. Boyer. The binding change mechanism for ATP synthase—Some probabilities and possibilities. *Biochimica et Biophysica Acta - Bioenergetics*, 1140:215–250, 1993.
- [12] J. P. Abrahams, A. G. W. Leslie, R. Lutter, and J. E. Walker. Structure at 2.8 Å resolution of F1-ATPase from bovine heart mitochondria. *Nature*, 370:621–628, 1994.
- [13] P. D. Boyer. The ATP Synthase—A Splendid Molecular Machine. *Annual Review of Biochemistry*, 66:717–749, 1997.
- [14] H. Noji, R. Yasuda, M. Yoshida, and K. Kinosita. Direct observation of the rotation of F1-ATPase. *Nature*, 386:299–302, 1997.
- [15] A. Hinton, S. Bond, and M. Forgac. V-ATPase functions in normal and disease processes. *Pflügers Archiv - European Journal of Physiology*, 457:589–598, 2009.
- [16] L. D. Landau and E. M. Lifshitz. *Electrodynamics of Continuous Media*. Pergamon Press, Oxford, 1960.
- [17] R. W. Whatmore. Pyroelectric devices and materials. *Reports on Progress in Physics*, 49:1335–1386, 1986.
- [18] M. Fiebig. Revival of the magnetoelectric effect. *Journal of Physics D: Applied Physics*, 38:R123–R152, 2005.

- [19] S. B. Lang and S. Muensit. Review of some lesser-known applications of piezoelectric and pyroelectric polymers. *Applied Physics A*, 85:125–134, 2006.
- [20] G. J. Snyder and E. S. Toberer. Complex thermoelectric materials. *Nature Materials*, 7:105–114, 2008.
- [21] A. Bogi and S. Faetti. Elastic, dielectric and optical constants of 4'-pentyl-4-cyanobiphenyl. *Liquid Crystals*, 28:729–739, 2001.
- [22] H. Yokoyama, S. Kobayashi, and H. Kamei. Measurement of Director Orientation at the Nematic–Isotropic Interface Using a Substrate-Nucleated Nematic Film. *Molecular Crystals and Liquid Crystals*, 107:311–331, 1984.
- [23] H. Yokoyama, S. Kobayashi, and H. Kamei. Deformations of a Planar Nematic–Isotropic Interface in Uniform and Nonuniform Electric Fields. *Molecular Crystals and Liquid Crystals*, 129:109–126, 1985.
- [24] J. H. Gibbs and E. A. DiMarzio. Nature of the Glass Transition and the Glassy State. *The Journal of Chemical Physics*, 28:373–383, 1958.
- [25] L. D. Landau and E. M. Lifshitz. *Quantum Mechanics*. Pergamon Press, Oxford, 2nd edition, 1965.
- [26] L. D. Landau and E. M. Lifshitz. *Statistical Physics*. Pergamon Press, Oxford, 2nd edition, 1969.
- [27] J. Timmermans. Plastic Crystals: A Historical Review. *Journal of Physics and Chemistry of Solids*, 18:1–8, 1961.
- [28] S. Chandrasekhar. *Liquid Crystals*. Cambridge University Press, Cambridge, New York, 2nd edition, 1992.



- [29] P. G. de Gennes and J. Prost. *The Physics of Liquid Crystals*. Clarendon Press, Oxford, 2nd edition, 1993.
- [30] J. N Israelachvili. *Intermolecular and Surface Forces*. Academic Press, Massachusetts, 3rd edition, 2011.
- [31] J. Meunier, D. Langevin, N. Boccara, and H. K. V. Lotsch, editors. *Physics of Amphiphilic Layers*, volume 21 of *Springer Proceedings in Physics*. Springer, Berlin, Heidelberg, 1987.
- [32] G. J. Vroege and H. N. W. Lekkerkerker. Phase transitions in lyotropic colloidal and polymer liquid crystals. *Reports on Progress in Physics*, 55:1241–1309, 1992.
- [33] M. Szwarc, M. Levy, and R. Milkovich. Polymerization initiated by electron transfer to monomer. A new method of formation of block polymers. *Journal of the American Chemical Society*, 78:2656–2657, 1956.
- [34] A. Skoulios. La structure des solutions aqueuses concentrées de savon. *Advances in Colloid and Interface Science*, 1:79–110, 1967.
- [35] F. C. Bawden, N. W. Pirie, J. D. Bernal, and I. Fankuchen. Liquid Crystalline Substances from Virus-infected Plants. *Nature*, 138:1051–1052, 1936.
- [36] H. Zocher. Über freiwillige Strukturbildung in Solen. (Eine neue Art anisotrop flüssiger Medien.). *Zeitschrift für anorganische und allgemeine Chemie*, 147:91–110, 1925.
- [37] L. Onsager. The Effects of Shape on the Interaction of Colloidal Particles. *Annals of the New York Academy of Sciences*, 51:627–659, 1949.

- [38] R. S. Werbowyj and D. G. Gray. Liquid Crystalline Structure In Aqueous Hydroxypropyl Cellulose Solutions. *Molecular Crystals and Liquid Crystals*, 34:97–103, 1976.
- [39] R. S. Werbowyj and D. G. Gray. Ordered Phase Formation in Concentrated Hydroxypropylcellulose Solutions. *Macromolecules*, 13:69–73, 1980.
- [40] G. Friedel. Les états mésomorphes de la matière. *Annales de Physique*, 9:273–474, 1922.
- [41] T. Sluckin, D. Dunmur, and H. Stegemeyer. *Crystals That Flow : Classic Papers From the History of Liquid Crystals Liquid Crystals Book Series*. Taylor & Francis Routledge, 2004.
- [42] J. F. Johnson and R. S. Porter. *Liquid Crystals and Ordered Fluids*, volume 2. Springer, Boston, 1974.
- [43] D. Demus and H. Zschke. *Flüssige Kristalle in Tabellen II*, volume 2. Deutscher Verlag für Grundstoffindustrie, Leipzig, 1984.
- [44] H. Kikuchi. *Liquid Crystalline Blue Phases*, volume 128 of *Liquid Crystalline Functional Assemblies and Their Supramolecular Structures. Structure and Bonding*. Springer, Berlin, Heidelberg, 2007.
- [45] D. Demus and L. Richter. *Textures of Liquid Crystals*. Verlag Chemie, Weinheim, New York, 1978.
- [46] I. Dierking. *Textures of Liquid Crystals*. Wiley-VCH, Weinheim, 1st edition, 2003.
- [47] O. D. Lavrentovich and D.-K. Yang. Cholesteric cellular patterns with electric-field-controlled line tension. *Physical Review E*, 57:R6269–R6272, 1998.

- [48] G. H. Brown. *Advances in Liquid Crystals*, volume 1. Academic Press, New York, San Francisco, London, 1975.
- [49] G. Vertogen and W. H. de Jeu. *Thermotropic Liquid Crystals, Fundamentals*, volume 45 of *Springer Series in Chemical Physics*. Springer, Berlin, Heidelberg, 1988.
- [50] S. Chandrasekhar and N. V. Madhusudana. Spectroscopy of Liquid Crystals. *Applied Spectroscopy Reviews*, 6:189–311, 1972.
- [51] J. R. McColl and C. S. Shih. Temperature Dependence of Orientational Order in a Nematic Liquid Crystal at Constant Molar Volume. *Physical Review Letters*, 29:85–87, 1972.
- [52] W. Maier and A. Saupe. Eine einfache molekulare Theorie des nematischen kristallinflüssigen Zustandes. *Zeitschrift für Naturforschung A*, 13:564–566, 1958.
- [53] Y. Poggi, J. C. Filippini, and R. Aleonard. The free energy as a function of the order parameter in nematic liquid crystals. *Physics Letters A*, 57:53–56, 1976.
- [54] C. W. Oseen. The theory of liquid crystals. *Transactions of the Faraday Society*, 29:883, 1933.
- [55] F. C. Frank. I. Liquid crystals. On the theory of liquid crystals. *Discussions of the Faraday Society*, 25:19, 1958.
- [56] J. F. Nye. *Physical Properties of Crystals: Their Representation by Tensors and Matrices*. Clarendon Press, Oxford, New York, 1st edition, 1984.
- [57] P. G. de Gennes. Short Range Order Effects in the Isotropic Phase of Nematics and Cholesterics. *Molecular Crystals and Liquid Crystals*, 12:193–214, 1971.

- [58] V. Fréedericksz and A. Repiewa. Theoretisches und Experimentelles zur Frage nach der Natur der anisotropen Flüssigkeiten. *Zeitschrift für Physikalische Chemie*, 42:532–546, 1927.
- [59] V. Fréedericksz and V. Zolina. Forces causing the orientation of an anisotropic liquid. *Transactions of the Faraday Society*, 29:919–930, 1933.
- [60] H. Zocher. The effect of a magnetic field on the nematic state. *Transactions of the Faraday Society*, 29:945, 1933.
- [61] P. Oswald, A. Dequidt, and G. Poy. Lehmann effect in nematic and cholesteric liquid crystals: A review. *Liquid Crystals Reviews*, 7:142–166, 2019.
- [62] N. Éber and I. Jánossy. An experiment on the thermomechanical coupling in cholesterics. *Molecular Crystals and Liquid Crystals*, 72:233–238, 1982.
- [63] N. V. Madhusudana and R. Pratibha. An experimental investigation of electromechanical coupling in cholesteric liquid crystals. *Liquid Crystals*, 5:1827–1840, 1989.
- [64] Y. Tabe and H. Yokoyama. Coherent collective precession of molecular rotors with chiral propellers. *Nature Materials*, 2:806–809, 2003.
- [65] S. Hénon and J. Meunier. Microscope at the Brewster angle: Direct observation of first-order phase transitions in monolayers. *Review of Scientific Instruments*, 62:936–939, 1991.
- [66] D. Hoenig and D. Moebius. Direct visualization of monolayers at the air-water interface by Brewster angle microscopy. *The Journal of Physical Chemistry*, 95:4590–4592, 1991.

- [67] Y. Tabe and H. Yokoyama. Fresnel formula for optically anisotropic Langmuir monolayers: An application to Brewster angle microscopy. *Langmuir*, 11:699–704, 1995.
- [68] P. Oswald and A. Dequidt. Measurement of the Continuous Lehmann Rotation of Cholesteric Droplets Subjected to a Temperature Gradient. *Physical Review Letters*, 100:217802, 2008.
- [69] P. Oswald. Lehmann rotation of cholesteric droplets subjected to a temperature gradient: Role of the concentration of chiral molecules. *The European Physical Journal E*, 28:377–383, 2009.
- [70] P. Oswald. Microscopic vs. macroscopic origin of the Lehmann effect in cholesteric liquid crystals. *The European Physical Journal E*, 35:10, 2012.
- [71] P. Oswald and S. Pirkl. Lehmann rotation of the cholesteric helix in droplets oriented by an electric field. *Physical Review E*, 89:022509, 2014.
- [72] J. Yoshioka, F. Ito, Y. Suzuki, H. Takahashi, H. Takizawa, and Y. Tabe. Director/barycentric rotation in cholesteric droplets under temperature gradient. *Soft Matter*, 10:5869, 2014.
- [73] P. Oswald and G. Poy. Lehmann rotation of cholesteric droplets: Role of the sample thickness and of the concentration of chiral molecules. *Physical Review E*, 91:032502, 2015.
- [74] T. Yamamoto, M. Kuroda, and M. Sano. Three-dimensional analysis of thermomechanically rotating cholesteric liquid crystal droplets under a temperature gradient. *Europhysics Letters*, 109:46001, 2015.

- [75] G. Poy and P. Oswald. Do Lehmann cholesteric droplets subjected to a temperature gradient rotate as rigid bodies? *Soft Matter*, 12:2604–2611, 2016.
- [76] S. Bono, S. Sato, and Y. Tabe. Unidirectional rotation of cholesteric droplets driven by UV-light irradiation. *Soft Matter*, 13:6569–6575, 2017.
- [77] P. Oswald and G. Poy. Role of impurities in the Lehmann effect of cholesteric liquid crystals: Towards an alternative model. *Physical Review E*, 98:032704, 2018.
- [78] S. Bono, Y. Maruyama, and Y. Tabe. Formation and dynamics of the aggregates of cholesteric double-twist cylinders. *Soft Matter*, 14:9798–9805, 2018.
- [79] S. Bono, Y. Maruyama, K. Nishiyama, and Y. Tabe. Photo-Controllable Rotation of Cholesteric Double-Twist Cylinders. *Molecular Crystals and Liquid Crystals*, 683:39–45, 2019.
- [80] S. Bono, Y. Maruyama, K. Nishiyama, and Y. Tabe. A thermomechanical coupling in cholesteric liquid crystals: Unidirectional rotation of double-twist cylinders driven by heat flux. *The European Physical Journal E*, 42:99, 2019.
- [81] K. Nishiyama, S. Bono, Y. Maruyama, and Y. Tabe. Direct Observation of Rigid-Body Rotation of Cholesteric Droplets Subjected to a Temperature Gradient. *Journal of the Physical Society of Japan*, 88:063601, 2019.
- [82] S. Bono, Y. Maruyama, K. Nishiyama, and Y. Tabe. Heat-Driven Rigid-Body Rotation of a Mixture of Cholesteric Liquid Crystal Droplets and Colloids. *The Journal of Physical Chemistry B*, 124:6170–6174, 2020.

- [83] K. Nishiyama, S. Bono, and Y. Tabe. Steady rigid-body rotation of cholesteric droplets and their dumbbell-shaped aggregates driven by heat flux along the helical axes. *Soft Matter*, 17:10818–10828, 2021.
- [84] F. M. Leslie. Some Thermal Effects in Cholesteric Liquid Crystals. *Proceedings of the Royal Society A: Mathematical, Physical and Engineering Sciences*, 307:359–372, 1968.
- [85] S. Sarman. Molecular dynamics simulation of thermomechanical coupling in cholesteric liquid crystals. *Molecular Physics*, 98:27–35, 2000.
- [86] S. Sarman. Transport properties of cholesteric liquid crystals studied by molecular dynamics simulation. *Molecular Physics*, 99:1235–1247, 2001.
- [87] S. Sarman and A. Laaksonen. Molecular Dynamics Simulation of Viscous Flow and Heat Conduction in Liquid Crystals. *Journal of Computational and Theoretical Nanoscience*, 8:1081–1100, 2011.
- [88] S. Sarman and A. Laaksonen. Thermomechanical coupling, heat conduction and director rotation in cholesteric liquid crystals studied by molecular dynamics simulation. *Physical Chemistry Chemical Physics*, 15:3442–3453, 2013.
- [89] S. Sarman, Y.-L. Wang, and A. Laaksonen. Thermomechanical coupling in coarse grained cholesteric liquid crystal model systems with pitches of realistic length. *Physical Chemistry Chemical Physics*, 18:16822–16829, 2016.
- [90] J. L. Ericksen. Inequalities in Liquid Crystal Theory. *Physics of Fluids*, 9:1205, 1966.
- [91] J. L. Ericksen. General Solutions in the Hydrostatic Theory of Liquid Crystals. *Transactions of the Society of Rheology*, 11:5–14, 1967.

- [92] L. D. Landau and E. M. Lifshitz. *Theory of Elasticity*. Butterworth-Heinemann, Oxford, 3rd edition, 1986.
- [93] J. L. Ericksen. Anisotropic Fluids. *Archive for Rational Mechanics and Analysis*, 4:231–237, 1959.
- [94] J. L. Ericksen. Theory of Anisotropic Fluids. *Transactions of the Society of Rheology*, 4:29–39, 1960.
- [95] J. L. Ericksen. Transversely isotropic fluids. *Kolloid-Zeitschrift*, 173:117–122, 1960.
- [96] F. M. Leslie. Some Constitutive Equations for Anisotropic Fluids. *The Quarterly Journal of Mechanics and Applied Mathematics*, 19, 1966.
- [97] M. J. Stephen. Hydrodynamics of Liquid Crystals. *Physical Review A*, 2:1558–1562, 1970.
- [98] D. Forster, T. C. Lubensky, P. C. Martin, J. Swift, and P. S. Pershan. Hydrodynamics of Liquid Crystals. *Physical Review Letters*, 26:1016–1019, 1971.
- [99] F. Jähnig and H. Schmidt. Hydrodynamics of liquid crystals. *Annals of Physics*, 71:129–166, 1972.
- [100] P. C. Martin, O. Parodi, and P. S. Pershan. Unified Hydrodynamic Theory for Crystals, Liquid Crystals, and Normal Fluids. *Physical Review A*, 6:2401–2420, 1972.
- [101] L. Onsager. Reciprocal Relations in Irreversible Processes. I. *Physical Review*, 37:405–426, 1931.
- [102] L. Onsager. Reciprocal Relations in Irreversible Processes. II. *Physical Review*, 38:2265–2279, 1931.



- [103] D. Svenšek, H. Pleiner, and H. R. Brand. Inverse Lehmann effects can be used as a microscopic pump. *Physical Review E*, 78:021703, 2008.
- [104] S. Sato, S. Bono, and Y. Tabe. Unidirectional Heat Transport Driven by Rotating Cholesteric Droplets. *Journal of the Physical Society of Japan*, 86:023601, 2017.
- [105] S. Juodkazis, S. Matsuo, N. Murazawa, I. Hasegawa, and H. Misawa. High-efficiency optical transfer of torque to a nematic liquid crystal droplet. *Applied Physics Letters*, 82:4657–4659, 2003.
- [106] C. Manzo, D. Paparo, L. Marrucci, and I. Jánossy. Light-induced rotation of dye-doped liquid crystal droplets. *Physical Review E*, 73:051707, 2006.
- [107] Y. Yang, P. D. Brimicombe, N. W. Roberts, M. R. Dickinson, M. Osipov, and H. F. Gleeson. Continuously rotating chiral liquid crystal droplets in a linearly polarized laser trap. *Optics Express*, 16:6877, 2008.
- [108] I.-H. Lin, D. S. Miller, P. J. Bertics, C. J. Murphy, J. J. de Pablo, and N. L. Abbott. Endotoxin-induced structural transformations in liquid crystalline droplets. *Science*, 332:1297–1300, 2011.
- [109] M. Urbanski, C. G. Reyes, J. Noh, A. Sharma, Y. Geng, V. S. R. Jampani, and J. P. F. Lagerwall. Liquid crystals in micron-scale droplets, shells and fibers. *Journal of Physics: Condensed Matter*, 29:133003, 2017.
- [110] D. Seč, T. Porenta, M. Ravnik, and S. Žumer. Geometrical frustration of chiral ordering in cholesteric droplets. *Soft Matter*, 8:11982, 2012.
- [111] L. D. Landau and E. M. Lifshitz. *Fluid Mechanics*. Pergamon Press, Oxford, 3rd edition, 1966.

[112] A. G. Chmielewski. Viscosity Coefficients of Some Nematic Liquid Crystals. *Molecular Crystals and Liquid Crystals*, 132:339–352, 1986.

# List of Research Achievements

## Academic Papers

- Katsu Nishiyama, Shinji Bono, and Yuka Tabe. Steady rigid-body rotation of cholesteric droplets and their dumbbell-shaped aggregates driven by heat flux along the helical axes. *Soft Matter*, Vol. 17, No. 48, pp. 10818–10828, 2021. Selected as the back cover.
- Shinji Bono, Yuji Maruyama, Katsu Nishiyama, and Yuka Tabe. Heat-Driven Rigid-Body Rotation of a Mixture of Cholesteric Liquid Crystal Droplets and Colloids. *The Journal of Physical Chemistry B*, Vol. 124, No. 28, pp. 6170–6174, 2020.
- Shinji Bono, Yuji Maruyama, Katsu Nishiyama, and Yuka Tabe. A thermomechanical coupling in cholesteric liquid crystals: Unidirectional rotation of double-twist cylinders driven by heat flux. *The European Physical Journal E*, Vol. 42, p. 99, 2019.
- Katsu Nishiyama, Shinji Bono, Yuji Maruyama, and Yuka Tabe. Direct Observation of Rigid-Body Rotation of Cholesteric Droplets Subjected to a Temperature Gradient. *Journal of the Physical Society of Japan*, Vol. 88, No. 6, p. 063601, 2019. Selected as the Papers of Editors' Choice.
- Shinji Bono, Yuji Maruyama, Katsu Nishiyama, and Yuka Tabe. Photo-Controllable

Rotation of Cholesteric Double-Twist Cylinders. *Molecular Crystals and Liquid Crystals*, Vol. 683, No. 1, pp. 39–45, 2019.

## Review

- Katsu Nishiyama and Yuka Tabe. Direct Observation of Unidirectional Rotation of Cholesteric Droplets Subjected to a Temperature Gradient. *AAPPS Bulletin*, Vol. 29, No. 5, pp. 40–41, 2019.

## Lectures

- 西山活, 多辺由佳. 熱-力学交差相関によって駆動されるカイラル液晶滴の剛体回転. 第10回ソフトマター研究会, 福岡, 2022年11月.
- Katsu Nishiyama, and Yuka Tabe. Steady Rigid-Body Rotation of Cholesteric Droplets Driven by the Lehmann Effect. 28th International Liquid Crystal Conference. Lisbon, July 2022.
- 西山活, 多辺由佳. 分子トルクが駆動する液晶滴のマクロな剛体回転. Young Soft Webinar (第10回セミナー), オンライン, 2022年5月.
- 西山活, 多辺由佳. Lehmann効果によって駆動されるコレステリック液晶滴の剛体回転. 第8回 ZAIKEN Festa (講演番号 C-23), オンライン, 2022年3月.
- 西山活, 多辺由佳 他. らせん軸と平行な熱流下におけるコレステリック液晶滴の剛体回転. 2021年日本液晶学会討論会 (講演番号 1CO4), オンライン, 2021年9月.

- 西山活, 坊野慎治, 丸山雄司, 多辺由佳. 温度勾配下におけるコレステリック液晶滴の剛体回転の直接観察. 2019年日本液晶学会討論会 (講演番号 2B06), つくば, 2019年9月.
- 西山活. 光照射による局所的な発熱が駆動するコレステリック液晶滴の定常回転. 第九回京都若手ソフトマター研究会 (講演番号 2), 京都, 2019年3月. ポスター賞受賞.
- 西山活, 丸山雄司, 坊野慎治, 多辺由佳. 一方向光照射による同一掌性コレステリック液晶滴の双方向同時回転. 2018年日本液晶学会討論会 (講演番号 PA47), 岐阜, 2018年9月.